UNIVERSITÀ DEGLI STUDI DI PADOVA
DIPARTIMENTO DI INGEGNERIA CIVILE, EDILE E AMBIENTALE
Department of Civil, Environmental and Architectural Engineering

Corso di Laurea Magistrale in Mathematical Engineering

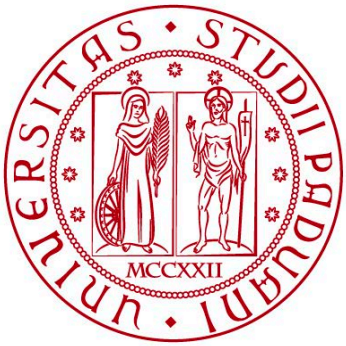

TESI DI LAUREA MAGISTRALE

Development of a reacting flow solver to model the combustion of hydrocarbons fuels in detonation engines

Relatori:
Chiar.mo Prof. Stefano Lanzoni
Chiar.mo Dr. Bayindir H. Saracoglu

Laureando:
Ludovico Nista
Matricola:
1133362

ANNO ACCADEMICO 2017-2018

Abstract

The pressure rise attained through a detonation process inspires alternative power generation and propulsion system based on detonation combustors. In order to model such detonation based systems, an open-source unsteady reacting flow solver with detailed chemistry modelling for detonation engines was developed in the scope of this master dissertation work. OpenFoam version 2.1 is used as the development platform for the new detonation solver. Unsteady Reynolds Averaged Navier-Stokes equations were solved to model the turbulence flow. Three dimensional species mass continuity equations were implemented to handle the complex mixtures behind the detonation wave. The new solver resolves the combustion phenomena through finite rate chemistry with Arrhenius form of reaction rate. Consequently, it can solve the chemical kinetics behind the detonation wave using both reduced and detailed reaction schemes. Such an approach allows modelling of detonation of various fuels with affordable computational time depending on the chosen reaction kinetics. Two distinct solvers were developed to properly simulate deflagration-to-detonation transition (DDT) phenomena: a pressure-based solver rests on PISO algorithm for the deflagration and a density based solver rests on second order HLCC Riemann solver to resolve the strong gradients across the detonation wave. The solver was initially tested through the DDT of H_2-Air mixture in a notched tube. Results were obtained both for single step chemistry and detailed reaction mechanism including 19 elementary reactions and 9 species and then compared with experimental results on the same setup. Subsequently, the solver was also tested through the DDT of C_2H_2-Oxygen mixture in another notched tube. Results were obtained only for detailed reaction mechanism including 25 elementary reactions and 10 species and compared with experimental data. Moreover, the flame velocities obtained inside the DDT tubes were compared with theoretical Chapman-Jouget velocities obtained from Cantera package and analytical solutions. Tests to resolve the detonation cell structures were performed and cell sizes comparable with results in the literature were obtained for both mixtures. Lastly, the developed solver was used to simulate complex flow in rotating detonation engines.

Acknowledgements

I would first like to thank my thesis supervisor *Dr. Bayindir H. Saracoglu* of the Aeronautics and Aerospace Department at the Von Karman Institute of Fluid Dynamics. He completely supported me on this work becoming a real mentor. In his office, we shared each other several ideas, not only technical, passing me down other important teachings. He pushed me to do my best in all situations, getting me back up on my feet when needed. It is an honour to have met a person of such depth.

I would also like to acknowledge *Prof. Stefano Lanzoni* of the engineering school at the University of Padova and *Dr. Ali Can Ispir* of the Aeronautics and Aerospace Department at the Von Karman Institute of Fluid Dynamics, as the second readers of this thesis. I am gratefully indebted to them for their very valuable comments on this thesis.

In addition, I would like to thank my friends or whoever helped me during this demanding path. Many thanks for having completely supported me without asking anything back. Because also to you, I have achieved this goal.

Finally, I must express my very profound gratitude to my parents, *Alessio* and *Luciana*, to my sister, *Veronica*, and to my whole family, especially *Nonna Lea*, for having provided me with unfailing support and continuous encouragement throughout my years of study and through the process of researching and writing this thesis. This accomplishment would not have been possible without their love. Thank you.

I wish this dissertation will be an example for my niece, *Emilia*, encouraging her to work hard with always a lot of dedication.

Ludovico Nista

Rhode-Saint-Genese (Belgium), October 9, 2018

"Mettere in discussione se stessi é il modo migliore per capire gli altri"
— Michelangelo Buonarroti

Contents

List of Tables

List of Figures

Chapter 1

Introduction

The concept of the detonation engine dates back to the pioneering work of Hoffman [1]. He proposed some experiments as early as 1940 using both gaseous acetylene and benzene as a liquid hydrocarbon fuel mixed with oxygen with intermittent detonation results, but most research for propulsion applications has taken place only in the last 50 years due to the complex nature of rapidly mixing the fuel and air at high speeds, and initiating and sustaining a detonation using a controlled and cyclic method in fuel-air mixtures [2].

At the same time, detonation engines offer the potential for high thrust and efficiency in a large operational envelope with the advantage of being mechanically very simple to operate, that leads to low weight and costs. The addition of thrust tubes in a multitube arrangement also offers the potential for increased thrust as well as increasing the frequency with which a single tube can be fired.

However, to date, no practical detonation engines have been put into production; it may be due to significant key difficulties: achieving deflagration-detonation transition, that has the largest impact on detonation cycle, without requiring a tube long enough to make it impractical and drag-imposing on the aircraft, reducing the noise and damping the severe vibration caused by the operation of the engine, can be just a few examples. But the high thermodynamic efficiency offered by these new combustors may be reduced once for all the specific fuel consumption. For the moment, only one of these engines was successfully integrated into a low-speed demonstra-

tion aircraft that flew in sustained pulse detonation engine powered flight in 2008 [3]. It is then the intent of the research to identify the main variables that govern detonation transition and outline a reliable open-source solver able to simulate both overall and detailed flow nature within detonation engines.

1.1 Thermodynamic closure of detonation engines

Detonation engines have attracted considerable attention over the last decades because of their high theoretical thermal efficiency and specific impulse. These types of engines offer pressure augmentation through the combustion process[1], which is considered a constant volume: it implies a large theoretical cycle efficiency increase (around 10%) compared to the Joule cycle [4] and consequently a reduction in exhaust emissions. The Brayton-Joule cycle, nowadays, is the thermodynamically standard for gas turbine engines, like turbofan or turbojet engines in civil aviation [5]. Moreover, the high-pressure ratios associated with detonation combustion may eliminate the need for expensive high-pressure feed system, thereby reducing propulsion system weight, complexity, costs and packaging volume. In addition, air-breathing detonation engines can potentially operate over a wide range of flight Mach numbers (from 0 to 5), without the assistance of booster stages.

1.1.1 Turbojet and Turbofan Engines

Most modern airliners and military aircrafts are powered by gas turbine engines, called Turbofan or Turbojet. The latter are composed by five parts, as shown in Figure 1.1: air inlet, compressors, combustion chamber, turbines (that drives the compressor) and outlet nozzle. The working principle is a bit nested with respect to the detonation engines: large amounts of surrounding air are continuously brought into the engine inlet. Behind the inlet, the air enters into the compressor. The compressor produces a jump in pressure. At the exit of the compres-

[1] A detonation combustor is commonly referred to pressure gain combustor because of the significant total pressure rise during the combustion process.

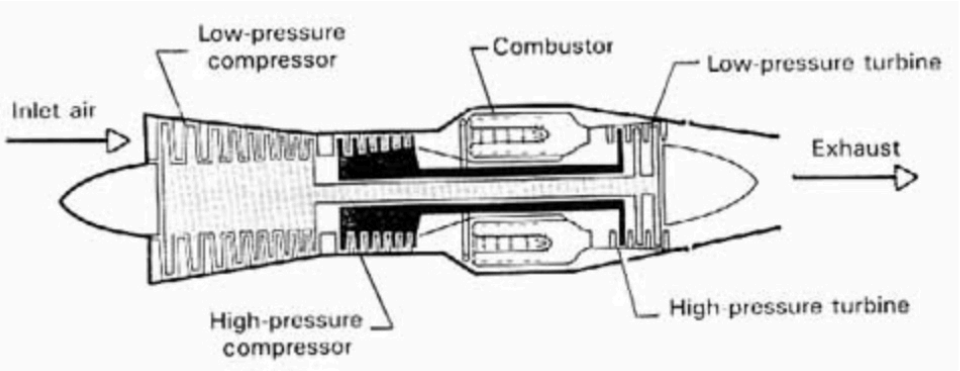

Figure 1.1: Sketch of turbojet engine proposed by [6]

sor, the air is at much higher pressure than free stream. In the burner a small amount of fuel is combined with the air and ignited. Leaving the burner, the hot exhaust is passed through the turbine. In a jet engine, the energy extracted by the turbine is used to turn the compressor by linking the compressor and the turbine by a central shaft. Basically, the turbine takes some energy out of the hot exhaust, but there is enough energy left over to provide thrust to the jet engine by increasing the velocity through the nozzle. Since the exit velocity is greater than the free stream velocity, a first estimation of the thrust, derived by Nasutti [5], is analytically given by:

$$Thrust = F = \dot{m}_e V_e - \dot{m}_a V_0 + (p_e - p_0) A_e \tag{1.1}$$

where F indicates the downstream force, $\dot{m}$ the mass flow rate (mass/time) of both free stream (0) and at the exit (e)[2], V the velocity, p the static pressure, A the area of the nozzle. Actually, this cannot be considered the real thrust because it takes into account only the pressure acting on the engine. Hence, the effective thrust is reduced by a factor D depending on the shape of engine. Furthermore, introducing the ratio between the mass fuel rate and the mass air rate f, the Equation 1.1 is given by:

$$F = \dot{m}_a[(1+f)V_e - V_0] + (p_e - p_0)A_e \rightarrow F = (\dot{m}_a + \dot{m}_f)V_e - \dot{m}_a V_0 + (p_e - p_0)A_e \tag{1.2}$$

[2]Summing together fuel and air masses.

Considering the pressure and temperature limits on the compressors and turbines stages, typical values of f are equal to 2% ($f \ll 1$). Finally, the thrust is defined by:

$$F \approx \dot{m}_a(V_e - V_0) + (p_e - p_a)A_e \tag{1.3}$$

Other useful parameter, that characterise the engines, is the specific impulse I_{sp}, which measures the efficiency of how the engine uses the air aspired. It is given by:

$$I_{sp} = \frac{F}{\dot{m}_a} = V_e - V_0 \tag{1.4}$$

thus strongly depends on the velocity at the exit. The only differences, in addiction to the overall working principle, are the values of those parameters: turbojets have in average $I_{sp} = 4000s$ whereas TurboFan have more than $10000s$ of specific impulse [5].
For the modern airlines, turbojets have been replaced in slower aircraft by turboprops because their better range-specific fuel consumptions and noise [7]. At medium speeds, where the propeller is no longer efficient, turboprops have been replaced by turbofans (Figure 1.2). They are the most modern variation of the basic Turbojet engine where the operative principle is similar the Turbojet. The particularity is that the core engine is surrounded by a fan in the front and an additional turbine at the rear. The fan and the low pressure turbine are composed of many blades, like the core compressor and core turbine, and are connected to an additional shaft. The incoming air is then captured by the engine inlet. Some of the incoming air passes through the fan and continues on into the core compressor and then the burner, where it is mixed with fuel and combustion occurs. The hot exhaust passes through turbine and then out the nozzle, as in a basic turbojet. The rest of the incoming air passes through the fan bypasses, or goes around the core engine, and contributes to the thrust. The air that goes through the fan has a velocity that is slightly increased from free stream and has high mass flow rate. So, a turbofan gets some of its thrust from the core and some of its thrust from the fan. The ratio of the air that goes around the engine to the air that goes through the core is called the bypass ratio.

In conclusion, the turbojet and turbofan are two common types of jet engines, and both are

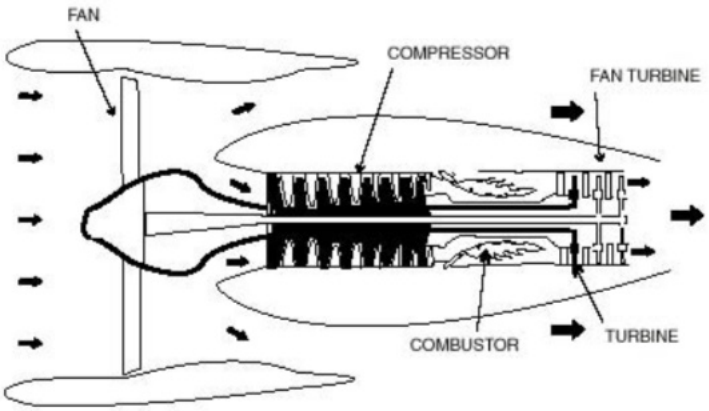

Figure 1.2: Turbofan engine sketch proposed by [5]

used in commercial and private aircrafts. The turbojet engine creates most of its thrust by the bypass of air through the jet engine, and the exhaust exiting the jet engine system. The turbofan jet engine creates most of its thrust by the fan blades located in the front of the jet engine.

For these engines categories, the combustion could be traded as deflagration, i.e. under nearly constant pressure conditions. The constant pressure consumption of reactants into products resulting in a high temperature gas which propagate at relatively low flame speeds $(1-30m/s)$ [1].

Brayton cycle

The Brayton (or Joule) cycle, where represents the cycle governing the thermodynamic process in turbojet and turbofan engines, is presented in Figure 1.3 with focus on $p-v$ and $T-S$ plots. The ideal Brayton cycle uses isentropic compression and expansion processes to transfer work to and from the system. As already said, this cycle represents the constant pressure heat addition of deflagration combustion. It consists of two constant pressure processes and two isentropic processes. Clearly, the total area indicates the availability of useful work for the engine. Tracing the path shown, the thermal efficiency of the cycle $\eta_{Brayton}$ is defined as the useful work output divided by the total heat energy input. It depends only on the temperature

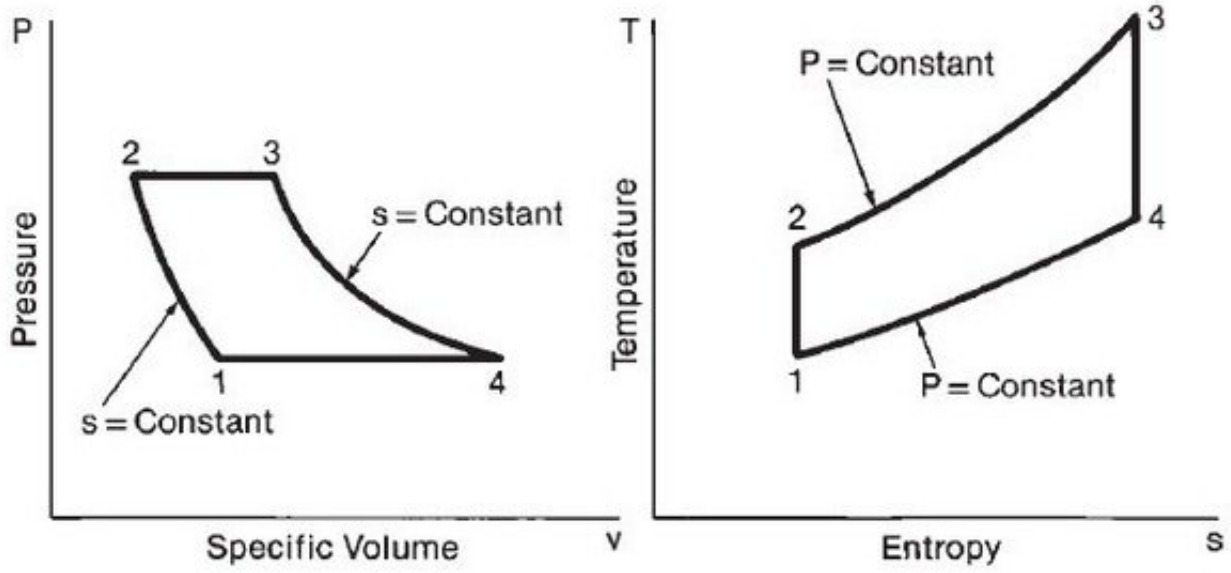

Figure 1.3: Ideal Brayton thermodynamic cycle [8].

change during either of the two isentropic compression or expansion processes, that is:

$$\eta_B = \frac{\text{Net work}}{\text{Heat in}} = \frac{C_p[(T_3 - T_2) - (T_4 - T_1))]}{C_p[T_3 - T_2]} = 1 - \frac{T_4 - T_1}{T_3 - T_2} = 1 - \frac{T_1}{T_2} = 1 - \left(\frac{P_1}{P_2}\right)^{\frac{\gamma-1}{\gamma}} \quad (1.5)$$

where γ is the heat capacity ratio.

From theoretical point of view, referring to the Equation 1.5, increasing T_2 the efficiency grows. Moreover, there is a limit for T_2, which is adiabatic flame temperature, and for pressure combustors that limit is almost reached. In fact, according to [9], the air transport is responsible for a daily consumption of 5 millions of oil barrels, amounting to 781 millions tons of $C0_2$ emission per year. Moreover, the mechanical components (like turbine and compressor) are composed by some metal alloys that have a low melting points (around 1100°C).

Moreover, despite of modern technologies, they have some limits: at M $>$ 3, compressed air reaches such extreme temperatures that compressor stage fan blades begin to fail and the turbine inlet temperature limits thrust. An available solution to extend the range of use is install an afterburner rear the turbine providing temporary increase in thrust, again leading to high fuel consumption.

A way to improve the thermal efficiency is adding heat at constant volume, the basic thermodynamic transformation of detonation engines.

1.2 Detonation Engines

Detonation engines burn propellant mixture through a nearly constant volume process to produce high chamber pressure (≈ 15-20 of high compression ratios) and thrust, while simultaneously using less fuel. Basically, they operate through the use of supersonic combustion rather than subsonic combustion of its fuel.

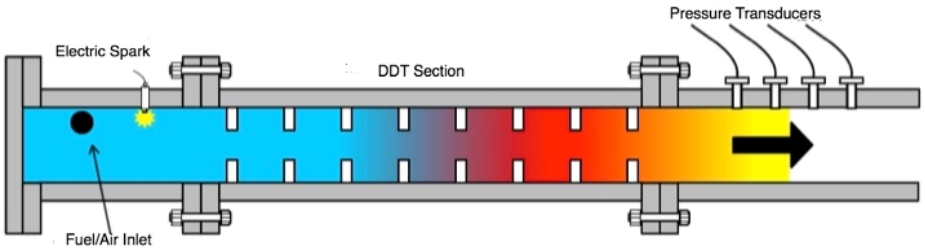

Figure 1.4: Configuration of a typical thrust producing PDE [10]

Detonation enables very rapid energy conversion which means high burning rate, that does not allow enough time for the local expansion of the combustion products to occur. Therefore, the detonation process is thermodynamically closer to a constant volume process. The higher thermodynamic efficiency of the nearly constant volume combustion process (detonation) is directly traceable with lower entropy rise in the working fluid, when compared to constant pressure (deflagration) combustion process. Then, the motivation for pursing development of detonation propulsion technologies reside in the inherent thermal efficiency of the detonation cycle that is traceable to the low entropy rise in the working fluid.

Before proceeding with technical discussions of the operating principles, theoretical description of deflagration and detonation will be provided.

The combustion, which is an exothermic chemical reaction between a fuel and an oxidiser that once initiated can sustain itself as long as the products are present in the proper proportions and thermal diffusion limits are not exceeded, is divided in two main phenomena that are depending on the velocity at which the combustion wave propagates. Each mode has its own characteristic behaviour which differs radically in their respective final thermodynamic states, depending on several factors including mixture composition, pressure, temperature. In gen-

eral, combustion occurs in terms of deflagration or detonation, first proof by Michelson using Rankine theory [11].

1.2.1 Deflagration

Deflagration is the common combustion phenomena associated with current propulsion systems such as ramjets and turbojets. A deflagration is a chemical reaction in which the heat output is sufficient to enable the reaction to proceed and be accelerated without input of heat from another source. The main characteristic is that the chemical reaction time scalar are comparable with the integral time scalar, in other words the flow velocity. This speed is dependent on the chemical composition, mass diffusion rates, and thermal transfer rates of the reactants[3]. Looking the principal variables across deflagration wave, the deflagration flame front gradually raises the temperature of the unburnt mixture before the onset of the chemical reaction. When the temperature exceeds the reaction activation energy, the reactants are slowly consumed giving rise to the products. Furthermore, the pressure varies slightly across the deflagration flame front: in fact across it, the pressure decreases while the volume increases.

1.2.2 Detonation

Detonation is a violent chemical reaction that proceeds through the combustion products towards the reactants at supersonic velocity. The supersonic combustion event propagates at high velocities[4] and produces a rapid combustion of the reactants due to the strong shock wave leading the detonation. In fact, contrary to the deflagration, across the detonation, the pressure increases while the volume decreases. Both phenomena, i.e. reactions and shock waves, proceed in a totally coupled and mutually supporting manner, and this is described by the Chapman-Jouget theory.

The crossroad of such researches was in 1883 when it was demonstrated that, under right conditions, deflagration would transition into a detonation wave, proving that the detonation process

[3] Typical flame speeds are 1 to 100m/s.

[4] Typical detonation waves propagate at velocity on the order of 2000m/s.

can be viewed as a rapid adiabatic reaction whose energy release drives the detonation wave. The combined work of D. L. Chapman and E. Jouget shown the relationship between velocities of combustion wave processes and the pressure at which they occur. There exists a minimum velocity in which a detonation can occur, and it is thermodynamically tied to the properties of the burned gas. There is also a relation that the detonation wave velocity is equal to the sound velocity of the burned gas in which it propagates. This process can be described by the one dimensional Chapman-Jouguet (CJ) theory and the ZND model, which postulates that there are two regions at which combustion process can occur.

Chapman-Jouguet theory

The CJ model uses a control volume surrounding a planar shock wave to determine the gas dynamics properties after the wave from those before it. Assuming a steady, one dimensional flow in a constant combustion area, with no external heat added, negligible diffusion effects and no viscous effects, the Hugoniot relationship can be derived from the conservation equations.

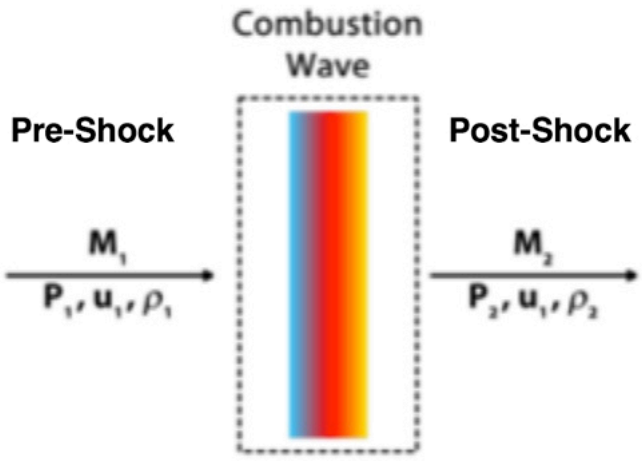

Figure 1.5: Control volume used in CJ Model [10]

By analysing the detonation as a supersonic shock wave, conservation equations lead to[5]:

$$\begin{aligned} \rho_1 w_1 &= \rho_2 w_2 \\ P_1 + \rho_1 w_1^2 &= P_2 + \rho_2 w_2^2 \\ h_1 + \frac{w_1^2}{2} &= h_2 + \frac{w_2^2}{2} \end{aligned} \tag{1.6}$$

The Hugoniot curve, defined by the relationship between enthalpy h, pressure p, and density ρ, provides the locus of possible solutions for state 2 (from a given state 1) and gives the energy release:

$$h_2 - h_2 = \frac{1}{2}(V_1 + V_2)(p_2 - p1) \tag{1.7}$$

On other hand, Rayleigh provides the relation between heat addition and the gases initial and final pressures and densities:

$$\frac{\gamma}{\gamma - 1}\left(\frac{p_2}{\rho_2} - \frac{p_1}{\rho_1}\right) - \frac{1}{2}(p_2 - p_1)\left(\frac{1}{\rho_1} + \frac{1}{\rho_2}\right) = q \tag{1.8}$$

The intersection between the previous curves describes the different conditions at which combustion can occur, as shown in Figure 1.6. These combustion conditions include various strengths of deflagration and detonations, dependent upon the pressure and specific volume conditions at which the event is occurring.

The CJ points, shown by CJ_U and CJ_L, are the boundaries for strong and weak combustions. For constant area combustion tubes, the maximum flow velocity is limited to the sonic velocity of the burned gas. Although the detonation wave propagates and consumes the reactants at supersonic velocity, the flow of the combustion products away from the detonation wave is limited to Mach 1, relative to the wave [12]. These CJ conditions can be easily calculated by

[5] "1" for front state whereas "2" for back state

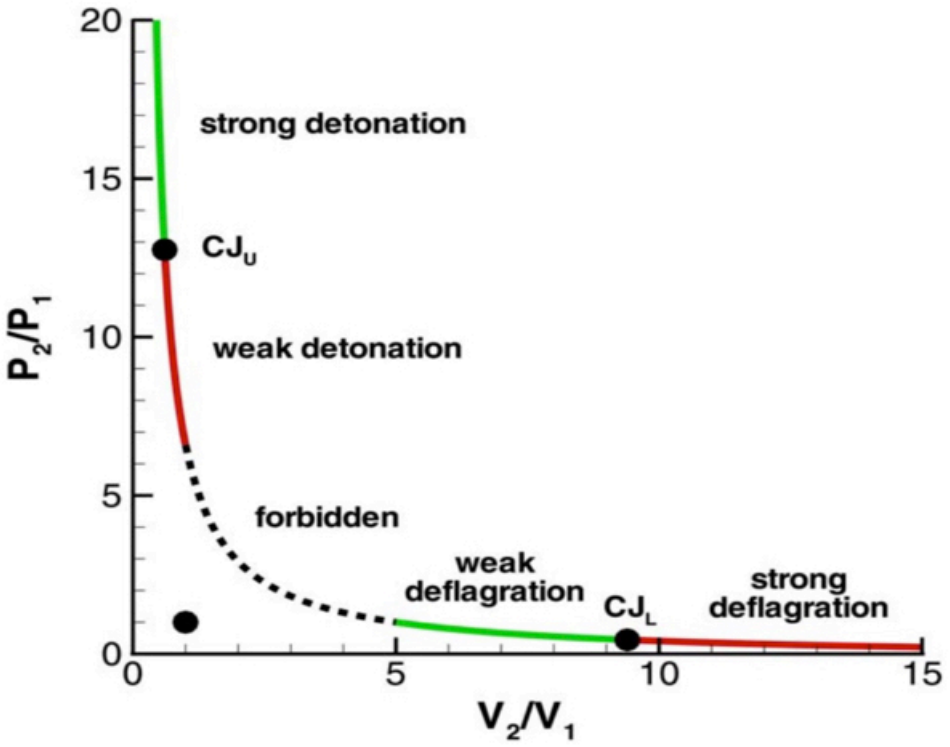

Figure 1.6: Hugoniot curve

using Cantera program [13], some of those reported on following:

$$\begin{aligned} \frac{P_2}{P_1} &= \frac{\gamma M_{CJ}^2 + 1}{\gamma + 1} \qquad U_{CJ} = M_{CJ} C_1 \\ \frac{\rho_2}{\rho_1} &= \frac{(\gamma+1) M_{CJ}^2}{1 + \gamma M_{CJ}} \qquad u_2 = U_{CJ}\left(1 - \frac{\rho_2}{\rho_1}\right) \end{aligned} \tag{1.9}$$

Table 1.1 below shows some sample data for hydrogen, methane, propane and acetylene. On average, air-fuel mixtures produce a significantly lower pressure and temperature ratio as well as lower detonation velocities when compared to the same mixtures although both result in pressure and temperature ratios ten or more times greater than ambient conditions.

Mixture	P/P_1	T/T_1	ρ/ρ_1	M_{CJ}	U_{CJ} [m/s]
Hydrogen-Air	15.8	10	1.8	4.9	1965
Methane-Air	17.4	9.4	1.8	5.1	1800
Propane-Air	18.4	9.6	1.8	5.3	1796
Acetylene-Air	19.3	10.6	1.8	5.4	1864

Table 1.1: Typical Hydrocarbon CJ parameters (1bar, 295K)

1.2.3 Humphrey cycle

Since both detonation engines, which their working principle will be described below, are based on minimising the entropy rise in the working fluid using detonation waves to generate thrust, the detonation can be modelled as constant volume transformation[6]. Thus, they can be summarised as Humphrey cycle from the thermodynamic point of view.

This cycle represents the constant volume heat addition of the detonation combustion process. As shown in Figure 1.7, the cycle is similar, except that the constant volume pressure combustion process of the Brayton cycle, is replaced by a constant volume heat addition process [14]. With the same analysis of the cycle efficiency, the efficiency of the Humphrey cycle is given by:

$$\eta_{Humphrey} = 1 - \gamma \frac{T_0}{T_2} \left[\frac{\left(\frac{T_3}{T_2}\right)^{\frac{1}{\gamma}} - 1}{\frac{T_3}{T_2} - 1} \right] \tag{1.10}$$

The efficiency of this cycle depends not only on the isentropic compression temperature ratio T_0/T_2 but also on the ratio of specific heat γ and temperature change due to the constant volume combustion (i.e. the detonation temperature ratio T_3/T_2).

The difference between the Brayton (Equation 1.5) and Humphrey (Equation 1.10) cycle efficiencies is the following T_1/T_2 multiplier:

$$\gamma \left[\frac{\left(\frac{T_3}{T_2}\right)^{\frac{1}{\gamma}} - 1}{\frac{T_3}{T_2} - 1} \right] \tag{1.11}$$

The value of this expression is always less than one for detonation combustion. As a result, the efficiency of a Humphrey cycle is greater than the efficiency of the Brayton cycle [15, 16]. Figure 1.8 provides the calculation of cycle thermal efficiency as a function of compression ratio, P_2/P_1. The actual detonation cycle efficiency lies somewhere between the two limiting specific heat curves ($\gamma = 1.4$ and γ=1.16). At a compression ratio of 6, the constant volume process

[6] One can say that the expansion cannot take place.

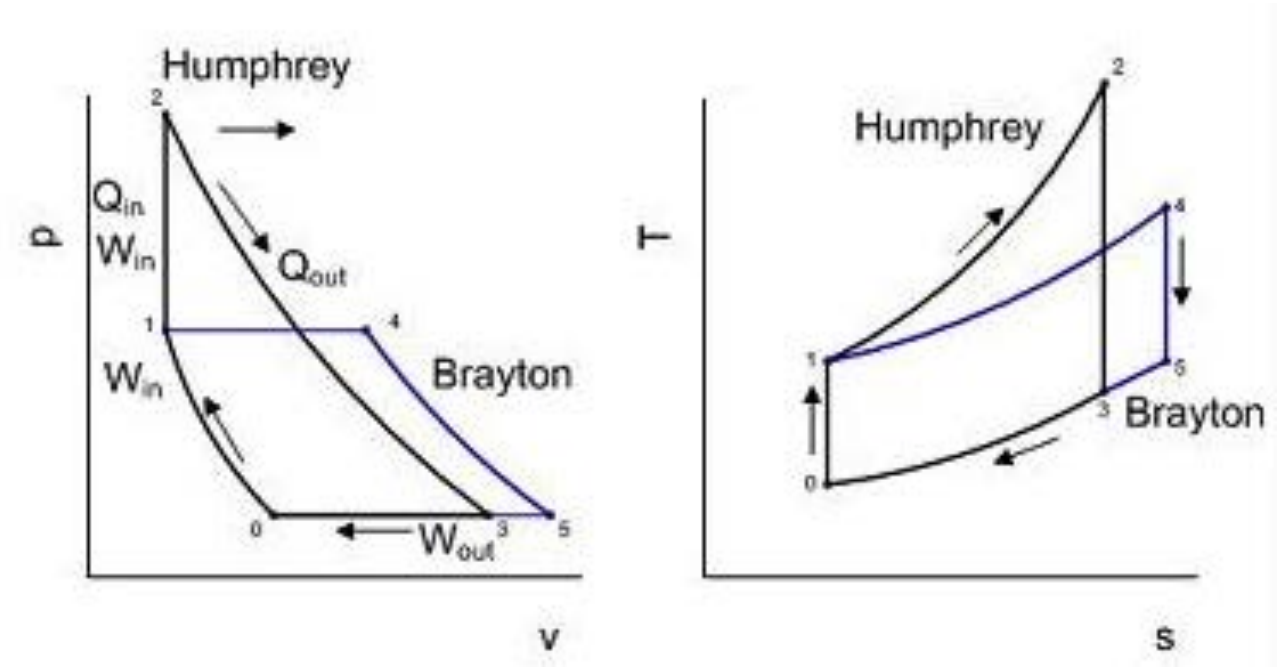

Figure 1.7: Comparison between Brayton and Humphrey cycle

offers from 30% to 50% improvement in thermal cycle efficiency over the constant pressure cycle [15, 16]. Thus, the thermodynamic efficiency of the detonation cycle is close to that of the constant volume cycle, and significantly better than that of the constant pressure cycle.

1.2.4 Zeld'ovich-Von Neumann-Doring cycle

Actually, the previous thermodynamic cycle described above, is just a simplification where fresh mixture reacts infinitely fast. A more realistic cycle is the Zeld'ovich Von Neumann Doring cycle (ZND cycle), which states that chemical reactions occur at a finite speed, introducing reaction kinetic, and the conditions behind the leading shock wave differ from the CJ final equilibrium conditions. Table 1.2 shows the qualitative differences.

Mixture	P/P_1	T/T_1	ρ/ρ_1
Hydrogen-Air (CJ)	15.8	10	1.8
Hydrogen-Air (ZND)	27.4	5.1	5.4

Table 1.2: ZND vs CJ properties

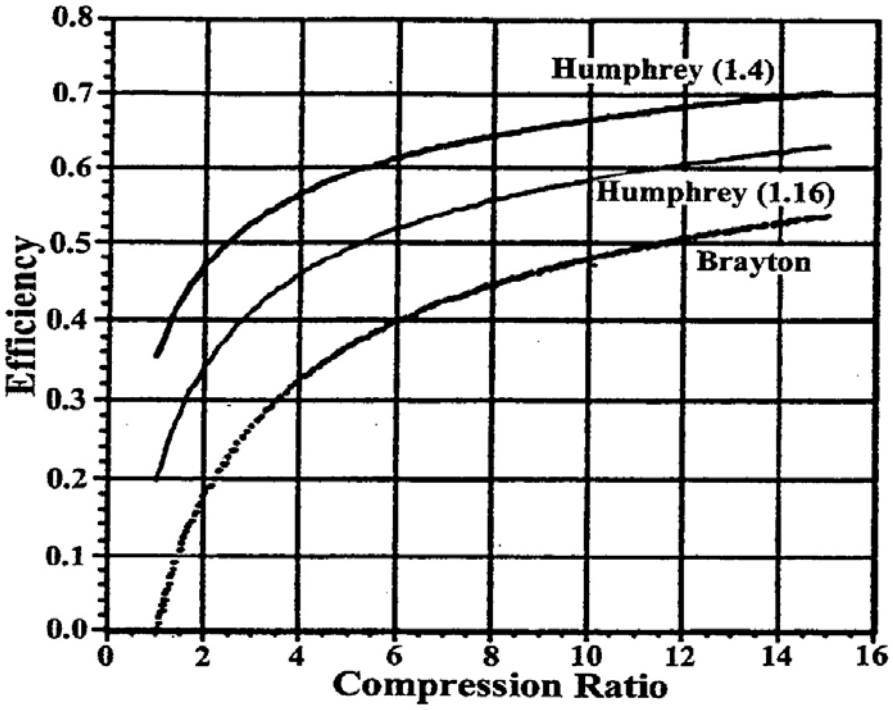

Figure 1.8: Thermodynamic Efficiency of Brayton Isobaric and Humphrey Detonation Cycles for Stoichiometric Hydrogen/Air [15]

Detonation combustion wave properties, as shown in Figure 1.9, for a detonation propagating in a tube filled with a combustible gas mixture can be modelled as a strong shock that rapidly compresses the reactants to initiate combustion, and a thin flame front in which heat addition occurs. The shock front moves at the detonation velocity relative to the gas and dramatically increases the temperature and pressure. The region of unburnt gas immediately behind the shock is a stable high-pressure region, known as the Von Neumann spike. This region represents the ignition delay, and its width is dictated by chemistry kinetics of the gas mixture. Once the chemical reaction is initiated heat is added to the flow causing to the temperature to increase and to pressure to decrease. The pressure and density in a stable detonation wave are significantly lower than in the Von Neumann region between the shock front and the chemical reaction zone.

The detonation can be viewed as three district regions whose width are dependent on the equivalence ratios and kinetics of the gas mixture. In the first region, the shock wave delivers a tremendous amount of energy into the unburned reactants. The dramatic increase in the

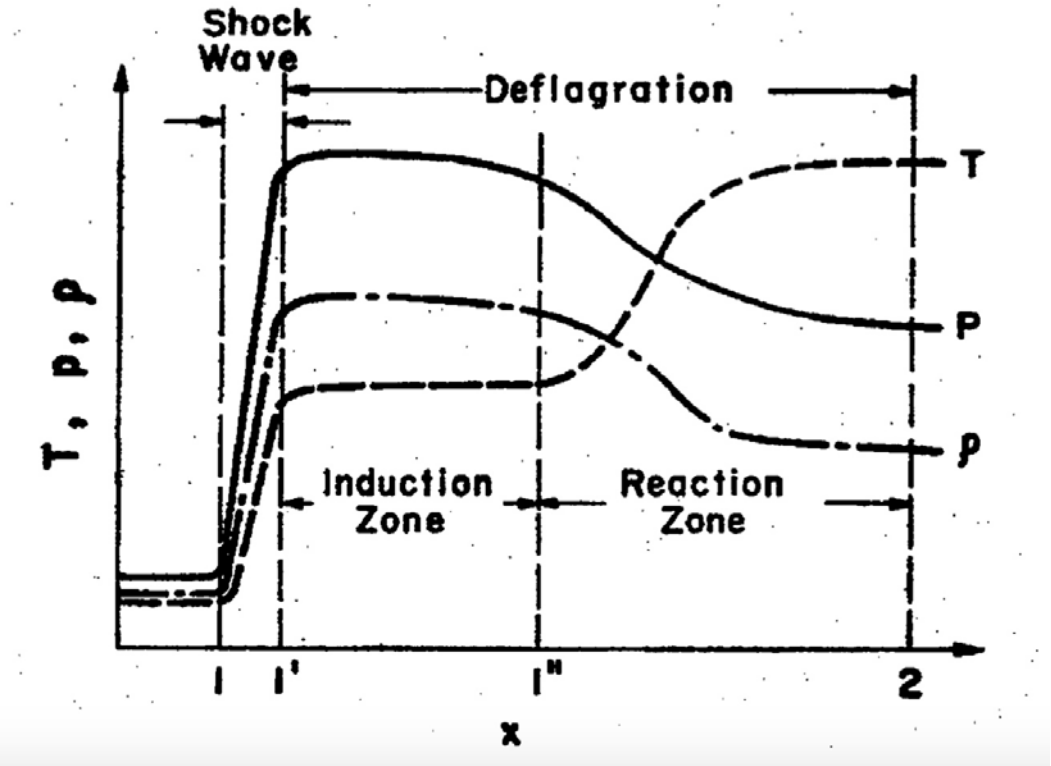

Figure 1.9: Physical properties of 1-D detonation wave structures [1]

thermodynamic properties of the gas mixture increases the chemical reaction rates and accelerates the energy release phase of the wave structure. On other hand, the deflagration region consists of two zones that describe the thermodynamics of combustion the reactants. In the first (induction zone) the chemical reaction is beginning but is not yet impacting the thermodynamic properties of the mixture. In the reaction zone, the reaction rate begins to increase exponentially.

Table 1.3 shows a qualitative comparison between deflagration and detonation, for 1D stationary analysis.

Property ratios	**Deflagration**	**Detonation**
Wave velocity ratio	0.0001-0.03	5-10
Reactant velocity ratio	4-6	0.4-0.7
Pressure ratio	0.98	13-55
Temperature ratio	4-16	8-21
Density ratio	0.06-0.25	1.7-2.6

Table 1.3: Qualitative difference between deflagration and detonation [1].

For a H_2-Air mixture, the different theoretical efficiencies can be calculated. This is visible in Figure 1.10, where efficiency calculations are taken from Heiser & Pratt, 2002 [17]. At the end, the ZND cycle has a greater efficiency than the Humphrey cycle due to the fact that it takes into accounts the frozen shock [18].

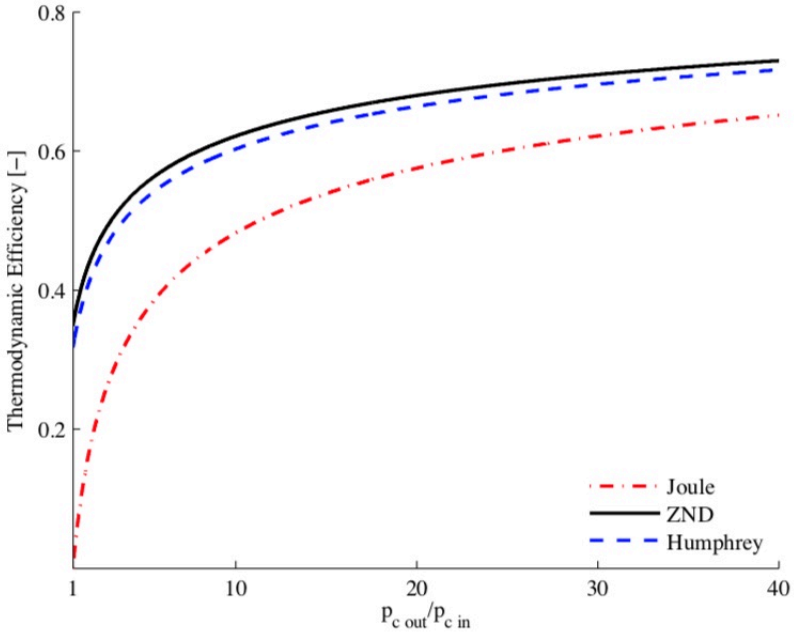

Figure 1.10: Comparison of the efficiency of three different cycles for a given heat value [19].

1.2.5 Detonation cells

Although the one-dimensional ZND model works well for approximating detonation wave, in actually the detonation wave has a complex 3D structure. This structure is the result of transverse shock wave that propagates laterally behind the leading normal shock wave.

As shown theoretically in Figure 1.11, the intersection of the transverse waves with the leading normal shock wave results in localised high-pressure, high-temperature regions known as triple points. The extreme high heating that occurs at these points greatly accelerates the local reaction rates and ensures that the heat release region is closely coupled to the leading normal shock wave. The rapid oscillation of the triple points across the leading shock wave promotes the

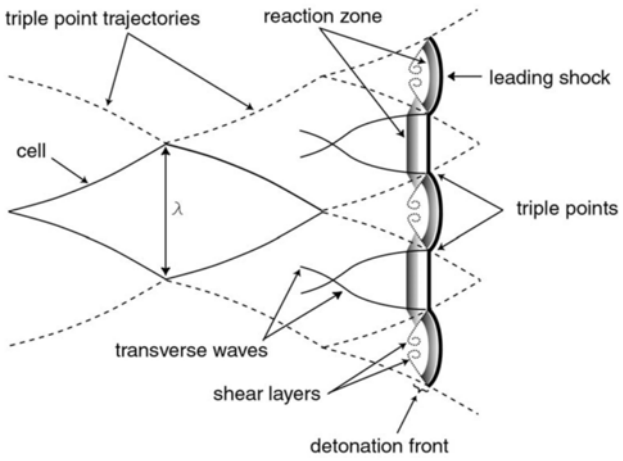

Figure 1.11: Theoretical hydrogen-air detonation wave structure [20].

stability of the detonation wave and results in the characteristic fish scale patterns. Hence, these

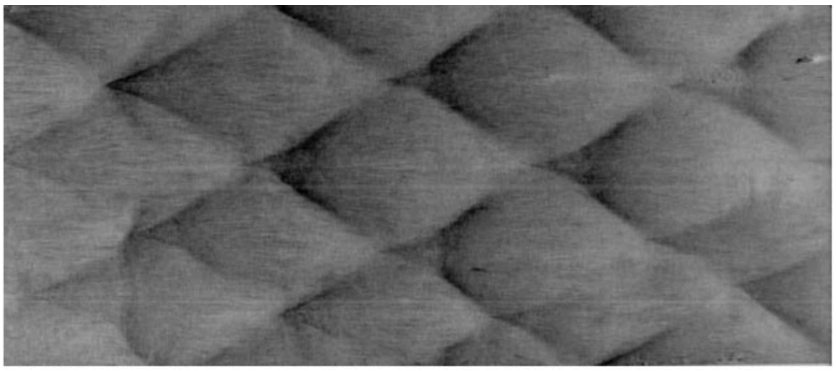

Figure 1.12: Experimental hydrogen-air detonation wave structure [20].

detonation cells are then a natural phenomenon due to complex fluid interaction. Therefore, observations from experimental reveal that detonation cells appear whenever detonation in taking place, leading to good indicator for understanding if the flow has reached detonation conditions. The cell width is the maximum distance between triple points and is representative of the sensitivity of the mixture to detonation. In fact, many of the dynamic parameters of detonations are largely affected by the cell size and because it is one of the most readily observable aspects of the wave, it is used in empirical relations for critical tube diameter, critical energy and minimum tube diameter. Mixtures with small cell widths are more sensitive and likely to detonate than mixtures with larger cell widths. The cell size can be approximated by the formula $\lambda = Al$ where l is the induction zone length and A is an empirical proportionality constant, which varies strongly with the equivalence ratio. A plot of typical detonation width

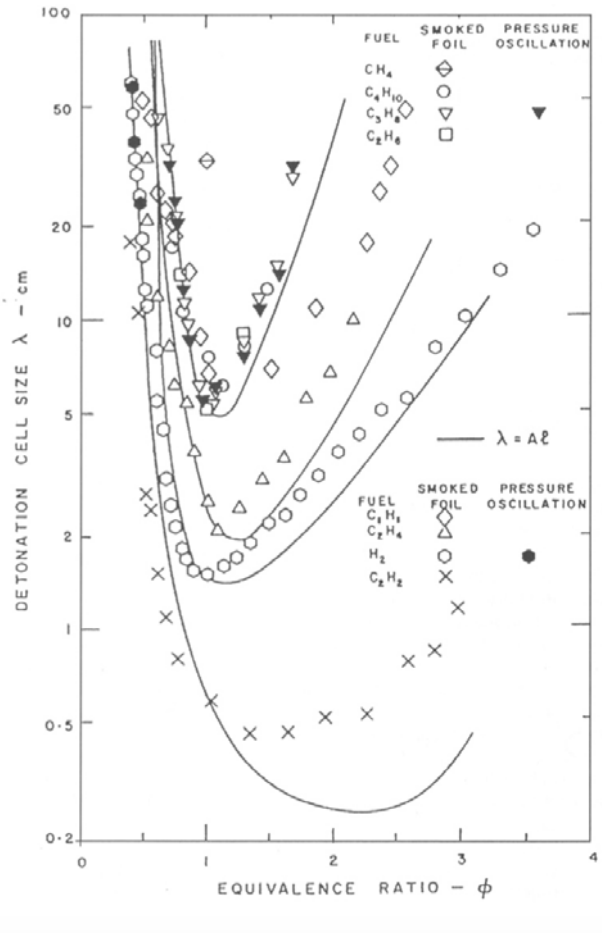

Figure 1.13: Cell size vs Equivalence Ratio [21].

values are presented in Figure 1.13.

1.3 Classes of detonation engines

Pulse Detonation Engines

The first type of detonation engines is the pulse detonation engine, also known as "PDE". In the PDE combustor, the detonation cycle is periodically started with an ignition system operating at a certain frequency [22], as shown in Figure 1.14. In the first phase (a), the tube is totally filled with fresh mixture and is ignited by an ignition source (b). Selections of a fuel and oxidiser affect net thrust or work produced by a PDE cycle to the large variation in detonation velocities, compression ratios and temperatures. It is typically best to use gaseous

form reactants because of their lower detonation energy requirements. In the third phase (c) the detonation wave is consuming all the reactants and arrives at the exit (d), providing thrust. In some situations the energy required for direct initiation of detonation may be prohibitively high. In order to promote this DDT, the tube can be filled by notches for pushing that transition. In the last phase (e), the tube is refilled and the whole process starts again. Each phase in the process is distinct and segmented, and every detonation wave must be individually ignited.

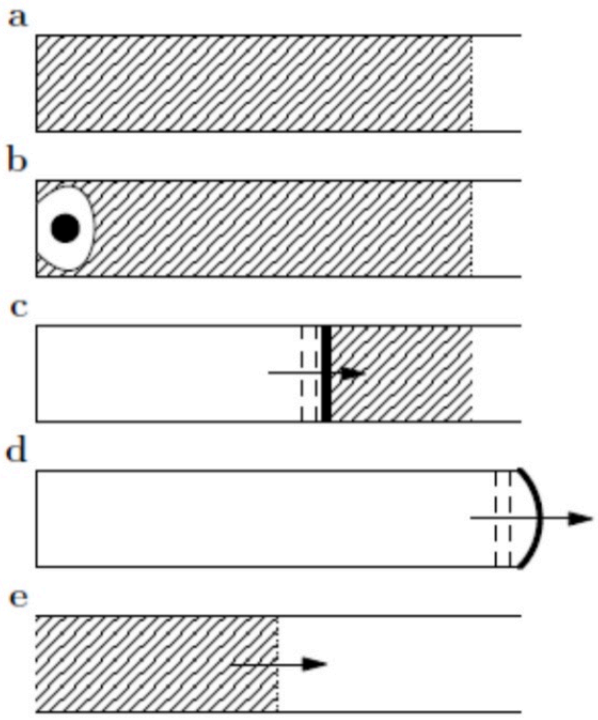

Figure 1.14: Operating principle of pulsed detonation engine [23].

Rotating Detonation Engines

The other type of detonation engines is the rotating detonation engine, also known as "RDE". The rotating detonation engine is fundamentally different from traditional detonation engines in that is does not rely on pulsed combustion but rather a continuously rotating detonation wave. So, the engine offers a continuous combustion of the reactants through a swirling detonation wave motion in an annuls shaped combustor, where the working principle is explained in Figure 1.15. Fresh mixture is continuously injected into the inlet of the combustor (1) and

the blue zone represents the fresh mixture that is awaiting to be consumed by the detonation front(3). This front moves in a transverse way whereas the consumed products travel in an axial way to the exit (6). The oblique shock travels through the burnt mixture (5). This configuration has the ability to provide continuous detonation level pressure at the exhaust if a stable detonation can be maintained. A detonation still has to be initiated externally and then directed into the channel but does not require continuous pulsing. This concept has already

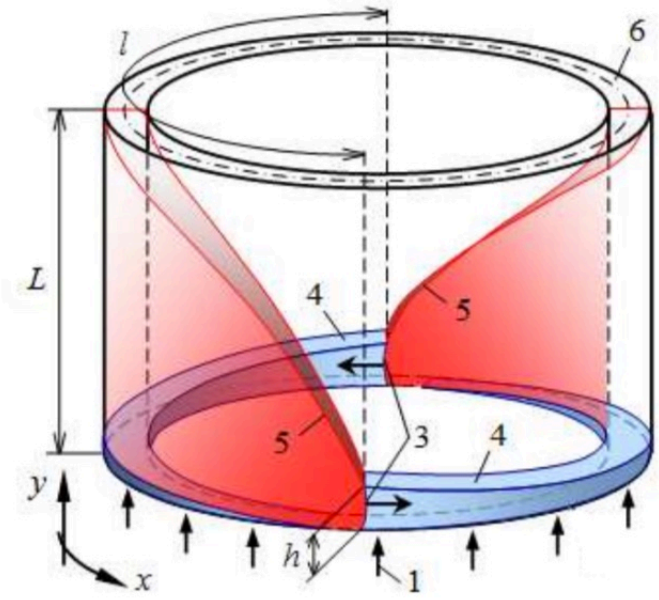

Figure 1.15: Continuous detonation engine operating principle [22].

been introduced by Voitsekhovskiil in 1569 [24] but due to the complexity of this process, the concept is still under studying. Clearly, the advantaged of this type instead of other lies in the fact that detonation does0 not have to be initialised in each cycle, the injection of fresh mixture is simultaneous and the engine is more compact [20].

1.4 Reaction mechanisms

The combustion phenomenon is a complicated natural effect which involves different chemical reactions between any combustible flow and an oxidiser to form an oxidised product.
For simulating the combustion, and then for calculating the production and heat release terms in the governative equations, the Arrhenius coefficients and the different chemical reactions are

stored on suited mechanisms, shown in appendix B. From the physical point of view, these could be treated in two different ways: reduced and detailed. On the first cases, only few reactions are involved on the mechanism trying to simulate the complete combustion. On other hand as detailed when the mechanism describes events on molecular level. Clearly, ideally full chemistry needs to be used in the DDT simulations, using for instance 9 species and 21 reactions [25]. For the simulations of the most shock tube tests, the computational mesh would need to be in the order of million to even tens of million because of the size of the tubes. It would be computationally too expensive to use detailed kinetic schemes. Then, also single step chemistry model is taken into account as viable alternative and the effects are compared with the effects coming from the detailed ones.

The solver that will be described is able to work with any scheme of reactions, from the reduced to the detailed one. Certainly, one-step chemistry model (reduced) is sufficient in replicating and predicting re-initiation of detonations however it has some other limitations. For instance, due to the absence of a loss mechanism, it cannot give the critical initiation energy and detonation limits. Instead, detailed chemistry is capable of reproducing some of the finer details [26], as for example the detonation cells. For all the kinetic models, the combustion process is taken into account by transport equations for species, appropriate source terms for its production/consumption and heat release by fuel burning. Basically, the approach is the following:

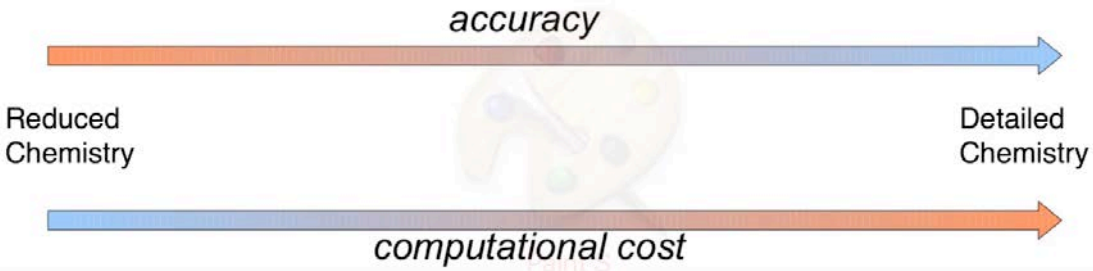

Figure 1.16: Sketch of the reaction mechanisms behaviour.

1.5 Aim of the Thesis

Due to the absence of open source solvers able to simulate the DDT process in detonation engines from the detailed point of view, the aim of this research is to outline the implementation of the new solver able to simulate the pressure gain combustion phenomena within detonation engines, including both deflagration and detonation modes. A critical issue for realising this solver is the completely different dynamics of the flow, leading to different numerical implementations capable to handle their main effects. In order to verify the numerical consistency of the algorithms implemented, the solvers have been tested on different applications: different computational domains, different mesh grid sizes and different mixtures have been taken into consideration, both homogeneous and inhomogeneous. The objective of this thesis is then showing the numerical approaches used to overcome these issues, yielding to a more precise agreement between experimental and numerical results, using different types of reaction mechanisms.

1.6 Structure of the Thesis

In the chapter 2 the governative equations, the structure of the solvers, the numerical approaches as well as a detailed description of the verification test cases are provided. Chapter 3 presents all the results performed using these solvers. First of all, results coming from shock tube, in order to test the capability of the density-based solver, are showed. Moreover, two dimensional simulations of H_2-Air mixture using reduced and detailed reaction scheme are performed together with a comparison against experimental data. Furthermore, simulation using only a detailed scheme of C_2H_2-Oxygen mixture is provided. Finally, for both mixtures, investigations about detonation waves and their cellular structures are presented. At the end, chapter 4 presents the main results of this work with focus on future works using the same methodologies. In the appendix theoretical and experimental CJ velocities, reaction mechanisms and further numerical results are provided.

Chapter 2

Methodology

2.1 Governing equations

Detonation is a transient phenomenon and then, time dependent partial differential equations are needed in order to solve the flow dynamic, as already written on subsection 1.2.2 [27, 11]. Generalised by the Reynolds Transport Theorem [28], mass and momentum conservation equations for compressible flows, by using both Newtonian's and Stokes's hypothesis, are given by [29]:

$$\frac{\partial \rho}{\partial t} + \frac{\partial (\rho u_i)}{\partial x_i} = 0 \tag{2.1}$$

$$\frac{\partial (\rho u_i)}{\partial t} + \frac{\partial (\rho u_i u_j)}{\partial x_j} = -\frac{\partial p}{\partial x_i} + \frac{\partial \tau_{ij}}{\partial x_j} + \rho f_i \tag{2.2}$$

where ρ is the density [mass/volume], $\vec{u}$ is the three dimensional velocity of the flow, p is the static pressure, $\vec{f}$ represents the body forces per unit volume acting on i-direction and $\vec{\vec{\tau}}$ is called *viscous tensor*, which represents the deviatoric component of the total stress tensor σ, that is defined by:

$$\tau_{ij} = -\frac{2}{3}\mu \frac{\partial u_k}{\partial x_k}\delta_{ij} + \mu \left(\frac{\partial u_i}{\partial x_j} + \frac{\partial u_j}{\partial x_i} \right) \tag{2.3}$$

where μ is the dynamic viscosity whereas δ_{ij} is the Kronecker delta [30].

Basically, Equation 2.1 states that the mass in the system cannot disappear nor being created

whilst Equation 2.2 is based upon the Newton's law for a continuum [30].

For the conservation of energy, that it will described more detailed in the next sections, the *stress tensor* σ is defined as:

$$\sigma_{ij} = \tau_{ij} - p\delta_{ij} \tag{2.4}$$

2.1.1 Species properties

Combustion involves multiple species reacting through multiple chemical reactions. The Navier-Stokes equations apply for such multispecies-multireaction gases require some additional terms. In order to provide those terms, definitions of chemical and thermodynamic variables are needed.

Chemical Species

Chemical species are characterised through their mass fractions Y_k, that is:

$$Y_k = \frac{m_k}{m} \tag{2.5}$$

for k = *1,...,N* where N is the number of species in the reacting mixture. The mass of species present in a given volume V is indicated by m_k whilst the total mass of gas in this volume is m.

Going from non reacting flow to combustion, it requires solving for $N + 5$ variables instead of 5. Knowing that the most chemical schemes involve a large number of species (e.g. N is larger than 50 for most simple hydrocarbon fuels), this is the first significant effort needed to compute reacting flows: increase the number of conservation equations to solve.

Thermochemistry

Considering a mixture of N perfect gases, the total pressure is the sum of partial pressures:

$$p = \sum_{k=1}^{N} p_k \quad \text{considering} \quad p_k = \rho_k \frac{R}{W_k} T \tag{2.6}$$

where T is the static temperature, R is the perfect gas constant, $\rho_k = \rho Y_k$ and W_k are respectively the density and the atomic weight of species k. Total density ρ of the multi-species gas can be assumed as:

$$\rho = \sum_{k=1}^{N} \rho_k \tag{2.7}$$

leading to the ideal gas law, that is:

$$p = \rho \frac{R}{W} T \tag{2.8}$$

where W is the mean molecular weight of the mixture:

$$\frac{1}{W} = \sum_{k=1}^{N} \frac{Y_k}{W_k} \tag{2.9}$$

As already said, the flow in question must be regarded as compressible; from the numerical point of view, it requires two more equations in order to be solved: the state equation for perfect gases and the energy conservation equation. For reacting flow, there are multiple possible variables to define the latter case, e.g. in terms of internal energy or enthalpy. For both of cases, the energy conservation states that the total energy and/or total enthalpy of an isolated system remains constant, i.e. it is not created or destroyed but is transformed from one form to another.

In order to be as general as possible, both approaches will be described. Starting with the classical definition of specific enthalpy h_k of species k, this is defined as the sum of sensible and chemical enthalpy:

$$h_k = h_{s,k} + h_{c,k} = \int_{T_0}^{T} C_{p,k} dT + \Delta h^0_{f,k} \tag{2.10}$$

where T_0 is the reference temperature, C_p is heat capacity at constant pressure and $\Delta h^0_{f,k}$ is the mass enthalpy of formation of species k. So, the sensible enthalpy h_s of specie k is given directly by:

$$h_{s,k} = \int_{T_0}^{T} C_{p,k} dT \tag{2.11}$$

that is zero at $T = T_0$ for all substances.

Furthermore, the sensible energy of species k is defined to satisfy the following equations: $h_{s,k} = e_{s,k} + p_k/\rho_k$. Clearly, this choice requires the introduction of the RT_0/W_k term into $e_{s,k}$

definition. The energies and enthalpies, previous defined, are mass quantities: for example, the formation enthalpy $\Delta h^0_{f,k}$ for the species k is the enthalpy needed to form $1Kg$ of species k at the reference temperature T_0. These values are linked to molar ones $\Delta h^{0,m}_{f,k}$ by:

$$\Delta h^0_{f,k} = \Delta h^{0,m}_{f,k}/W_k \tag{2.12}$$

Examples of magnitudes of these reference values, $\Delta h^0_{f,k}$ and $\Delta h^{0,m}$, are listed on Table 2.1.

Substance	W_k (Kg/mole)	$\Delta h^0_{f,k}(KJ/Kg)$	$\Delta h^{0,m}_{f,k}(KJ/mole)$
H_2O	0.018	-13435	-241.8
O_2	0.032	0	0
H_2	0.002	0	0
CH_4	0.016	-4675	-74.8
N_2	0.028	0	0
CO_2	0.044	-8943	-393.5

Table 2.1: Formation enthalpies at $T_0 = 298.15K$

The heat capacities at constant pressure $C_{p,k}$ of species k are mass heat capacities related to molar capacities by $C^m_{p,k}$ by $C_{p,k} = C^m_{p,k}/W_k$. Still considering perfect diatomic gas, these can be linked each other by:

$$C^m_{p,k} = 3.5R \quad \text{and} \quad C_{p,k} = 3.5R/W_k \tag{2.13}$$

In practice, the changes of $C^m_{p,k}$ with temperature are large in combustion flows, thus an approximation is needed in order to reduce both computational cost and numerical issue (section 2.3). On Figure 2.1 are shown the trends of the mass heat capacities at constant pressure for different chemical species. Using the same approach, the mass heat capacities at constant volume $C_{v,k}$ are related to the $C_{p,k}$ by:

$$C_{p,k} - C_{v,k} = R/W_k \tag{2.14}$$

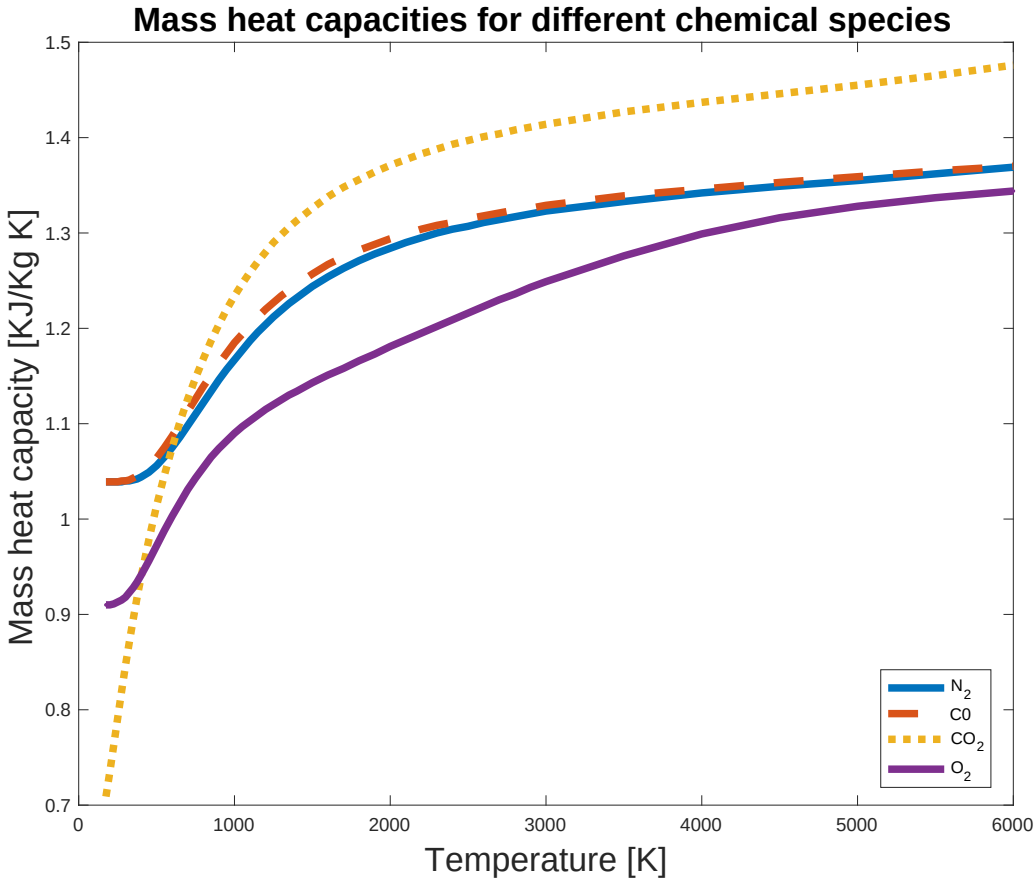

Figure 2.1: Mass heat capacities at constant pressure of CO_2, CO, O_2 and N_2

Then, the total internal energy e for the mixture can be defined as well in term of $C_{v,k}$ by:

$$
\begin{aligned}
e = \sum_{k=1}^{N} \left(\int_{T_0}^{T} C_{p,k} dT - RT/W_k + \Delta h^0_{f,k} \right) Y_k = \\
= \sum_{k=1}^{N} \left(\int_{T_0}^{T} C_{v,k} dT - RT/W_k + \Delta h^0_{f,k} \right) Y_k \\
= \int_{T_0}^{T} C_v dT - RT_0/W + \sum_{k=1}^{N} \Delta h^0_{f,k} Y_k = \sum_{k=1}^{N} e_k Y_k \quad (2.15)
\end{aligned}
$$

where the correlation between internal energy and enthalpy, that is $e = h - p/\rho = \sum_{k=1}^{N} h_k Y_k - p/\rho$ has been used.

In conclusion, the heat capacity at constant pressure C_p of the mixture is given by:

$$C_p = \sum_{k=1}^{N} C_{p,k} Y_k = \sum_{k=1}^{N} C_{p,k}^m Y_k / W_k \tag{2.16}$$

Equation 2.16 shows that the mixture heat capacity C_p is a function both temperature T and composition Y_k and, clearly, it may change significantly from one point to another. However, in most hydrocarbon/air flames, the properties of nitrogen dominate[1] and the mass heat capacity of mixture is very close to that of nitrogen[2]. So, the C_p of the mixture is assumed to be constant along the whole process. As one can see on Figure 2.1, the C_p of N_2 does not change dramatically within the temperature range.

To be thorough, the heat capacity at constant volume C_v of the mixture is defined as:

$$C_v = \sum_{k=1}^{N} C_{v,k} Y_k = \sum_{k=1}^{N} C_{v,k}^m Y_k / W_k \tag{2.17}$$

similar to what was done previously.

Diffusion parameters

Since the combustion is also a diffusion process, all kinds of diffusion must be taken into account. The heat diffusion coefficient is called λ whilst the diffusion coefficient of species k in the rest of the mixture is called D_k[3]. Since solving the diffusion problem in a multi-species gas is a problem in itself, one can use a simplified version: the Fick's law.

The diffusion coefficient D_k for the species k is characterized in terms of Lewis number defined by:

$$Le_k = \frac{\lambda}{\rho C_p D_k} = \frac{\alpha}{D_k} \tag{2.18}$$

where $\alpha = \lambda/(\rho C_p)$ is the heat diffusivity coefficient. From the physical point of view, this parameter compares the diffusion speeds of heat and species k. Without losing generality, λ can be kept constant [31] and the magnitude of Le_k equal to one since it is important only for

[1] Molar fraction of N_2 in air is equal to 78.08%

[2] This value changes only from 1000 to 1300 J/(Kg K) when temperature goes from 300K to 3000K

[3] Used by Fick's law

laminar flames[4].

Other important parameters are the Prandtl number P_r, which compares momentum and heat transport, and the Schmidt number, which compares momentum and mass diffusivity:

$$P_r = \frac{\nu}{\lambda/(\rho C_p)} \quad \text{and} \quad S_c = \frac{\mu}{\rho D_k} \tag{2.19}$$

Other assumptions as Soret (molecular species diffusion due to temperature gradients) and Dufour (heat flux due to species mass fraction gradients) effects will be neglected.

2.1.2 Chemical Kinetics

For the combustion, the chemical kinetic plays a fundamental role because is responsible of the rates of chemical reactions which occur along the phenomenon. Chemical kinetics also includes investigations of how different experimental conditions can influence the speed of a chemical reaction and yields information about the reaction mechanisms and transition states.

The chemical kinetics concerns with understanding the rates of chemical reactions and is to be contrasted with thermodynamics, which deals with the direction in which a process occurs but in itself tells nothing about its rate. One can say that thermodynamics is times arrow, while chemical kinetics is times clock. A chemical reaction is, by definition, one in which chemical substances are transformed into other substances, which means that chemical bonds are broken and formed so that there are changes in the relative positions of atoms in molecules [11]. At the same time, there are shifts in the arrangements of the electrons that form the chemical bonds. The detailed mechanism by which a chemical process occurs is referred to as the reaction mechanism.

The vast amount of work done in chemical kinetics has led to the conclusion that some chemical reactions go in a single step[5] and other reactions go in more than one step (multi-step). Measurements of the rates of chemical reactions over a range of conditions can show whether a reaction proceeds by one or more steps. If a reaction is stepwise, kinetic measurements provide

[4] Only few milliseconds over tens of milliseconds for most simulations

[5] These are known as elementary reactions.

evidence for the mechanism of the individual elementary steps.

The parameter that drives these analyses is the reaction rate. It is defined in terms of the rates with which the products are formed and the reactants (the reacting substances) are consumed. The rate can then be defined as the concentration of a substance that is consumed or produced in unit time.

Numerical Modelling of Reaction Rate

Consider a chemical system of N species reacting through M reactions, mathematically defined by:

$$\sum_{k=1}^{N} \nu'_{k,j} \mathcal{M}_k \rightleftharpoons \sum_{k=1}^{N} \nu''_{k,j} \mathcal{M}_k \quad \text{for} \quad j = 1, M \tag{2.20}$$

where $\mathcal{M}_k$ is the symbol for species k, $\nu'_{k,j}$ and $\nu''_{k,j}$ are the molar stoichiometric coefficients of species k in reaction j[6].

For example, taking the classical methane reaction:

$$CH_4 + 2O_2 \rightarrow CO_2 + 2H_2O \tag{2.21}$$

and imposing $r = 1$ (because there is only one reaction), the Table 2.2 shows the molar stoichiometric coefficients:

$\mathcal{M}_1 = CH_4$	$\mathcal{M}_2 = O_2$	$\mathcal{M}_3 = CO_2$	$\mathcal{M}_4 = H_2O$
$\nu'_{1,1} = 1$	$\nu'_{2,1} = 2$	$\nu'_{3,1} = 0$	$\nu'_{1,4} = 0$
$\nu''_{1,1} = 0$	$\nu''_{2,1} = 0$	$\nu''_{3,1} = 1$	$\nu''_{1,4} = 2$

Table 2.2: Molar stoichiometric coefficients for classical methane reaction

Furthermore, mass conservation enforces:

$$\sum_{k=1}^{N} \nu'_{k,j} W_k = \sum_{k=1}^{N} \nu''_{k,j} \mathcal{M}_k \quad \text{or} \quad \sum_{k=1}^{N} \nu_{k,j} W_k = 0 \quad \text{where} \quad \nu_{k,j} = \nu''_{k,j} - \nu'_{k,j} \tag{2.22}$$

[6] In literature, these are referred to stoichiometric coefficients for reactant k or for product k in the reaction j

For species k, the reaction rate $\dot{\omega_k}$ is the sum of rates $\dot{\omega_{k,j}}$ produced by all M reactions:

$$\dot{\omega_k} = \sum_{j=1}^{M} \dot{\omega_{k,j}} = W_k \sum_{j=1}^{M} \nu_{k,j} Q_j \quad \text{with} \quad Q_j = \frac{\dot{\omega_{k,j}}}{W_k \nu_{k,j}} \tag{2.23}$$

where Q_j is the rate of progress of reaction j. Using the same approach of [32], the progress rate Q_j of reaction j is defined by:

$$Q_j = K_{f,j} \prod_{k=1}^{N} \left(\frac{\rho Y_k}{W_k} \right)^{\nu'_{k,j}} - K_{r,j} \prod_{k=1}^{N} \left(\frac{\rho Y_k}{W_k} \right)^{\nu''_{k,j}} \tag{2.24}$$

where $K_{f,j}$ and $K_{r,j}$ are the forward and reverse rates of reaction j. These rate constants constitute a central problem of combustion modelling. In this dissertation, they are modelled using the empirical Arrhenius law:

$$K_{f,j} = A_{f,j} T^{\beta_j} \exp\left(-\frac{E_j}{RT} \right) = A_{f,j} T^{\beta_j} \exp\left(-\frac{T_{a,j}}{T} \right) \tag{2.25}$$

where $A_{f,j}$ is the pre-exponential constant, β_j is the temperature exponent and $T_{a,j}$ is the activation temperature (or $E_j = \mathrm{R} T_{a,j}$, the activation energy).

These constants are usually included into the chemical scheme that must be available for the computation. Example of the chemical schemes are shown on chapter C.

The backwards rates $K_{r,f}$ are computed from the forward rates through the equilibrium constants:

$$K_{r,f} = \frac{K_{f,j}}{\left(\frac{p_a}{RT}\right)^{\sum_{k=1}^{N} \nu_{k,j}} exp\left(\frac{\Delta S_j^0}{R} - \frac{\Delta H_j^0}{RT} \right)} \tag{2.26}$$

where $p_a = 1$ bar. The Δ symbols refer to changes occurring when passing from reactants to products in the j^{th} reaction: ΔH_j^0 and ΔS_j^0 are respectively enthalpy and entropy changes for reaction j[7].

[7] These quantities are obtained from tabulations

2.1.3 Stoichiometry in premixed flames

For the sake of simplicity, the initial composition of the fuel can be expressed either in term of mass fraction or in term of the equivalence ratio. Moreover, in this work will be discussed only the so-called premixed flames. The term premixed flames refers to a premixed combustor, where fuel and oxidizer are mixed before entering into the combustion chamber. If $\nu_F^{'}F$ and $\nu_O^{'}O$ are the coefficient corresponding to fuel and oxidizer, when considering an overall unique reaction of the type:

$$\nu_F^{'}F + \nu_O^{'}O \rightarrow Products \tag{2.27}$$

the mass stoichiometric ratio s is defined by:

$$s = \frac{\nu_O^{'}W_O}{\nu_F^{'}W_F} \tag{2.28}$$

whereas the equivalence ratio ϕ of a given mixture is given by:

$$\phi = s\frac{Y_F}{Y_O} \tag{2.29}$$

This ratio is a central parameter for premixed gases: rich combustion (fuel in excess) is obtained for $\phi > 1$ while lean regimes (oxidizer in excess) are achieved when $\phi < 1$. In hydrocarbon-air flames, values of the fuel mass fraction are very small so that the premixed gas entering into the chamber contains mostly air.

2.1.4 Conservation of Mass and Species

The total mass conservation for reacting flow is unchanged compared to non reacting ones (Equation 2.1) because combustion does not generate mass.

Since there are several kind of species, one can define a mass conservation equation for each species k in the mixture:

$$\frac{\partial(\rho Y_k)}{\partial t} + \frac{\partial(\rho(u_i + V_{k,i})Y_k)}{\partial x_i} = \dot{\omega}_k \tag{2.30}$$

where $V_{k,i}$ is the i-component of the diffusion velocity V_k of species k and $\dot{\omega}_k$ is the reaction rate of species k (Equation 2.23). The term $V_{k,i}Y_k$ is defined by Equation 2.34

Numerical System for Mass Conservation

Instead of using the mass conservation for each species, having in mind the assumption that the sum of mass fractions must be unity, i.e. $\sum_{k=1}^{N} Y_k = 1$, one can define directly the total mass conservation. In fact, the mass conservation for each species (Equation 2.30) will add to the system other N equations while there are only N unknowns: then, the system is over determinate.

In order to use both Fick's Law and still maintain global mass conservation, for all simulations has been used the following approach: one can solve the global mass conservation equation (Equation 2.1) and subsequently solving only $N-1$ species equations. The last species mass fraction[8] is obtained solving $Y_N = 1 - \sum_{k=1}^{N-1} Y_k$, absorbing all inconsistencies introduced by Fick's Law, in the last equation.

However, this simplification leads to dangerous effects in some particular cases, as described in appendix B.

2.1.5 Conservation of Momentum

The equation of momentum is the same in reacting and non reacting flows (Equation 2.2). In order to take into account the mass fractions of all the species, the equation of the momentum is modified as:

$$\frac{\partial(\rho u_i)}{\partial t} + \frac{\partial(\rho u_i u_j)}{\partial x_j} = -\frac{\partial p}{\partial x_i} + \frac{\partial \tau_{ij}}{\partial x_j} + \rho \sum_{k=1}^{N} Y_k f_{k,j} \tag{2.31}$$

where $f_{k,j}$ is the body force acting on species k in j-direction.

Clearly, this equation does not add any explicit reaction terms even if the flow is modified by combustion. For example, the dynamic viscosity μ strongly changes because temperature varies and the density also changes through the flame front. These effects lead to a local variation of

[8] Using $H_2 - Air$ mixture, it is usually used N_2

Reynolds number, much more than in a non-reacting flow and at the end, combustion features are taken into account.

2.1.6 Conservation of Energy

The energy conservation requires the greatest attention because its behaviours are very important for reacting flows. Starting from the conservation equation in terms of total (chemical) energy e_t [11], this defined by:

$$\frac{\partial(\rho e_t)}{\partial t} + \frac{\partial(\rho u_i e_t)}{\partial x_i} = -\frac{\partial q_i}{\partial x_i} + \frac{\partial(\sigma_{ij} u_i)}{\partial x_j} + \dot{Q} + \rho \sum_{k=1}^{N} Y_k f_{k,i}(u_i + V_{k,i}) \tag{2.32}$$

where $e_t = e + K = e + (u_i u_i)/2$ with (absolute) internal energy e and kinetic energy K, $\dot{Q}$ is the heat source term (due for example to an electric spark, not related to the heat released by combustion) and the last term is the power produced by body forces f_k on species k.
The energy flux q_i is composed by two parts:

$$q_i = -\lambda \frac{\partial T}{\partial x_i} + \rho \sum_{k=1}^{N} h_k Y_k V_{k,i} \tag{2.33}$$

first including a heat diffusion term expressed by Fourier's Law (heat flow due to heat conduction) and second the diffusion of species with different enthalpies (enthalpy flux due to species diffusion). Assuming the Fick's law, the last term can be written as:

$$V_{k,i} Y_k = -D_k \frac{\partial Y_k}{\partial x_i} \tag{2.34}$$

where D_k is the diffusion coefficient of species k.
Using the standard relation between energy and enthalpy, one can arrange a conservative energy equation in terms of the absolute (chemical) enthalpy h[9]:

$$\frac{\partial(\rho h)}{\partial t} + \frac{\partial(\rho u_i h)}{\partial x_i} = \frac{Dp}{Dt} - \frac{\partial q_i}{\partial x_i} + \tau_{ij} \frac{\partial u_i}{\partial x_j} + \dot{Q} + \rho \sum_{k=1}^{N} Y_k f_{k,i} V_{k,i} \tag{2.35}$$

[9] Whole deduction can be found on [32]

The above expressions are not always easy to implement because it uses the expression for energy and enthalpy including the chemical terms in addition to energy or enthalpy; sometimes the energy equation in terms directly of sensible energy or enthalpy is preferred. From the definition of the sensible enthalpy h_s:

$$\frac{\partial(\rho h_s)}{\partial t} + \frac{\partial(\rho u_i h_s)}{\partial x_i} = \dot{\omega_T} + \frac{Dp}{Dt} - \frac{\partial q_i}{\partial x_i} + \tau_{ij}\frac{\partial u_i}{\partial x_j} + \dot{Q} + \rho\sum_{k=1}^{N} Y_k f_{k,i} V_{k,i} \tag{2.36}$$

where $\dot{\omega_T}$ is the heat release due to combustion:

$$\dot{\omega_T} = -\sum_{k=1}^{N} \Delta h^0_{f,k}\dot{\omega_k} \tag{2.37}$$

The separation of sensible enthalpy from the heat of formations gives this equation the advantage over Equation 2.35 that the heat of formation becomes the only source term.
Finally using the definition of the total (chemical) enthalpy $h_t = e_t + p/\rho$, one can deduce:

$$\frac{\partial(\rho h_t)}{\partial t} + \frac{\partial(\rho u_i h_t)}{\partial x_i} = \frac{\partial p}{\partial t} - \frac{\partial q_i}{\partial x_i} + \frac{\partial(\tau_{ij} u_i)}{\partial x_j} + \dot{Q} + \rho\sum_{k=1}^{N} Y_k f_{k,i}(u_i + V_{k,i}) \tag{2.38}$$

Equation 2.38 and Equation 2.32 play a fundamental role at high speed because the influence of kinetic energy cannot be neglected. Thus, these formulations must be implemented for supersonic simulations.

2.1.7 Species Equations

Finally, since combustion flows deal with chemical species in order to predict the local mass fraction of each species, a transport equation for species k is defined by:

$$\frac{\partial \rho Y_k}{\partial t} + \frac{\partial(\rho u_i Y_k)}{\partial x_i} = \frac{\partial}{\partial x_i}\left(\rho D_k \frac{\partial Y_k}{\partial x_i}\right) + \dot{\omega_k} \tag{2.39}$$

Once again, it is considered only the Fick's Law to approximate diffusion velocity. This is a strong approximation because relates the diffusion flux to the concentration under a steady-

state condition. In fact, it postulates that the flux goes from regions of high concentration to regions of low concentration, with a magnitude that is proportional to the concentration gradient. However, the intrinsic diffusion problem nested into the combustion itself does not have to be solved sparing computational time.

2.2 Turbulent Combustion

Due to the high turbulent nature of detonation, turbulence has to be taken into account to solve the Navier-Stokes equations. In fact, in general, after few microseconds the laminar regime is soon replaced by a regime where turbulence and combustion interact. As easy to understand, studying and modelling turbulent combustion process is an important problem to develop and improve practical system, i.e to increase efficiency and reduce fuel consumption. Actually, their complexity comes from three main points:

- combustion, even more with turbulent features, is an indistinctly complex process involving a large range of chemical time and length scales;
- turbulence itself is probably the most complex phenomenon in non-reacting fluid mechanics;
- turbulent combustion results from the two-way interaction of chemistry and combustion. When a flame interacts with a turbulent flow, turbulence is modified by combustion because of the strong flow accelerations through the flame front induced by heat release, and because of the large changes in kinematic viscosity associated with temperature changes. On the other hand, turbulence alters the flame structure, which may enhance the chemical reaction but also, in extreme cases, completely inhibit it, leading to flame quenching.

Avoiding an elementary introduction about turbulence, the three main numerical approaches used in turbulence combustion modelling are briefly presented:

- **DNS**[10]**:** the N-S equations are solved without any turbulence model [33], that means all characteristic length and time scales are resolved; it requires a very fine mesh in order to resolve the scales in the Kolmogoroff range, which depends on the Reynolds number. Due to the use of the very fine mesh and very small time step, the computational cost is huge. Typically, this approach is limited to academic situations;

- **LES**[11]**:** the N-S equations are filtered by a low-pass filter [29]. The larger scales are explicitly computed whereas the effects of smaller ones are modelled. From the computational point of view, this method lies in between a DNS and RANS and, in the most cases, requires a 3D domain. When the computational domain is large and the flow has high turbulence level, LES is not feasible;

- **RANS**[12]**:** these describe mean flow fields, decomposing a turbulent quantity $\phi(x, y, z, t)$ in its time-average quantity $\overline{\phi(x, y, z)}$ and its fluctuating quantity $\phi'(x, y, z, t)$, called Reynolds decomposition [33]. In conclusion, these are substituted into N-S equations.

- **URANS**[13]**:** The RANS method is limited to the use of stationary flow [34]. Then, defining the time-average quantity $\bar{\phi}$ as:

$$\bar{\phi} = \frac{1}{\Delta t} \int_{t}^{t+\Delta t} \phi dt \tag{2.40}$$

  the turbulent fluctuations may also originate from the average value $\bar{\phi}$ [33]. In this work, URANS has been chosen to model turbulence since gives good results (for this analysis) still keeping an acceptable computational cost.

Without going into details, when turbulence is modelled by the use of URANS method, the Reynolds stress appears in the N-S equations in addition to the viscous stresses, that is an apparent stress tensor introduced by the model itself. Typical chooses for this kind of application are the so-called "$k-\epsilon$" and/or "$k-\omega$", i.e. common two-equation turbulence models in terms

[10] Direct Numerical Simulation.
[11] Large Eddy Simulation.
[12] Reynolds Average Navier-Stokes
[13] Unsteady Reynolds Average Navier-Stokes

of turbulent kinetic, turbulent dissipation or specific dissipation. A more comprehensive study can be found in literature [33, 29].

2.3 Numerical Implementation of the Solver

The core of the solver is based on the existing code proposed by Ettner [35], but with significant changes. A specific combustion model is implemented for working with both schemes of reaction, reduced and detailed. Moreover, two different algorithms are implemented for solving the different natures of the combustion. Chemical model and supersonic effects are taken into account for the implementation.

In this section, after a briefly introduction of OpenFoam, the old solver will be described highlighting of it the main aspects. Afterwards, a deeper description of the new solver will be provided. Particular focus on highlighting the main differences between the previous solver and the new one will be considered as well.

2.3.1 OpenFoam

The open-source computational fluid dynamic (CFD) software OpenFoam was used to perform the simulations using its open-source packages [36]. The modular software architecture in the oriented-object programming language C++ made possible to build them on existing solvers and models. Most of the existing codes can be processed in parallel, in this work great emphasis has been placed on making the implementation fully parallelizable. These aspects will not be described in this work but a good explanation can be found in the OpenFoam user guide [37]. Post-processing can be done with paraView and preprocessing, like meshing etc., can be performed using OpenFoam utilities, as well.

One reason of this software choice is that, contrary to many proprietary detonation codes, OpenFoam has the built-in capability of dealing with unstructured grids a clear advantage in view of the intended future application to sophisticated geometries. Another reason for the usage of OpenFOAM was that the code is free and open source and thus also the model developed can be made available to the scientific community at no cost. Although some openFoam solvers have been used for years to simulate high-speed reactive flows, the approach adopted here has not been largely employed to simulated detonation process. Marcantoni et al. [38]

performed planar detonations using Kurganov central schemes and detailed chemistry, through an adaptation of the second order central-upwind numerical scheme of Kurganov, previously introduced for non reactive flow simulation (for example, *rhoCentralFoam*). Ettner et. al. [39] has performed simulations using the same pressure/density-based approach used here, but the chemical kinetic is modelled extracting interpolated values from Cantera in terms of pressure, temperature and mixture fraction of hydrogen atoms, that means without resolving the microstructures of the flow. Furthermore, the detonation is just modelled by adding artificial sources.

2.3.2 ddtFoam

This solver was developed by Dr. Ettner in his PhD Thesis [35] and is publicly available on the website [40]. The purpose of this code is simulating the deflagration-to-detonation transition (DDT) without resolving all microscopic details of the flow, being able to use only H_2-Air mixture in 2D notched shock tubes. In fact, it is able to simulate both deflagrations and detonations effects with emphasis on their transition.

Basically, it is splitted in two main solvers based on the solution of different algorithms: the pressure-based, used to start computations for the deflagrative part, and the density-based used for the detonative part. As already said, in order to provide the rates of reaction, the solver contains a tabulated data based on the O'Conaire's scheme [25]. Hence, the solver does not solve at each step a species equation but imports tabulated data from Cantera: this allows to simulate the detonation phenomenon with less computational cost.

Omitting the detailed description of the whole solver, which can be found in his thesis [35], the two algorithms will be briefly described in the following in order to understand the main features.

Pressure-based solver "pddtFoam"

When the Mach number is below 0.3, the compressibility effects should be neglected and the continuity equation (Equation 2.1) is not suitable anymore to compute the density as a depen-

dent variable wherein the pressure is evaluated from it via the equation of state (Equation 2.8). To handle these issues, methods based on solving a new transport equation for pressure is formulated. Here the pressure-velocity coupling solution methods known as PISO (i.e. Pressure Implicit with Splitting of Operators) is used [41]. An appropriate description for the OpenFoam environment has been given by Jasak [42]. Rather than solve all of the coupled equations in a coupled or iterative sequential fashion, PISO splits the operators into an implicit predictor and multiple explicit corrector steps [43].

Therefore, this algorithm must be taken into account only for the deflagration since the combustion wave propagates at subsonic speed. By introducing a reaction progress variable c for each cell, with $c = 0$ representing unburnt mixture and c = 1 a burnt mixture, the calculation of the mass species can be replaced with a simple transport equation in term of c, instead of solving the species equation:

$$\frac{\partial(\bar{\rho}\tilde{c})}{\partial t} + \frac{\partial(\bar{\rho}\tilde{c}\tilde{u}_j)}{\partial x_j} = \frac{\partial}{\partial x_j}\left(\bar{\rho} D_{eff} \frac{\partial \tilde{c}}{\partial x_j}\right) + \overline{\omega_{c,def}} \tag{2.41}$$

where the overbar denotes Reynolds-averaging and the tilde denotes Favre-averaging[14]. Knowing the progress variable c, the mixture composition can be found using a table calculated in advanced with Cantera and stored into the solver. The source term $\omega_{c,def}$ is modelled by using the RANS version of the Weller combustion model with an additional quenching factor G [39]. Hence, the turbulent flame speed is calculated by:

$$s_T = \xi s_L \tag{2.42}$$

having imposed s_T and s_L respectively the turbulent and laminar flame speed which can be found by a polynomial equations [39]. The deflagrative source term can then be solved:

$$\overline{\omega_{c,def}} = \bar{\rho}_u s_T |\nabla \tilde{c}| G \tag{2.43}$$

[14]These formal definitions can be found on [33]

with ξ the folding factor depending on the turbulent flame area and ρ_u [44].

However, the dependence of flame speed ($s_{L,0}$) on molar hydrogen fraction x_{H2} can be approximated as a polynomial. This molar fraction x_{H2} is calculated using another transport equation of mixture fraction f_H (fEqn), that is, the amount of hydrogen that would be present if the cell was completely unburnt:

$$\frac{\partial(\bar{\rho}\tilde{f}_h)}{\partial t} + \frac{\partial(\bar{\rho}\tilde{f}_h\tilde{u_j})}{\partial x_j} = \frac{\partial}{\partial x_j}\left(\bar{\rho}D_{eff}\frac{\partial \tilde{f}_h}{\partial x_j}\right) \tag{2.44}$$

Finally, the dependence of laminar flame speed on pressure and temperature can be approximated as:

$$s_L = s_{L,0}\left(\frac{T}{T_0}\right)^{\alpha}\left(\frac{p}{p_0}\right)^{\beta} \tag{2.45}$$

where α = 1.75 and β = -0.2.

In conclusion, without using both an explicit combustion model and without solving whole dynamic of the flow, the deflagration part is simulated taking into account different precautions. Experimental values for the laminar burning speed of hydrogen-air flames at standard conditions can be found on [45].

Density-based solver "ddtFoam"

The detonation process, at which the combustion wave travels at supersonic speeds, can be modelled by solving the Arrhenius equations of the reaction scheme, but it requires a very small spatial discretization due to the stiffness of those equations. Thus, the Ettner's idea was to model this phenomenon reducing the extensive computational effort, that is not feasible without supercomputers. Another principle of modelling detonation relies on the use of the auto-ignition delay time. This is based on the fact that fuel auto-ignites due to a high pressure and temperature: when pressure and temperature are high enough, autoignition delay time is very small and detonation of fresh mixture is initiated. At this scope, the dimensionless variable τ:

$$\tau = \frac{t}{t_{ignition}} \tag{2.46}$$

was introduced, indicating the elapsed time relative to the auto-ignition time. As long as τ has not reached unity, the flow is unaffected by ignition. As usual, a transport equation for τ was introduced:

$$\frac{\partial(\bar{\rho}\tau)}{\partial t} + \frac{\partial(\bar{\rho}\tau\tilde{u}_j)}{\partial x_j} = \frac{\partial}{\partial x_j}\left(\bar{\rho}D\frac{\partial \tau}{\partial x_j}\right) + \overline{\omega_\tau} \tag{2.47}$$

where the last term is the detonation source term. As for the pressure-based part, in order to reduce the computational cost, this auto-ignition time is stored in advance into the solver and is calculated with Cantera. Clearly, both temperature and pressure have a notable impact on $t_{ignition}$: then, a table containing pressure, temperature and mixture composition values are stored into the solver, as well. In conclusion, Equation 2.41 can be used to incorporate the detonation process leading to:

$$\frac{\partial(\bar{\rho}\tilde{c})}{\partial t} + \frac{\partial(\bar{\rho}\tilde{c}\tilde{u}_j)}{\partial x_j} = \frac{\partial}{\partial x_j}\left(\bar{\rho}D_{eff}\frac{\partial \tilde{c}}{\partial x_j}\right) + \overline{\omega_{c,def}} + \overline{\omega_{c,ign}} \tag{2.48}$$

where the last term is calculated with the autoignition delay time.

2.4 zndFoam

Since the previous solver is able to work only with H_2-Air mixtures, i.e. without using different schemes of reaction, and since it is not supposed for working properly to simulate the flow within detonation engines, a new version with significant updates is presented in this dissertation. Basically, the idea of splitting the simulation in two different solvers, using then two different algorithm, is unchanged. The main difference is the ability of the solver of simulating both macro and micro effects of the flow, using any kind of mixture and reactions scheme. So, the equations mentioned above (chapter 2) will be implemented with some approximations. The interaction between chemistry and turbulence, is modelled according to the partially stirred reactor (PaSR) concept. Moreover, the exponential dependence of the chemical kinetics from the temperature leads to solve the species conservative equations. Since the density-based part must be able to handle supersonic effects, an innovative numerical scheme of the Riemann solver class was implemented in order to well predict both position and value of the shock wave.
A detailed description of the solver zndFoam, thanks to the famous *Y. B. Zel'dovich, John von Neumann, and Werner Dring* theory is presented in this section with details to the numerical part as well.

2.4.1 Finite volume method

The discretization of the governing equations is based upon the finite volume method. The finite volume discretization scheme is formulated by taking advantage of the data structure provided by OpenFoam. A central problem of this method is the discretization of the convective term, which must appropriate based on the different applications.
The finite volume methods (FVM) methods transforms the integral form of the conservation equations into discrete algebraic equations over finite volumes. The computational domain is then split into small interconnected volumes, not overlapping, and the solver calculates for each volume the cell centred value by integrating the conservative equations. Some of the terms in these equations are turned into face fluxes and evaluated at the finite volume faces. Because

the flux entering a given volume is identical to that leaving the adjacent volume, the FVM is strictly conservative. Considering the generic conservation equation for a quantity ϕ and assuming that the velocity field and all fluid properties are know, the finite volume methods on its integral form can be written as:

$$\int_S \rho\phi \; \vec{v} \cdot \vec{n} \, \mathrm{d}S = \int_S \Gamma \; \nabla\phi \cdot \vec{n} \, \mathrm{d}S + \int_\Omega q_\phi \, \mathrm{d}\Omega \tag{2.49}$$

The usual approach is to define control volumes (CV) by a suitable grid and assign the computation node to the control volume center. The advantage of using it, is that the nodal value represents the mean over the CV to second order accuracy. The integral conservation equation applied to each CV leads to a global conservation equation, since surface integrals over inner CV faces cancel out. To obtain an algebraic equation for a particular CV of the form Equation 2.50, the surface and volume integrals need be approximated using quadrature formulae:

$$A\vec{\phi} = \vec{b} \tag{2.50}$$

where $\vec{\phi}$ contains all the conservative variables, i.e. $\rho, \rho\vec{u}, \rho h_t, \rho Y_k$.

Surface Integrals The net flux through the CV boundary is the sum of integrals over the four (in 2D) CV faces:

$$\int_S f \, \mathrm{d}S = \sum_k \int_{S_k} f \, \mathrm{d}S \tag{2.51}$$

where f is the component of the convective or diffusive flux vector in the direction normal to CV face. To calculate the surface integral exactly, one would need to know the integrand f everywhere on the surface S_e. This information is not available, as only CV center values of ϕ are calculated so an approximation must be introduced. Since the value of f is not available at the cell face center e, in this work, the trapezoid rule was used to get this value, which leads to:

$$F_e = \int_{S_e} f_e \, \mathrm{d}S \approx \frac{S_e}{6} \left(f_{ne} + f_{se}\right) \tag{2.52}$$

where the value of f are calculated by using the two nodal values, ne and se. Of course, the accuracy of the approximation depends on the order of shape functions.

Volume Integrals On other hand, some transport equations require integration over the volume of a CV [46]. Basically, the simplest second-order accurate approximation is to replace the volume integral by the product of the mean value of the integrand and the CV volume and approximate the former as the value at the CV centre:

$$Q_P = \int_\Omega q \, \mathrm{d}\Omega \approx q_P \, \Delta\Omega \tag{2.53}$$

where q_P stands for the value of q at the CV centre. This quantity is easily calculated since all variables are available at node P, thus no interpolation is necessary. But the above approximation contains a second-order error; for an approximation of higher order the values of q must be available at more locations, i.e. obtaining it by interpolation nodal values. Thus, the approximations to the integral require, in some cases, the values of variables at locations other than computational nodes. The integrand has to be expressed in terms of the nodal values by interpolation. In this work, linear interpolation was used (CDS).

The value at CV-face centre is linear interpolated between the two nearest nodes. At location e on a grid:

$$\phi_e = \phi_E \lambda_e + \phi_P (1 - \lambda_e) \tag{2.54}$$

where the linear interpolation factor λ_e is defined as:

$$\lambda_e = \frac{x_e - x_P}{x_E - x_P} \tag{2.55}$$

which is a second-order accurate that may produce oscillatory solutions. This is the simplest scheme of second-order accuracy and offers a good compromise among accuracy, simplicity and efficiency.

Temporal Discretization Since Navier-Stokes equations belong to the class of hyperbolic equations, a good choice of temporal discretization is the so-called Explicit Time Advance Scheme. Consider the simple Navier-Stokes equations of the form:

$$\frac{\partial \rho u_i}{\partial t} = H_i - \frac{\delta p}{\delta x_i} \tag{2.56}$$

where δ/δ_x represents a discretized spatial derivative and H_i is shorthand notation for the advective and viscous terms, the explicit Euler method for time advancement is defined by:

$$(\rho u_i)^{n+1} - (\rho u_i)^n = \Delta t \left(H_i^n - \frac{\delta p^n}{\delta x_i} \right) \tag{2.57}$$

To apply this method, the velocity at time step n is used to compute H_i and, if the pressure is availbale may also be computed. This the standard temporal discretization for solving supersonic flows. Of course, the stability of this method and the accuracy depend on the time step imposed.

For the incompressible schemes, it is usually performed a PISO scheme because of the incompressibility of the flow. The temporal discretization can be treated as implicit, requiring the knowledge of u_i^{n+1} [47]. Performing a simple Taylor expansion around time t can be noted that it comes out an anti-diffusion term with compression effects on profiles, very similar to the Downwind scheme in advection. This anti-diffusion term scales with the time step. A related issue to the anti-diffusion behavior is numerical instabilities, which increases with increasing temporal derivative placing a very strong restriction on the time step. It should be kept in mind for interpreting the results.

Riemann Solver For compressible flows and high Mach number, there is no coupling between continuity and momentum equation, then the explicit method is required to get accurate results. Moreover, the properties may be transported by waves independently of the bulk flow and flux interpolations can occur in any direction are required. Therefore, for the density-based part, the convective terms are evaluated using HLLC Riemann solver, introduced by Toro [48, 49]. The central idea is to assume a wave configuration for the solution that consists of two

waves separating three constant states. Assuming it, the wave speeds are given by some algorithm, application of the integral form of the conservation laws gives a closed-form, approximate expression for the flux. The mathematical description will be provided on the section related to the implementation of density-based solver.

At the end, to guarantee that every cell is only influenced by his neighbouring cell, the Courant number is introduced, which basically shows how far information can be transported throughout the cell in one time step. In order for the scheme to be stable, the CFL number should be limited to a maximum CFL number:

$$CFL = \frac{(|\vec{u}| + a)\ \delta t}{\delta x} < CFL_{max} \tag{2.58}$$

where $\vec{u}$ is the flowspeed, a the speed of sound, δx the spatial discretization and δt the time step. The CFL number imposed for each simulation is 0,2.

2.4.2 pzndFoam

As the previous pressure-based part, used for the deflagration phenomenon, pressure implicit with splitting of operator (PISO) is used to handle incompressible effects of the flow. However, in order to taking into account the combustion process, different energy (respect to the previous solver) and species equations were defined, extended to cover high temperature flows. Avoiding the description of the classes needed by OpenFoam for running the simulation itself, only the main equations of the solver will be described.

Global mass conservation - rhoEqn.H The global mass conservation is defined by:

```
solve(fvm::ddt(rho)+fvm::div(phi));
```

which is the numerical formulation of Equation 2.1, where *rho* indicates the density and *phi* is the mass flow through the cell faces, i.e. $\rho \cdot \vec{U} \cdot \vec{A}$ where U is the three-dimensional velocity

and A is the area of the face. As already said, the choose of using a global mass conservation, instead of a mass conservation for each species, may be lead to dangerous effects: assuming the approximation described on chapter B, these effects can be ignored.

Momentum conservation - UEqn.H The momentum equation for reactive flow is defined by:

```
FvVectorMatrix UEqn
(
    fvm::ddt(rho,U) + fvm::div(phi,U)
     + turbulence->divDevRhoReff(U)
     ==
     rho*g
);
```

which is the numerical formulation of Equation 2.31. The first assumption is related to the body forces $\rho \sum_{k=1}^{N} Y_k f_{k,j}$. In fact, assuming that $f_{k,j}$ is the gravitation force g, the previous term yields to:

$$\rho \sum_{k=1}^{N} Y_k f_{k,j} = -\rho g \sum_{k=1}^{N} Y_k \tag{2.59}$$

where g acts only in y-direction and ρ is assumed as constant due to the incompressibility of the flow. Using the definition of mass fraction Y_k, since the sum of the mass fraction in the mixture must be unity, the Equation 2.59 leads to:

$$\rho \sum_{k=1}^{N} Y_k f_{k,j} = -\rho g \sum_{k=1}^{N} Y_k = -\rho g \tag{2.60}$$

compatibly in what is described in the last line. Furthermore, the term *divDevRhoReff(U)* is related to the divergence of the stress tensor $\vec{\vec{\tau}}$ where, using the definition, is given by:

$$\frac{\partial \tau_{ij}}{\partial x_i} = \frac{1}{3}\mu \frac{\partial}{\partial x_i}\left(\frac{\partial u_k}{\partial x_k}\right) + \mu \frac{\partial^2 u_i}{\partial x_i^2} \tag{2.61}$$

Defining the operator *dev2* as:

$$dev2(A) = A - 2/3Tr(A)\vec{\vec{I}} \tag{2.62}$$

where *Tr* indicates the trace of the matrix A and I is the identity matrix, the formulation of Equation 2.61 is given by:

```
divDevRhoReff(U)
(
    -fvm::laplacian(muEff(),U)
    -fvm::div(muEff()*dev2(fvc::grad(U).().T()))
);
```

where, in matrix form, is given by:

$$-\nabla^2(muEffU) - \nabla \cdot \left[muEff \left((\nabla U)^T - \frac{2}{3} Tr((\nabla U)^T \vec{\vec{I}} \right) \right] \tag{2.63}$$

indicating with *muEff* the effective viscosity defined above, related to the turbulence model and T indicates the transpose of the matrix[15].

Energy conservation - hsEqn.H The energy equation defined in term of sensible enthalpy is given by:

```
fvScalarMatrix hsEqn
        (
            fvm::ddt(rho, hs)
            + mvConvection->fvmDiv(phi, hs)
            - fvm::laplacian(turbulence->alphaEff(), hs)
            ==
            dpdt
          + fvc::div(muEff*(fvc::grad(U))&U)
```

[15] Property: $\nabla \cdot A = Tr(\nabla A) = Tr(\nabla A)^T$

```
        + fvc::div(muEff*dev2(Foam::T(fvc::grad(U)))&U)
        - fvc::ddt(rho, K)
        - fvc::div(phi, K)
        + combustion->Sh()
    );
```

which is the numerical formulation of Equation 2.36 without using both the heat source term $\dot{Q}$ and the body forces. Moreover, some components are in terms of different variables with regards to the classical ones, but again this kind of energy equations can be directly obtained from the energy equation in terms of (absolute) enthalpy h:

$$\frac{\partial(\rho h)}{\partial t} + \frac{\partial(\rho u_i h)}{\partial x_i} = \frac{Dp}{Dt} - \frac{\partial q_i}{\partial x_i} + \tau_{ij}\frac{\partial u_i}{\partial x_j} + \dot{Q} + \rho\sum_{k=1}^{N} Y_k f_{k,i} V_{k,i} \tag{2.64}$$

Splitting the (absolute) enthalpy into sensible and chemical enthalpies, the Equation 2.64 is given by:

$$\frac{\partial(\rho h_s)}{\partial t} + \frac{\partial(\rho u_i h_s)}{\partial x_i} + \frac{\partial(\rho h_c)}{\partial t} + \frac{\partial(\rho u_i h_c)}{\partial x_i} = \frac{Dp}{Dt} - \frac{\partial q_i}{\partial x_i} + \tau_{ij}\frac{\partial u_i}{\partial x_j} \tag{2.65}$$

Taking into account only the chemical enthalpy, the previous equations can be written as:

$$\frac{\partial(\rho h_c)}{\partial t} + \frac{\partial(\rho u_i h_c)}{\partial x_i} = \sum_{k=1}^{N} h_{c,k}\left(\frac{\partial(\rho Y_k)}{\partial t} + \frac{\partial(\rho u_i Y_k)}{\partial x_i}\right) \tag{2.66}$$

where the expression into the brackets can be referred to the species equation (Equation 2.39). Then substituting:

$$\frac{\partial(\rho h_s)}{\partial t} + \frac{\partial(\rho u_i h_s)}{\partial x_i} + \sum_{k=1}^{N} h_{c,k}\dot{\omega}_k + \sum_{k=1}^{N} h_{c,k}\rho D\frac{\partial^2 Y_k}{\partial x_i^2} = \frac{Dp}{Dt} - \frac{\partial q_i}{\partial x_i} + \tau_{ij}\frac{\partial u_i}{\partial x_j} \tag{2.67}$$

The second term of RHS is referred to the energy flux (Equation 2.33). The first part is still referred to the Fourier's Law using, in the script, $alphaEff$ and hs instead of λ and T. This is because the diffusive flux term has to be included into the solution matrix. For this reason, it is necessary to express Fourier's Law in terms of sensible enthalpy. Starting with an expression

of the enthalpy gradient for a multicomponent gas mixture:

$$\nabla h = C_p \nabla T + \sum_{k=1}^{N} h_k \nabla Y_k \tag{2.68}$$

one can, by express the specific enthalpy with the sum of sensible and chemical enthalpy as well, modify Fourier's Law to:

$$\begin{aligned} \lambda \nabla T = \frac{\lambda}{C_p}\nabla h - \sum_{k=1}^{N} \frac{\lambda}{C_p} h_k \nabla Y_k = \frac{\lambda}{C_p}\nabla h_s + \sum_{k=1}^{N} \frac{\lambda}{C_p} h_{c,k} \nabla Y_k - \\ - \sum_{k=1}^{N} \frac{\lambda}{C_p} h_{c,k} \nabla Y_k - \sum_{k=1}^{N} \frac{\lambda}{C_p} h_{s,k} \nabla Y_k = \\ \frac{\lambda}{C_p}\nabla h_s - \sum_{k=1}^{N} \frac{\lambda}{C_p} h_{s,k} \nabla Y_k = \rho\alpha \nabla h_s - \rho\alpha \sum_{k=1}^{N} h_{s,k} \nabla Y_k \end{aligned} \tag{2.69}$$

Splitting the second part of the energy flux into sensible and chemical enthalpy, the main equation becomes:

$$q_i = \rho\alpha \nabla h_s - \rho\alpha \sum_{k=1}^{N} h_{s,k} \nabla Y_k + \rho \sum_{k=1}^{N} h_{s,k} D_k \nabla Y_k - \rho \sum_{k=1}^{N} h_{c,k} D_k \nabla Y_k \tag{2.70}$$

where the previous equation can be written as:

$$q_i = \rho\alpha \nabla h_s - \rho\alpha \sum_{k=1}^{N} h_{s,k} \left(1 - \frac{D_k}{\alpha}\right) \nabla Y_k - \rho \sum_{k=1}^{N} h_{c,k} D_k \nabla Y_k \tag{2.71}$$

Using the definition of Lewis number and assuming $Le_k = 1$,

$$q_i = \rho\alpha \nabla h_s - \rho \sum_{k=1}^{N} h_{c,k} D_k \nabla Y_k \tag{2.72}$$

Substituting Equation 2.72 into Equation 2.67, the final equation is given by:

$$\frac{\partial(\rho h_s)}{\partial t} + \frac{\partial(\rho u_i h_s)}{\partial x_i} + \sum_{k=1}^{N} h_{c,k} \dot{\omega}_k = \frac{Dp}{Dt} + \rho\alpha \frac{\partial^2 h_s}{\partial^2 x_i} + \tau_{ij} \frac{\partial u_i}{\partial x_j} \tag{2.73}$$

Using the definition of the total energy and defining the kinetic energy $K = (u_i u_i/2)$, the energy equation used by the pressure-based solver is given by:

$$\frac{\partial(\rho h_s)}{\partial t} + \frac{\partial(\rho K)}{\partial t} + \frac{\partial(\rho u_i h_s)}{\partial x_i} + \frac{\partial(\rho u_i K)}{\partial x_i} + \sum_{k=1}^{N} h_{c,k}\dot{\omega}_k = \frac{\partial p}{\partial t} + \rho\alpha\frac{\partial^2 h_s}{\partial^2 x_i} + \frac{\partial(\tau_{ij}u_i)}{\partial x_j} \tag{2.74}$$

In the end, the last term of the LHS is handled by the combustion term, i.e. calculated by the combustion model implemented.

The values of C_p, H_k, etc. are calculated in terms of the temperature and constant coefficients provied by the thermophysical table (chapter C). These are given by using the so called *Janaf Law* [50], such that:

$$\begin{aligned} C_{p,k} &= R\left((((a_{4,k}T + a_{3,k})\,T + a_{2,k})\,T + a_{1,k})\,T + a_{0,k}\right) \\ \frac{H_k}{RT_k} &= a_{1,k} + \frac{a_{2,k}}{2}\,T_k + \frac{a_{3,k}}{3}\,T_k^2 + \frac{a_{4,k}}{4}\,T_k^3 + \frac{a_{6,k}}{T_k} \\ \frac{S_k}{R} &= a_{1,k}\log T_k + a_{2,k}\,T_k + \frac{a_{3,k}}{2}\,T_k^2 + \frac{a_{4,k}}{4}\,T_k^2 + \frac{a_{4,k}}{3}\,T_k^3 + +\frac{a_{5,k}}{4}\,T_k^4 + a_{7,k} \end{aligned} \tag{2.75}$$

The functions are valid between a lower and upper limit in temperature, T_{low} and T_{high} respectively. Two sets of coefficients are specified, the first set for temperatures above a common temperature T_{common} (and below T_{high}), the second for temperatures below T_{common} (and above T_{low}). Having C_p, one can calculate the sensible neither enthalpy and energy, starting from Equation 2.11.

Species equation - YEqn.H The species equation, that must be solved for each species involved into the mixture, is defined by:

```
combustion->correct();
dQ = combustion->dQ();
label inertIndex = -1;
volScalarField Yt(0.0*Y[0]);
forAll(Y, i)
{
```

```
        if (Y[i].name() != inertSpecie)
        {
            volScalarField& Yi = Y[i];
            fvScalarMatrix YiEqn
            (
                fvm::ddt(rho, Yi)
              + mvConvection->fvmDiv(phi, Yi)
              - fvm::laplacian(turbulence->muEff(), Yi)
             ==
                combustion->R(Yi)
            );
            YiEqn.relax();
            YiEqn.solve(mesh.solver("Yi"));
            Yi.max(0.0);
            Yt += Yi;
        }
        else
        {
            inertIndex = i;
        }
    }
    Y[inertIndex] = scalar(1) - Yt;
    Y[inertIndex].max(0.0);
```

which is the numerical formulation of Equation 2.39, having previously defined the reactions scheme. One can see, the equation is based on the assumption that the ratio of momentum diffusivity and mass diffusivity Schmidt number, is unity ($Sc = 1$). Thus, this dimensionless number yields:

$$Sc = \frac{\mu}{\rho D} = 1 \rightarrow \rho D = \mu \tag{2.76}$$

Therefore, the mass diffusivity D has been imposed to be the same for all species and the species diffusion process is entirely controlled by the mixture viscosity, which is calculated from Sutherland's law, defined by:

$$\mu = \frac{A_s\sqrt{T}}{1 + T_s/T} \tag{2.77}$$

where A_s is the Sutherland coefficient and T_s is the Sutherland temperature, imported from the thermodynamic property table (chapter C). Moreover, since $Le = 1$:

$$Le = \frac{\lambda}{DC_p\rho} = 1 \rightarrow \frac{\lambda}{C_p} = \rho D \tag{2.78}$$

where, as in the previous case, $muEff = mu_T + mu$ requested by the turbulence model.

The term *combustion->R(Yi)* is connected to $\dot{\omega}_k$ which calculates the reaction rate of the i-species[16]. This is calculated by using suitable stoichiometric coefficients, species compositions and Arrhenius reaction rates as described in chapter 2.

However, this equation considers only Fick's Law as diffusion velocity, i.e considers only diffusion flux due to gradient concentration. It neglects the flux due to a pressure gradient and the thermal diffusion flux due to a temperature gradient. Moreover, it does not explicit any flux to external forces, for example in charged mixtures. But previous works on the same topic available in the literature, the species equation in this form has shown good behavior with reduced computational cost.

PISO Algorithm

The previous mentioned PISO algorithm, in which pressure and velocity are coupled, was considered. This algorithm was proposed by Issa in 1986 [41], pushing forward the SIMPLE concept on the solution of Navier-Stokes equations. In general, it gives more stable results and takes less CPU time than SIMPLE algorithm and it is suitable for solving the pressure-velocity linked equation with large time step.

Considering incompressible flows, the density variation are not linked to the pressure. The mass conservation (Equation 2.79) is only a constraint on the velocity field and the equation

[16] Or k, using the same notation

(combined with the momentum) can be used to derive an equation for the pressure[17].

In order to understand how this algorithm works, the incompressible Navier-Stokes equations will be handled for sake of simplicity in order to explain it[18]:

$$\begin{cases} \nabla \cdot \mathbf{u} = 0 \\ \frac{\partial \mathbf{u}}{\partial t} + \nabla \cdot (\mathbf{uu}) - \nabla \cdot (\nu \nabla \mathbf{u}) = -\nabla p \end{cases} \tag{2.79}$$

The non-linearity in the convection term ($\nabla \cdot (\mathbf{uu})$) is handled using an iterative solution technique, that is:

$$\nabla \cdot (\mathbf{uu}) \approx \nabla \cdot (\mathbf{u}^o \mathbf{u}^n) \tag{2.80}$$

where $\mathbf{u}^o$ is the currently available solution and $\mathbf{u}^n$ is the new solution. The algorithm cycles until $\mathbf{u}^o = \mathbf{u}^n$. Starting from the following semi-discrete form of the momentum equation:

$$a^u_{\mathbf{P}} u_P + \sum_N a^u_{\mathbf{N}} u_N = r_{\mathbf{P}} - \nabla p \tag{2.81}$$

with the operator H($\mathbf{u}$):

$$H(u) = r_{\mathbf{P}} - \sum_N a^u_{\mathbf{N}} u_N \tag{2.82}$$

where $r_{\mathbf{P}} = r_{\mathbf{0}} + \frac{U^{n-1}}{\Delta t}$ and $a_{\mathbf{P}}$ are the center coefficients of the momentum equations. The discrete operator H($\mathbf{u}$) has two contributions: the first one related to

By using Equation 2.81, continuity and state equations, the momentum equation becomes:

$$\begin{cases} a^u_{\mathbf{P}} u_P = H(u) - \nabla p \\ \rightarrow u_p = (a^u_{\mathbf{P}})^{-1} (H(u) - \nabla p) \end{cases} \tag{2.83}$$

Substituting the last one into the incompressible continuity equation (Equation 2.79), the elliptic pressure equation for incompressible flows is given by:

$$\nabla \cdot [(a^u_{\mathbf{P}})^{-1} \nabla p] = \nabla \cdot [(a^u_{\mathbf{P}})^{-1} H(u)] \tag{2.84}$$

[17] For compressible flows, the mass conservation is a transport equation for density. With an additional energy equation, p can be specified from a thermodynamic relation (ideal gas law)

[18] Bold format indicates vectorial variable

The previous algorithm can be summarized as algorithm 1. A complete description of this algorithm can be found on [46].

Input: Choice of u^o and p
Output: p
while *runTime.run()* **do**
  Set boundary conditions;
  Solve the discretized momentum equation;
  for $corr \leftarrow 1$ **to** $nCorr$ **do**
    Compute the mass fluxes;
    Solve the pressure equation;
    Correct the mass fluxes;
    Correct the velocities on the basis of the new pressure field;
  end
  Increase the time step;
end

Algorithm 1: PISO Algorithm

On the negative side, the derivation of PISO is based on the assumption that the momentum discretization may be safely frozen through a series of pressure correctors, which is true only at small time-steps. Experience also shows that the PISO algorithm is more sensitive to mesh quality than the SIMPLE algorithm [41].

2.4.3 zndFoam

The density-based solver has been developed to solve the governing equations, described above, using the finite volume method [51]. As seen before, a central problem of finite volume method is the discretization of the flux over each face (Figure 2.2). Due to the compressible effects

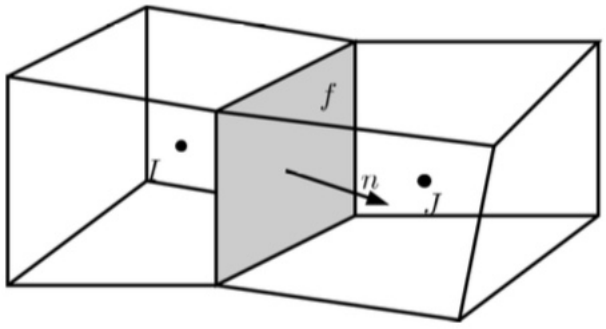

Figure 2.2: Sketch of two finite volume cells and their common face.

of the flow during the detonation part, the Harten-Lax-van-Leer-Contact (HLLC), introduced by Toro [48, 49], was used to calculate the convective terms and thus the flux. In fact, after reconstruction of the variables at the cell faces, discontinuities of the fluxes at the cell faces may be present. This scheme is very suitable for the simulation of high Mach number compressible flow as it leads to much better shock capturing than the standard schemes like the PISO scheme. HLLC scheme is essentially a modification of the HLL scheme, whereby the missing contact and shear waves are restored.

Basically, the governative equations of this part are unchanged from the previous one: the only difference is that there is no equation that couples speed and pressure, so no PISO loops. In addition, into energy equation the kinetic contribution is incorporated directly into the convective terms. Finally after having solved the convective fluxes, the diffusive fluxes are determined and the conservative equations solved.

Riemann fluxes

Since an accurate representation of shock and detonation fronts is indispensable in this work, a density-based solver has been developed. The convective flows are calculated using a Riemann solver [52, 53, 48]. As already reported, the conservative variable ϕ have been reconstructed by linear interpolation using the equation Equation 2.54. Taking this approach may occur new minimum and/or maximum on the cell surfaces, as illustrated for the one-dimensional case in Figure 2.3 leading to non-physical behaviour [35]. It is necessary then to introduce limiter functions instead of the gradient in order to recover physical solutions. In this work, a multi-dimensional cell-limited method is used [54].

After reconstruction of the variables at the cell faces, discontinuities of the fluxes at the cell faces are present. In order to calculate the convective flows over the cell faces, the HLLC[19] method ("Harten-Lax-van Leer-Contact") [48], which belongs to the group of Riemann solvers, has been calculated by solving a Riemann problem for the face.

[19] HLLC scheme is essentially a modification of the HLL scheme, whereby the missing contact and shear waves are restored.

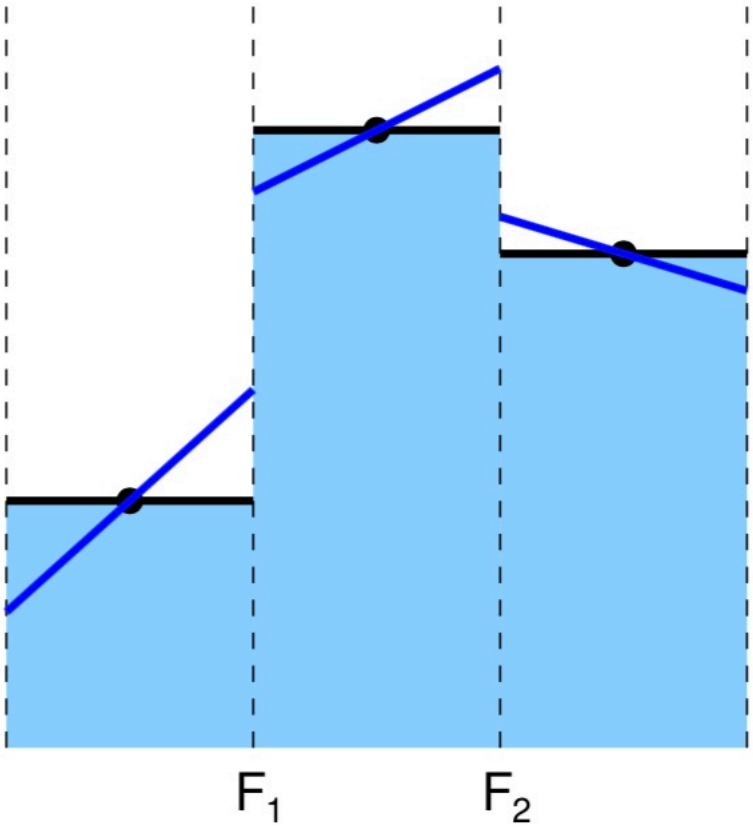

Figure 2.3: Schematic reconstruction of a variable from its centers of gravity on the boundaries.

Riemann Problem The analytical solutions of the general initial value problems (IVP) of hyperbolic systems are given in terms of the initial conditions. When the initial conditions have an intrinsic discontinuity, such that:

$$U(x,0) = \begin{cases} U_R & x > 0 \\ U_L & x < 0 \end{cases}$$

the special IVP is called Riemann problem, where U_R and U_L are two constant as shown in Figure 2.4. Of course, the problem has a discontinuity at $x = 0$ and it propagates a distant $d = at$ at time t. This particular characteristic curve $x = at$ will then separate those characteristic curves to the left, on which the solution takes on the value u_L, from those curves to the right, on which the solution takes on the values u_R (Figure 2.5).

The exact solution of the Riemann problem then requires an iterative numerical procedure

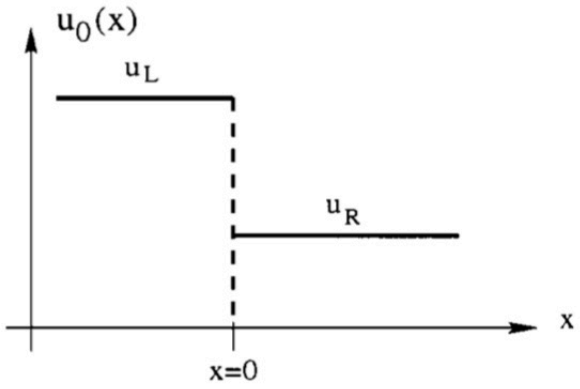

Figure 2.4: Illustration of the initial data for Riemann problem.

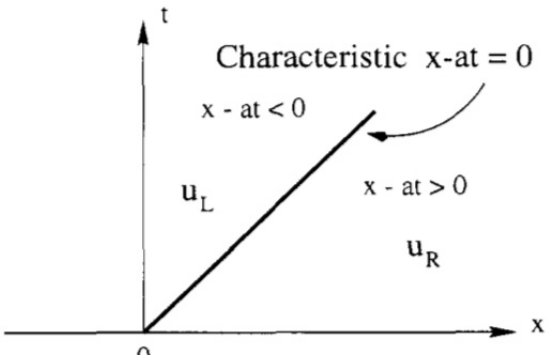

Figure 2.5: Illustration of the solution of the Riemann problem in the x-t plane for the linear advection equation with positive characteristic speed a.

due to the non-linearity of the governing equations. This iterative numerical procedure is computationally expensive, especially for simulations with a large number of cells. One way to avoid the iterations is to use an approximate solution of the Riemann problem instead of the exact one. The HLLC Riemann solver follows this approach basing its idea on decomposing the control volume in four different region in turn divided by three wave structures. Neglecting viscous and pressures terms into the reactive Navier-Stokes yields to Euler equations, which can be written conservatively as:

$$\frac{\partial \vec{\phi}}{\partial t} + \frac{\partial \vec{F}}{\partial \vec{x}} = 0 \tag{2.85}$$

with $\vec{\phi}$ and $\vec{F}$ defined as:

$$\vec{\phi} = (\rho u, \rho v, \rho w, \rho h_t) \quad and \quad \vec{F} = (\rho u, \rho u^2 + p, \rho uv, \rho uw, \rho u h_t + up) \tag{2.86}$$

These three waves divide the solution into four constant regions, as shown in Figure 2.6. Without limitation of generality, it is assumed that the variables are balanced over a cell area that is normal to the x-direction. The reconstructed variables on one side of a cell surface are denoted below by the index L, those on the other side of a cell surface with the index R. In order to calculate the flux from the state vectors on both sides of this surface, it is postulated in the HLLC solver that three waves (characteristics) are emanate from the interface, which propagate at constant velocities S_L, S_* and S_R where it is valid the following: $S_L < S_* < S_R$. The average characteristic always represents a contact wave, the two outer can be either compression shocks or expansion waves. Between the characteristics, there are always constant states. If the velocities are known, then the flux across the interface at $x = 0$ can be calculated from the state present there (e.g $\vec{\phi}_{*L}$ in Figure 2.6). Compared to the exact solution of the Riemann problem,

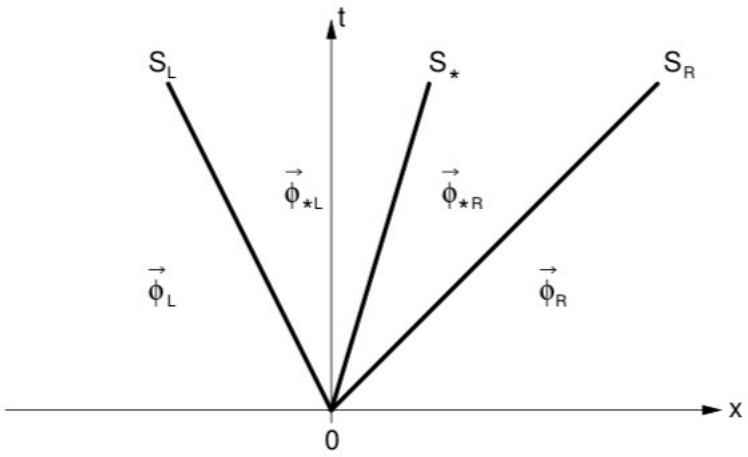

Figure 2.6: Three-wave structure of the HLLC Riemann scheme.

the HLLC solver makes the following simplifications in order to reduce the computational cost:

- all three waves represent discontinuities. Thus, the inner structure of an expansion is not resolved (within a single time step);

- The shaft speeds are not determined iteratively, but estimated from the initial state;

The estimate of velocities S_L and S_R from the initial states are given by:

$$S_L = u_L - a_L \qquad S_R = u_R + a_R \tag{2.87}$$

giving back a good representation of the propagation speed for expansion waves, but underestimates the propagation velocity of compression shocks [55]. For this reason, in this work, the determination of the previous velocities by the approach of Einfeldt [56] was preferred. Einfeldt showed by an eigenvalue analysis of the linearized Euler equations that the actual propagation velocities are much better for shock wave estimation:

$$S_L = \hat{u} - \hat{a} \qquad S_R = \hat{u} + \hat{a} \tag{2.88}$$

where:

$$\begin{aligned} \hat{u} &= \frac{\sqrt{\rho_L}u_L + \sqrt{\rho_R}u_R}{\sqrt{\rho_L} + \sqrt{\rho_R}} \\ \hat{a} &= \sqrt{\frac{\sqrt{\rho_L}a_L^2 + \sqrt{\rho_R}a_R^2}{\sqrt{\rho_L} + \sqrt{\rho_R}} + \frac{1}{2}\frac{\sqrt{\rho_L}\sqrt{\rho_R}}{(\sqrt{\rho_L} + \sqrt{\rho_R})^2}(u_R - u_L)^2} \end{aligned} \tag{2.89}$$

Knowing that the pressure p and the velocity u over the contact wave are constant, the formula for the velocity S_* can be derived [49]:

$$S_* = \frac{p_R - p_L + \rho_L u_L(S_L - u_L) - \rho_L u_R(S_R - u_R)}{\rho_L(S_L - u_L) - \rho_R(S_R - u_{R)}} \tag{2.90}$$

At this point, the approximate flow across the interface depends on the signs of the wave velocities:

$$\vec{F}^{HLLC} = \begin{cases} \vec{F}_L & 0 \leq S_L \\ \vec{F}_{*L} & S_L < 0 \leq S_* \\ \vec{F}_{*R} & S_* < 0 \leq S_R \\ \vec{F}_R & S_R < 0 \end{cases}$$

Hence, $\vec{F}_L$ and $\vec{F}_R$ can directly estimate from Equation 2.86. On other hand, to determine the

fluxes $\vec{F}_K$ (where K stands for L or R) one first calculates the corresponding state vector:

$$\vec{\phi}_{*K} = \frac{S_K - u_K}{S_K - S_*} \begin{pmatrix} \rho_K \\ \rho_K S_* \\ \rho_K v_K \\ \rho_K w_K \\ \rho_K h_{t,K} + (S_* - u_K)(\rho_K S_* + \frac{p_K}{S_K - u_K}) \end{pmatrix} \tag{2.91}$$

Considering the Rankine-Hugoniot relations:

$$\vec{F}_{*K} = \vec{F}_K + S_K(\vec{\phi}_{*K} - \vec{\phi}_K) \tag{2.92}$$

which finally yields to:

$$\vec{F}_{*K} = \frac{S_*(S_K\vec{\phi}_K - \vec{F}_K) + S_K[p_K + \rho_L(S_K - u_K)(S_* - u_K)](0, 1, 0, 0, S_*)^T}{S_K - S_*} \tag{2.93}$$

The convective transport of further passive scalars is analogous to the transport of the tangential velocities v and w, which are conserved across the characteristics. After calculating the convective flows with the HLLC scheme, the diffusive flows and any source terms can be calculated as already done in the pressure-based part.

An example of how the Riemann solver was used is presented below. First of all, a set of classes that solve the Riemann problem were implemented. For each equation involved within the solver, different fluxes definition were used. Taking the example of momentum equation, *rhoUFlux* was defined in order to estimate the convective term of the equation. However, the overall formulation of the equation is unchanged respect the previous pressure-based solver. Same considerations can be done for the other equations involved into the solver.

```
solve
(
        fvm::ddt(rho,U)
```

```
            + fvc::div(Riemann.rhoUFlux())
            - fvm::laplacian(turbulence->muEff(), U)
            - fvc::div(tauMC)
            ==
               rho*g
        );
            rhoU = rho*U;
```

2.4.4 PaSR Combustion Model

The combustion model used in this work belongs to the Partially Stirred Reactor model (PaSR), which uses complex chemistry to model ignition and mixed-controlled combustion. For these reasons, it requires high computational time and is suitable for diagnostic purposes. However, it provides very good insight of the combustion process taking place during the ignition and combustion phases. In the PaSR approach, a computation cell is split into two different zones: in one zone all reactions occur, while in the other one there are no reactions. Thus, the composition changes due to mass exchange with the reacting zone. Furthermore, the reacting zone is treated as a Perfectly Stirred Reactor (PSR), in which the composition is homogeneous. According to the PaSR concept, the concentration of each species i at the exit of reactor can be defined as:

$$c_1^i = k^* c^i + (1 - k^*) \cdot c_0^i \tag{2.94}$$

where k^* is the mass fraction of the mixture which reacts. Then, the model distinguishes between three molar concentrations (Figure 2.7):

- c_0^i : is the averaged concentration in the feed of the cell and may be considered as the initial averaged concentration in the cell;
- c^i : is the unknown concentration in the reaction zone on a sub-grid level in the unknown reactive fraction of the cell material;

- c_1^i : is the sought for, time-averaged exit concentration. his is also the averaged concentration in the cell.

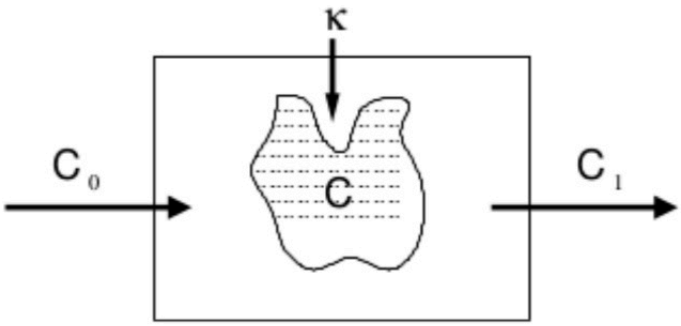

Figure 2.7: Conceptual picture of the Partially Stirred Reactor.

According to Equation 2.94, c_1^i is a linear interpolation between c^i and c_0^i and the whole combustion process can be split in sub-steps, proceeding in parallel (Figure 2.8):

1. the initial concentration in the reaction zone changes from c_0^i to c^i;
2. The reactive mixture c^i is mixed by turbulence with c_0^i resulting in the averaged concentration c_1^i.

Since c_1^i is the initial value for the next timestep, the time between c_0^i and c_1^i must be the integration step, τ. The turbulence mixes c^i with c_0^i, hence the time difference between c^i and c_1^i must be the characteristic time for turbulence, τ_{mix}. Assuming that the slope of the curve in Figure 2.8 is equal to the reaction rate in the reaction zone, it results in:

$$\frac{c_1^i - c_0^i}{\tau} = \frac{c^i - c_1^i}{\tau_{mix}} = f(c^i); \quad k^* = \frac{\tau}{\tau + \tau_{mix}} \tag{2.95}$$

Here, f(c^i) is reaction rate of the species i during time-step τ which is modelled with an Arrheniuss equation. To obtain c_1^i, it is now necessary to eliminate c^i in Equation 2.94. Using Taylor expansion, the term f(c^i) can be expressed as:

$$f(c^i) = f(c_1^i) + \frac{\partial f}{\partial c}(c^i - c_1^i) \tag{2.96}$$

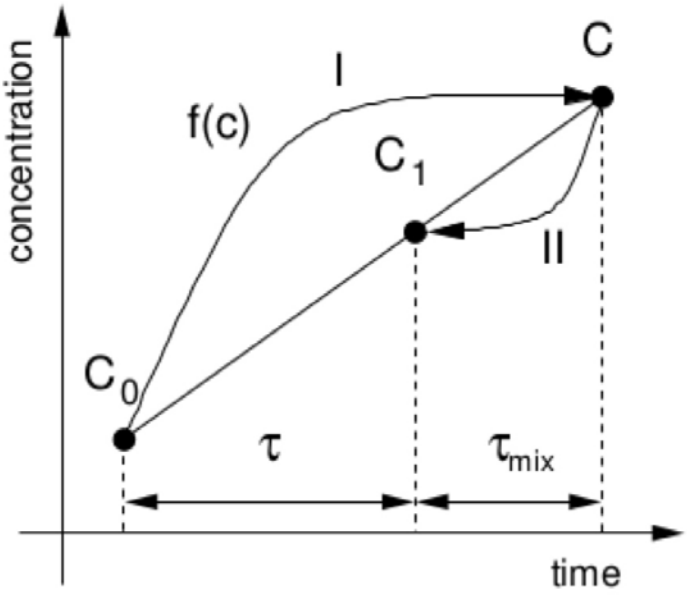

Figure 2.8: The reaction/mixing step procedure.

The term $\frac{\partial f}{\partial c}$ is assumed to be the reciprocal of a chemical time scale:

$$-\frac{\partial f}{\partial c} = \frac{1}{\tau_c} \tag{2.97}$$

and is calculated as:

$$\frac{\partial f}{\partial c} = \frac{\dot{\omega}(c_1^i) - \dot{\omega}(c_0^i)}{c_1^i - c_0^i} \tag{2.98}$$

where $\dot{\omega}(c_1^i)$ and $\dot{\omega}(c_0^i)$ are the reaction rate expressions of species i calculated at the beginning and at the end of the time step. Thus, Equation 2.96 becomes:

$$f(c^i) = f(c_1^i) - \frac{(c^i - c_1^i)}{\tau_c} \tag{2.99}$$

Substituting the expression of τ_c in Equation 2.94, the following expression is finally obtained for the sub-grid reaction rate:

$$\frac{c_1^i - c_0^i}{\tau} = \frac{\tau_c}{\tau_{mix} + \tau_c} f_m(c_1^i) \tag{2.100}$$

The reactive fraction k_i becomes equal to:

$$k_i = \frac{\tau_c}{\tau_{mix} + \tau_c} \tag{2.101}$$

Several expressions were proposed for the mixing time τ_{mix} [57, 58]. In this dissertation, it is assumed to be:

$$\tau_{mix} = C_{mix}\sqrt{\frac{\mu_{eff}}{\rho\epsilon}} \tag{2.102}$$

where C_{mix} needs to be estimated a priori. Typical values of C_{mix} are in the range from 0.001 to 0.3 [59].

2.4.5 Chemical model

The Arrhenius Law, which is for simplicity reported below, is used for calculating the reaction rates ω_i:

$$\omega_i = A_i T^{\beta_i} \exp\left(\frac{-E_{a,i}}{RT}\right) \tag{2.103}$$

that play a fundamental role for calculating the chemical part. In fact, the rate of an elementary chemical reaction is proportional to the product of the concentrations of reactants. For example, taking an elementary reaction between nitrogen trioxide and carbon monoxide:

$$NO_3 + CO \xrightarrow{\omega} NO_2 + CO_2 \tag{2.104}$$

the law of mass action asserts,

$$\begin{aligned} \frac{d[NO_3]}{dt} &= -\omega[NO_3][CO] \\ \frac{d[CO]}{dt} &= -\omega[NO_3][CO] \end{aligned} \tag{2.105}$$

where it is easy to verify that the entire reaction is modeled by a system of ODE. An extension of this way of thinking to more detailed reaction schemes is presented in appendix E. In this work, the ODE system is solved by Runge-Kutta method [60].

2.5 Validation of the zndFoam

The solver described above has been validated with focus on the transport properties and reaction rates. For each numerical simulation, the setup case will be described with focus on mesh structure, initial and boundary conditions. All the simulations performed will be compared with experimental data available in literature. The results will be presented in chapter 3.

2.5.1 1D Shock Tube

Since the density-based solver uses Riemann scheme to handle supersonic flow, the shock capacity is verified by simulating the classical Riemann problem. The shock tube problem is a common test for the accuracy of computational fluid codes: it consists of a one-dimensional Riemann problem with the initial conditions, e.g temperature and pressure, for left and right states of an ideal gas.
The numerical shock tube is modelled as a one-dimensional tube with a total length of $200mm$, closed at its ends, and an equidistant grid with $1.0mm$ spacing only on x-direction, as shown on Figure 2.9. It is divided into two equal regions by a thin diaphragm and each region is filled with the same gas, but with different thermodynamic parameters. The region with the highest pressure is called the driven section of the tube, while the low-pressure part is the working section. The gas being initially at rest, the sudden breakdown of the diaphragm generates a high-speed flow, which propagates in the working section.

In order to replicate the experimental case, the four sides are modelled as walls, imposing a no-slip condition, and a zero initial velocity has been imposed in each direction. The initial conditions for the tube filled up with air are given in Table 2.3 Since analytical solution is

Position	Pressure [MPa]	Temperature [K]
$x < 0$	0.1	300
$x > 0$	1	800

Table 2.3: Initial conditions of the shock tube

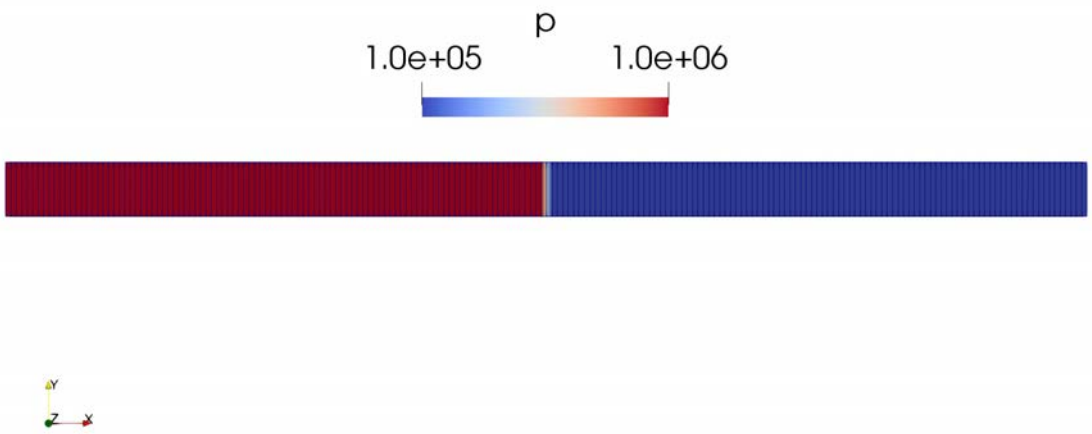

Figure 2.9: Shock tube computational domain.

available for this case, one can test it against the numerical solution, and get information how well a code captures and resolves shocks.

It must be noted that, only for this case, the flow has not reactive features and viscous effects is neglected, then solving one-dimensional Euler equations.

2.5.2 Hydrogen-Air Detonation in a DDT tube

Since the numerical results were compared with Ettner's experimental results, the numerical domain is directly taken from Ettner's phD thesis [39] using the same parameters imposed, where Figure 2.10 shows the domain of the considered cases. Then, the model has been tested against experimental results gained in a closed rectangular channel of length $L = 5.4m$, height $H = 60mm$, and width $W = 300mm$ whereas only 2D simulations were taken into account.

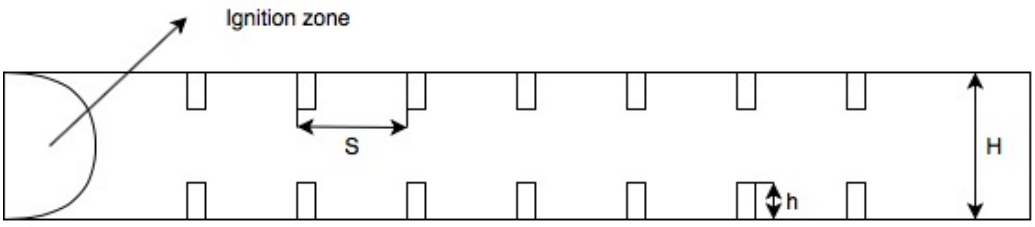

Figure 2.10: Schematic sketch of the channel geometry

The channel is equipped with flat plate obstacles of height h, placed on top and bottom walls, spaced at a distance of $S = 300mm$ from each other. The first obstacle is placed at $x = 0.25m$ from the front plate where a spark plug ignites the mixture. The last obstacle (7^{th}) is placed at $x = 2.05m$ and the remaining part of the channel is unobstructed [35]. The obstacle blockage ratio BR is determined by the obstacle height h:

$$BR = \frac{2h}{H} \tag{2.106}$$

In this work only blocking rate of 0.03 was investigated[20]. These series of notches are taken into account in order to promote the flame acceleration and DDT. In fact, the high turbulent intensity produced by these leads to a greater homogeneity of the mixture and an acceleration of the flow promoting detonation.

Initially the flow is at rest with the following initial conditions:

T_0	p_0	yH_2	yH_2O	yN_2	yO_2
293K	101325Pa	0.02276	0.0	0.74959	0.22764

Table 2.4: Physical conditions of the simulation.

where it is used nitrogen as inert species. In order to promote the deflagration ignition is modelled by patching the site of ignition at $x = 0$ with a burnt mixture and high temperature. The initial turbulence is vanishingly small and consequently the flame starts to propagate at laminar flame speed, excellent for the pressure-based solver. Then, at the beginning low turbulence values in the ignition region were imposed. Finally, as already said, turbulence is modelled using the $k - \omega$-SST model which is known for its good performance for both free-stream jets and wall-bounded flow [61, 62].

Grid sensibility analysis was also conducted. Because of the many variables involved in each simulation, the only physical parameter capable of characterising the mesh is the detonation cells width. Using a structured square mesh with different sizes (0.5x0.5mm, 1x1mm, 2x2mm, 4x4mm), detonation cells size have been analysed in comparison to the computational time necessary for the simulation. In Figure 2.11 is presented the analysis showing that the best

[20] Refereed to BR30%

mesh size for these simulation is the intersection between two curves: the detonation cells width for different mesh sizes and their computational costs. In fact, by modifying the mesh of only

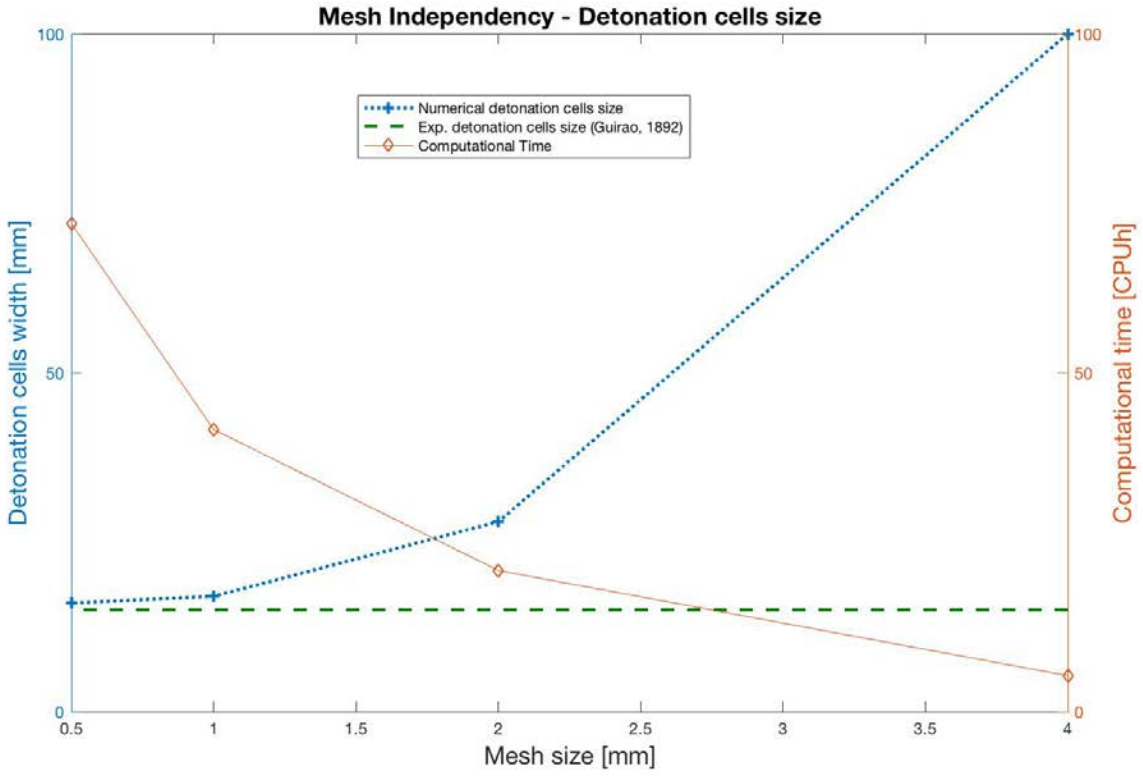

Figure 2.11: Mesh independence based on the detonation cells size.

few millimetres, the nature of the flow is significantly modified: using 4x4 mm, there are no microscopic effects, DDT and detonation cells. But using 1x1 mm, the flow dynamic is completely different showing features really detailed, such as the location of the DDT.

According to the previous analysis, the tube is discretized with a uniform, rectangular grid of 2mm grid spacing. For this test case, two different reaction schemes have been used to perform different simulation: a reduced scheme, proposed by Wang [63], based on one reaction (Table C.1) and a detailed one, proposed by O'Conaire [25], based on 19 reactions. This reaction has been used because of the wide range of validation (from 293K to 2700K) and for a wide range of pressures (from 0.05 to 87 atm).

In order to investigate also the diffusion effects, relating to combustion, both homogeneous mixture and mixture with concentration gradient were considered, with the mole fraction equal to 25% (at least, in average, for the inhomogeneous mixture). The hydrogen concentration

distribution for the inhomogeneous mixture equal to 25% is shown in Figure 2.12. Examples of the polynomials used for different mole fractions can be found in chapter D. Moreover, also pressure data will be compared with experimental ones, acquired at $x = 3.2m$ (close to the end of channel).

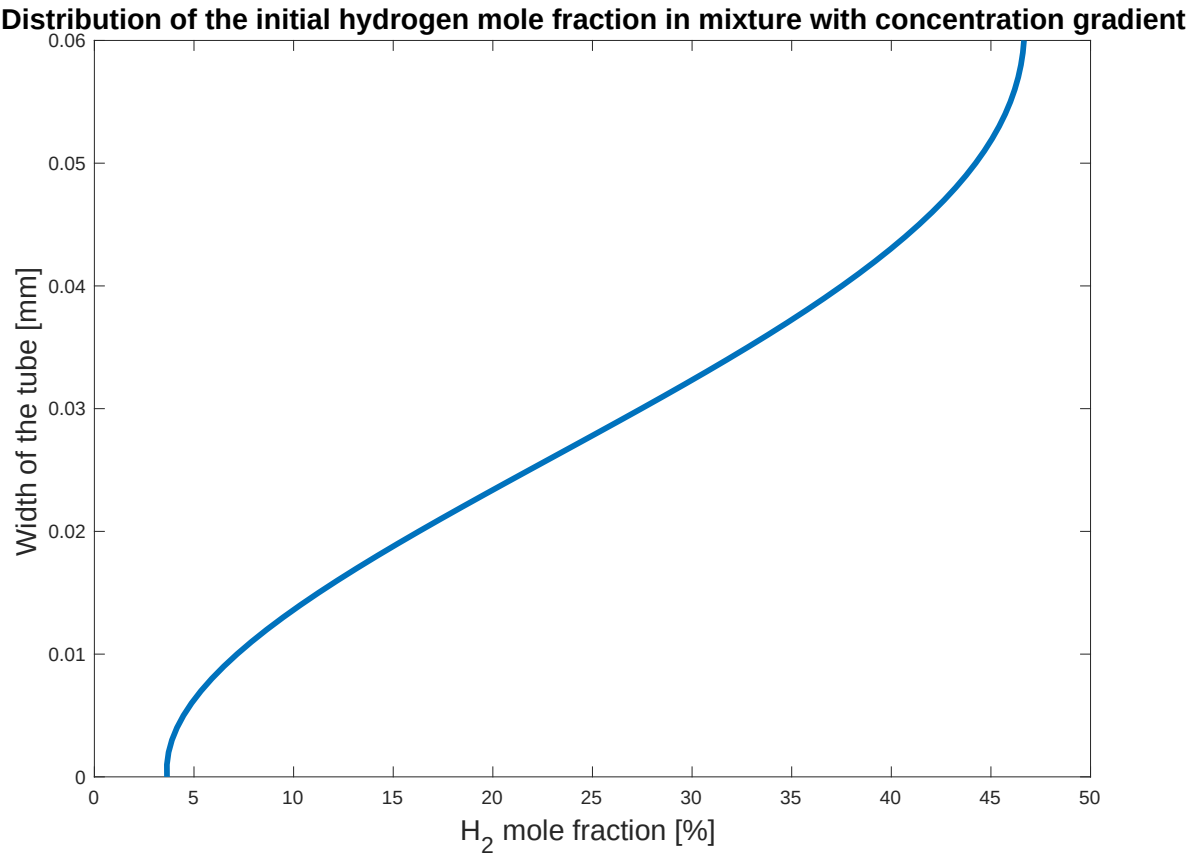

Figure 2.12: Distribution of the initial hydrogen mole fraction in the hydrogen-air mixture with concentration gradients.

2.5.3 Acetylene-Oxygen Detonation in a DDT Tube

Similarly to what previously described, with similar peculiarity, a scheme of the detonation chamber used for experimental studies and numerical simulations is shown in Figure 2.13, where a more detailed description of the experimental procedure can be found in [64]. As well as done before, it is not calculate the process of filling the gas chamber with acetylene and oxygen but it is imposed a ignition section where the flow is fully premixed. Analogously, the

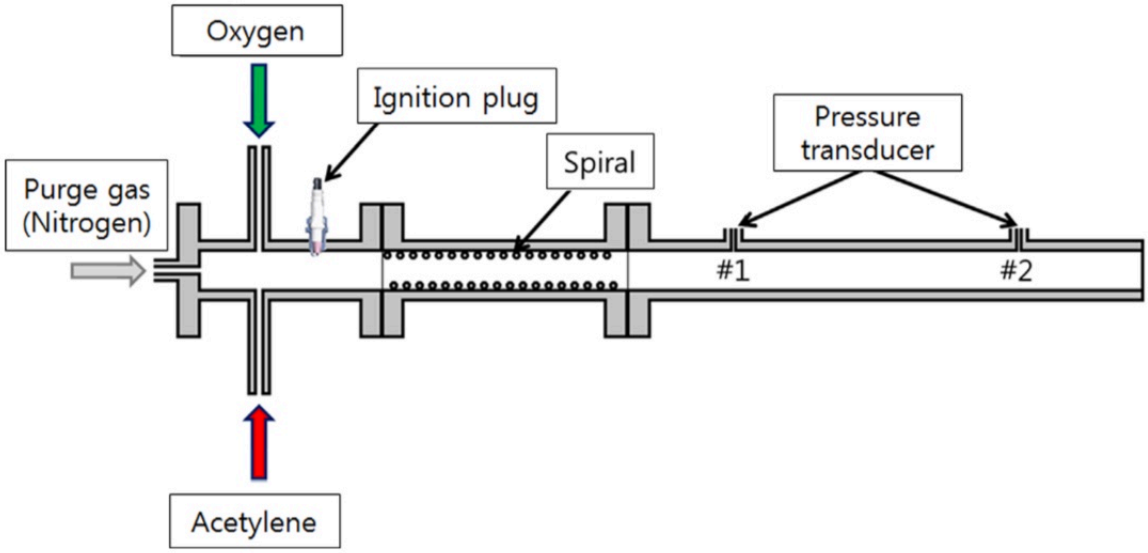

Figure 2.13: Schematic sketch of acetylene-oxygen test case.

whole system was closed, and adiabatic no-slip conditions imposed at the walls. The diameter of the tube is equal to $24mm$, the total length is $1240mm$, the length of the ignition section is 100mm and the length of the spiral section is 300mm. The blocking ration can be estimated around 50%. Instead of imposing a mass fraction of the fuel, as done for the previous case, an equivalence ratio (Equation 2.29) equal to unity is imposed.

Usual $k-\omega-SST$ turbulence model was used and grid sensibility was performed, as well. Thus, the tube is discretized with a uniform, rectangular grid of 1mm grid spacing. For this test case, only the mechanism proposed by Smirnov [65], including 11 reactions with 9 components was used, because of the limited availability of such mechanisms in the literature. Moreover, it is impossible simulating this special mixture with only one reaction due to the high energy-power of acetylene.

Contrary to the previous case, only an homogeneous mixture was considered, imposing only the equivalence ratio.

2.5.4 Detonation shock tube - Detonation cells

As already said in the introduction, detonation cells size is also investigated because capturing detonation on cellular level would provide resolved numerical simulations. Even if the simulation

is performed on a fine mesh, it can happen that these structures will never be encountered if nature is not given enough space and time to develop them [19]. Y.Eude [22] and Oran et. al [66] given small instabilities to the initial pressure field in order to speed up the generation of the cells, since these appear due to nature's instabilities. If the tube is too small, detonation can physically not originate or propagate, for H_2-Air the critical tube diameter is three times the length of a cell size [67]. The order of magnitude of cell sizes for stoichiometric H_2-Air mixtures at $0.1MPa$ and $293K$ is around $15mm$ [20].

The computational domain is a two dimensional shocktube with a length of $1m$ and a width of $0.1m$ and a computational cell size of $1x1mm$, according to the grid sensibility described above. The forced instability is made by high temperature and high pressure, at the beginning, for promoting the detonation wave.

Chapter 3

Results

In this chapter, numerical results coming from the previous test cases will be presented. These will be always compared with either available experimental data (using the same test case) or other solvers with similar features. A brief discussion for each result will be performed as well.

3.1 1D Shock Tube

The results of the shock tube case are presented in Figure 3.1. For comparison, a standard combustion solver rhoReactingFoam[1], has been taken as criterion for comparison since it is supposed to be able of simulating high speed reacting flow. On other hand, the analytical solution, proposed by J. D. Anderson [68], is considered as well. At 0.1 ms data have been sampled from each cell and compared each other to the different physical fields. One can see that rhoReactingFoam, that based essentially on a PISO scheme including at the end of the cycle a density correction, not only predicts a wrong shock location, but also is in general very dissipative and displays abnormal behaviour (e.g for temperature). This can be attributed to the non-conservative formulation of the Navier-Stokes equations which is inherent to the pressure-based scheme. Moreover, the density correction makes the density values on the boundary reliable with respects to the theoretical ones, but the trend between them completely

[1] Already available in the openFoam package.

random, not being to be able of predicting the state variable immediately after the shock. It can be concluded that standard openFoam solvers[2] are not suitable for the simulation of fast deflagrations and detonations.

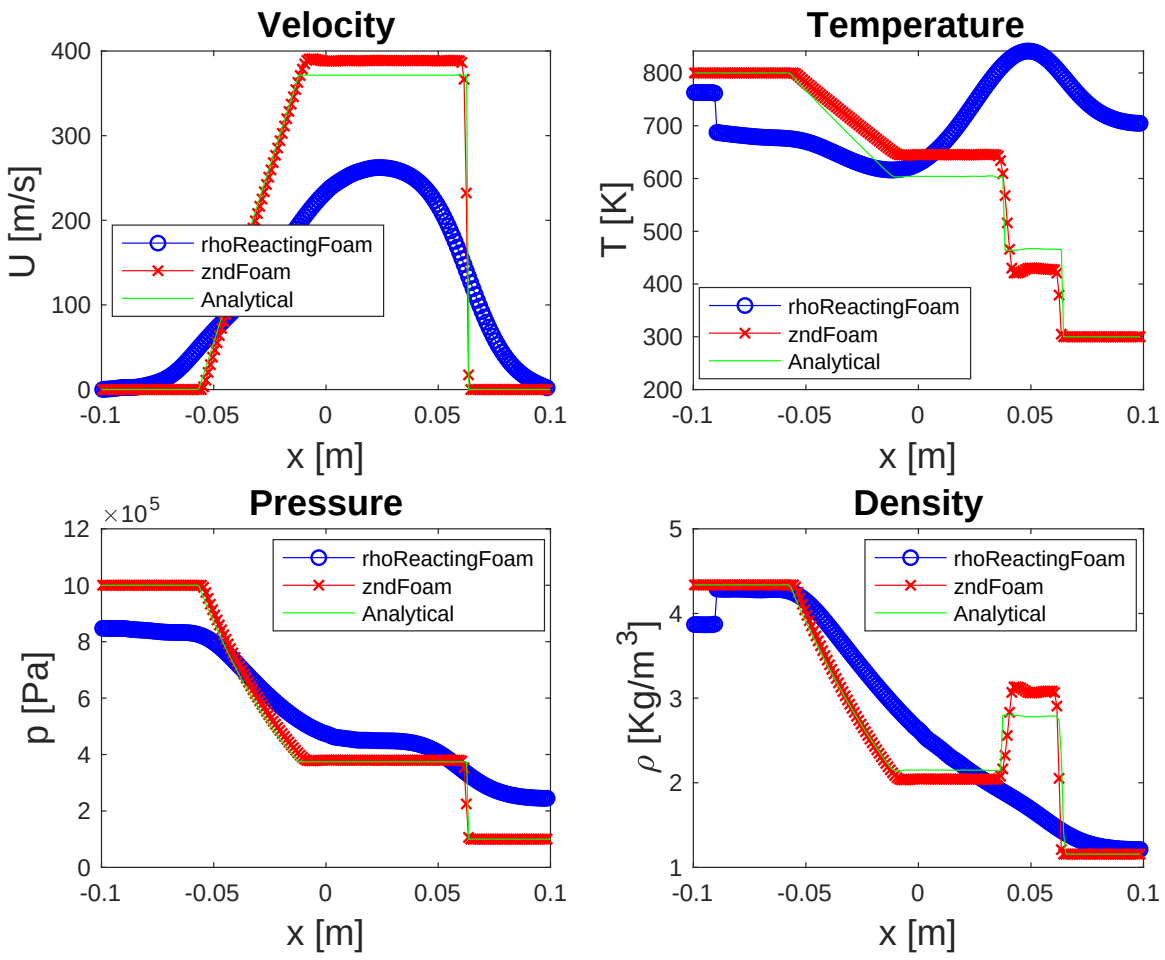

Figure 3.1: Solution comparison between rhoReactingFoam, zndFoam and the analytical one.

On other hand, HLLC scheme shows a much better performance providing accurate shock positions and almost same magnitudes, strictly closer to the theoretical solution. The solutions coming from zndFoam are more stable than the standard solver where oscillations appear in all the fields. The maximum relative error of zndFoam is around 10% much lower than rhoReactingFoam. It must however be noted that again this scheme presents some issues in particular on density and temperature: these can be related to the low-speed flow at the time of acquiring the data. In fact, at $t = 2.0ms$, the relative errors are already lower than the

[2]In this case only rhoReactingFoam.

previous ones endorsing the hypothesis.

Thus, it was decided to use the HLLC scheme as a basis for the detonation part solver in this work. Since, as already shown, it does not work properly in very low Mach number flow, PISO scheme is also implemented and used just to start computations in stagnant flow.

3.2 ddtFoam - Homogeneous H_2-Air Mixture

Although the Ettner's solver was not supposed to work pretty well for detonation engines applications, a first verification of it, using only homogeneous H_2-Air mixture, was performed in order to characterise the main features. The Ettner's test case described before was implemented, filling up the tube with 25% of fresh H_2 mixture. As usual, small circular zone of high temperature of burnt mixture is imposed to trigger a deflagration. The initial pressure and temperature of the mixture were respectively $0.1Mpa$ and $273K$. The experimental and numerical results for flame speeds were acquired between two subsequent photodiodes applying the first order derivative:

$$V_i = \frac{x_{i+1} - x_i}{t_{i+1} - t_i} \tag{3.1}$$

where t_{i+1} and t_i represent the time at which the flame passes the photodiodes located at x_i and x_{i+1}, respectively. In general, the numerical results are in good agreement with the experimental ones and the DDT is well simulated but some weird effects occur. Around at $12ms$, i.e. when the flame exceeds the first series of notches, the fast deflagration should have already started, but not in this case. The deflagration part is quite slow respect the experimental results leading to retarded DDT. Moreover, on the detonation part, the flame speed is overestimated[3] yielding to high pressure (recorded by sensors at the exit of the tube) and high temperature. Both of results are presented in chapter F: the pressure detected at the end of the tube on the midplane is wrong both on peak position and magnitude. Obliviously, this is related to the wrong estimation in velocity and then to wrong temperatures that overestimate the combustion, i.e. the production of the species. It must not be forgotten there is no equations

[3] Around 2000m/s instead of 1800m/s

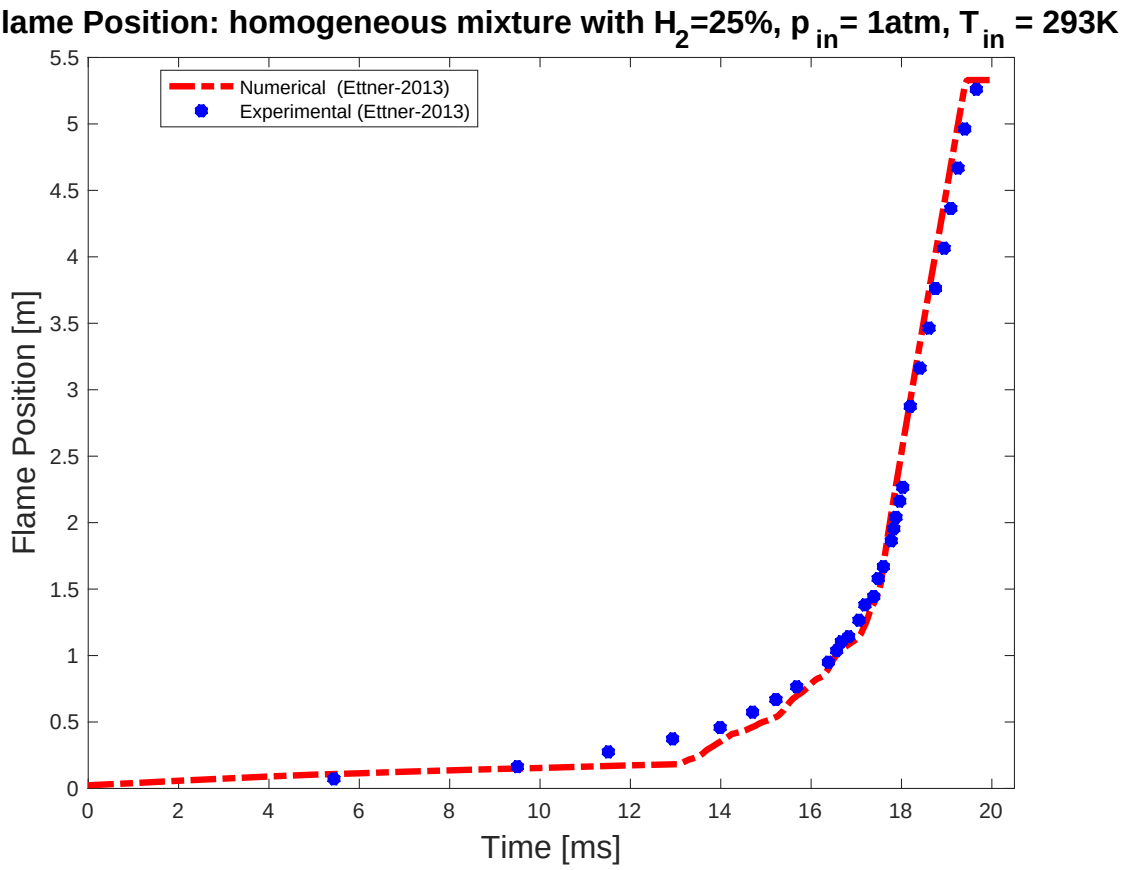

Figure 3.2: Comparison between numerical and experimental results using ddtFoam solver.

for species and the energy equation is not complete, i.e. not containing all the terms related to the combustion: so there is no possibility to reduce these effects, for example with safeguard parameters. Moreover, the table chemical data stored on the solver were acquired on standard conditions which may be different from our simulations.

These issues related to the impossibility of choosing the reaction mechanism desired, make one think of using different solver: even if the macroscopic details are well simulated, the microscopic ones are completely neglected[4]. In fact, in order to study also heat transfer phenomena or nature of shock waves, microscopic details, such as detonation cells, must be taken into account.

[4]Due to the character of the solver.

3.3 zndFoam - H_2-Air

In this section, the results achieved by using the solver zndFoam are provided. The test case used for these analyses is the same described in chapter 2, basically equal to the Ettner's case. Homogeneous and inhomogeneous mixtures are taken into account for different analysis, both macroscopic and microscopic. For each result, a brief discussion in terms of different physical variables is presented. Detailed pressure contours in the detonation region at different time steps are presented as well. Finally, for each simulation, nitrogen (N_2) was used as inert[5] species.

3.3.1 Homogeneous mixture

Numerical results for the homogeneous case with 25% of hydrogen are shown below. Only for this case, both reduced and detailed mechanism were considered for the analysis in order to make a comparison between the solutions. The mechanisms are presented in chapter B.

OneStep Mechanism

The results achieved by using the reduced mechanism are shown in Figure 3.3 with regards to positions and speed flame. Clearly, even if the flame positions are in good agreement with the experimental ones, showing almost the same Ettner's trend, the speed is completely overestimated. The green line indicates the theoretical value of the detonation velocity whereas the dots line indicates the experimental one[6]. Numerical speed results using both solvers, zndFoam and ddtFoam, are shown respectively by using red and black solid line whilst blue line shows the experimental results acquired by Ettner. The latter have an oscillatory behaviour that, as reported in Ettner's paper [39], are due to an experimental mistake and low precision of the sensors used.

Of course, a lot of these issues are related to the low precision of the mechanism. In fact,

[5] Diluent.

[6] The sharp values are reported in chapter A

only one reaction must reduce, dissociate, recombine and consume the species involved in the mixture, at the same time. It is clear that it is impossible to include all of them in only one reaction. For example, the energy activation of the reaction is much lower than the real one, in order to permit the more easily the dissociation, leading to the high reactivity of the flow and then to overshot temperatures. As shown by temperature and pressure contours in chapter F, both of them are completely arbitrary: temperature exceeds most of the times 5000K, with some point around 6000K and the pressure peak position is early than the experimental position, such is shown in Figure F.2.

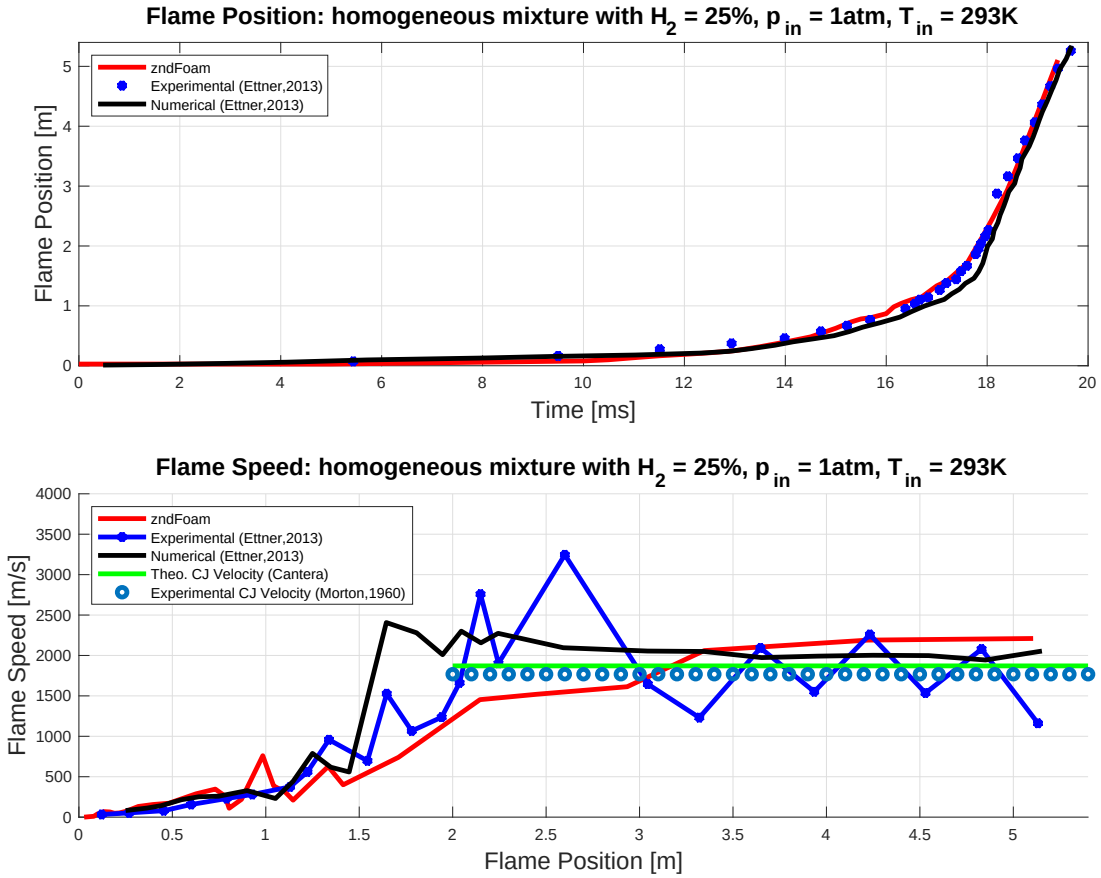

Figure 3.3: Flame position in function of time (top) and flame speed in function of tube length (bottom).

At this point should be clear that the reduced mechanism is not able to simulate microscopic features of the flow. This is confirmed by the following result: the detonation test case was simulated in order to get some information about the detonation cells. Same initial conditions

were imposed in order to promote the detonation. The results is shown in Figure 3.4

Even if the cells are not so marked, at least the smallest ones, the macroscopic effects as

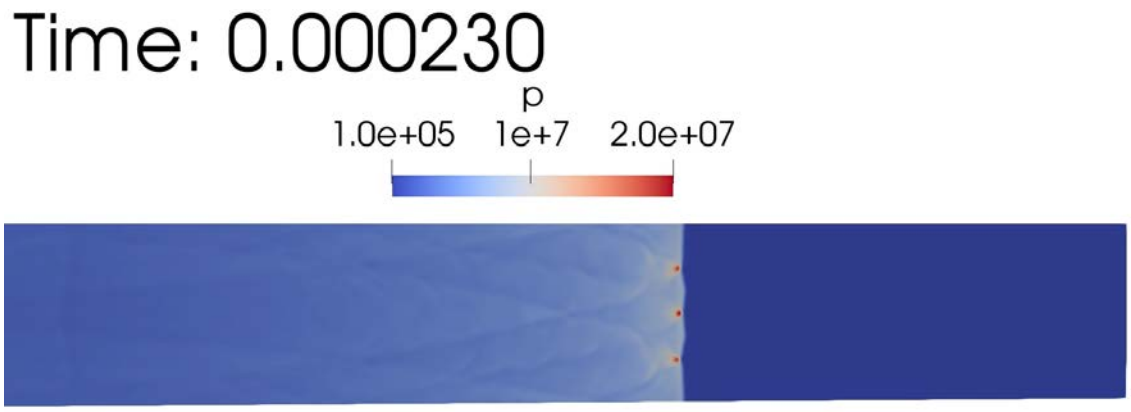

Figure 3.4: Detonation cells using OneStep mechanism.

the oblique shock waves and triple points present real features. The details of the flow are lost around the normal shock wave since the mechanism is not able anymore to reproduce microscopic details.

Detailed Combustion Modelling

Having seen the issues arising from the use of reduced mechanism, a detailed one was taken into consideration: on the same outline, the results of flame positions and flame velocities are shown in Figure 3.6. It can be seen that the agreement between numerical and numerical results is very good. Near the ignition zone, the flame propagates at a nearly constant laminar speed around several meters per second. When it exceed the first series of notches, the flame speed is abruptly increased, which can be attributed to mutual amplification of combustion-induced expansion and turbulence generation due to interaction with obstacles [39]. Subsequently, the flame speed continues to increase reaching velocities around 400 m/s between the second and third sets of obstacles. Following this, the flame speed starts to increase steeply, resulting in DDT transition around $x = 2.0m$. This transition is shown in Figure 3.5 in terms of pressure.

Looking the flame speed, three main effects are evident. On the deflagration part, the velocity

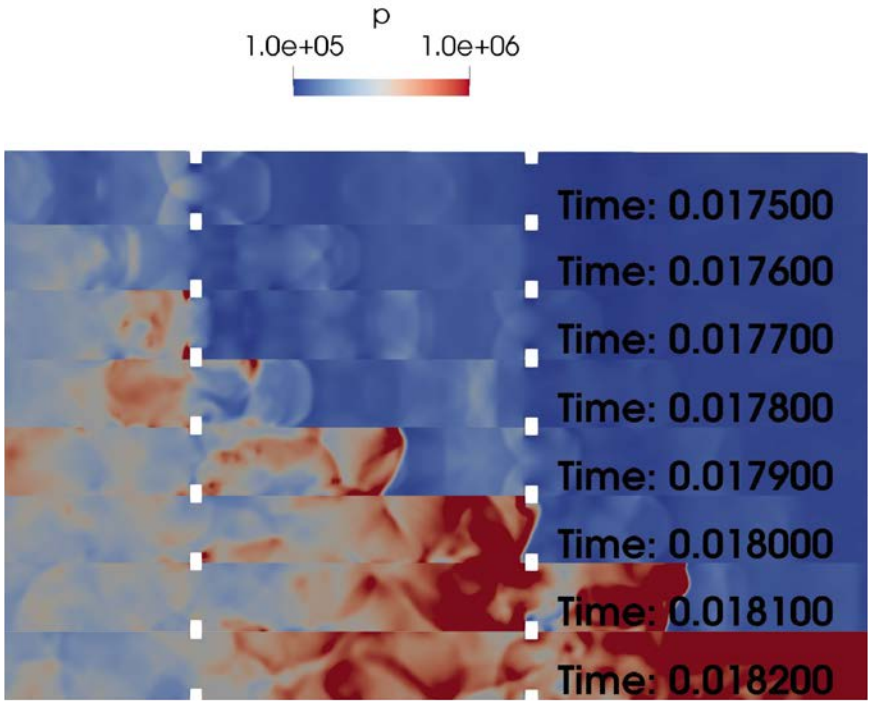

Figure 3.5: Predicted contours of pressure during DDT.

is after all well simulated with some oscillatory behaviour[7]. On the DDT transition, the speed is a bit underestimated, showing a linear trend, perhaps due to a wrong instant of switching between pressure-based and density based solver. At the end, detonation speed is perfectly simulated with respect to the theoretical and the experimental one. For the same issues mentioned before, Ettner's experimental results for the velocity have not been considered. Thus experimental value, acquired in the same condition, of detonation velocity proposed by Morton [69] was taken into account. At the same time, using Cantera package (available online [13], theoretical CJ velocity was estimated. At the end, Figure 3.6 shows a perfect agreement among theoretical, numerical and experimental values of detonation velocities. The percentage errors compared to both experimental and theoretical velocities are lower than 3%, pointing out to a reliable simulation.

In order to verify the reliability of the simulation and for future thrust estimations, pressure peaks of the flow were compared to the experimental data acquired by Dr. Ettner[8]. Figure 3.7

[7]Most probably due to the way of acquiring the flame positions.
[8]The pressure probe was located on the top wall, that is why is written: "height=100%"

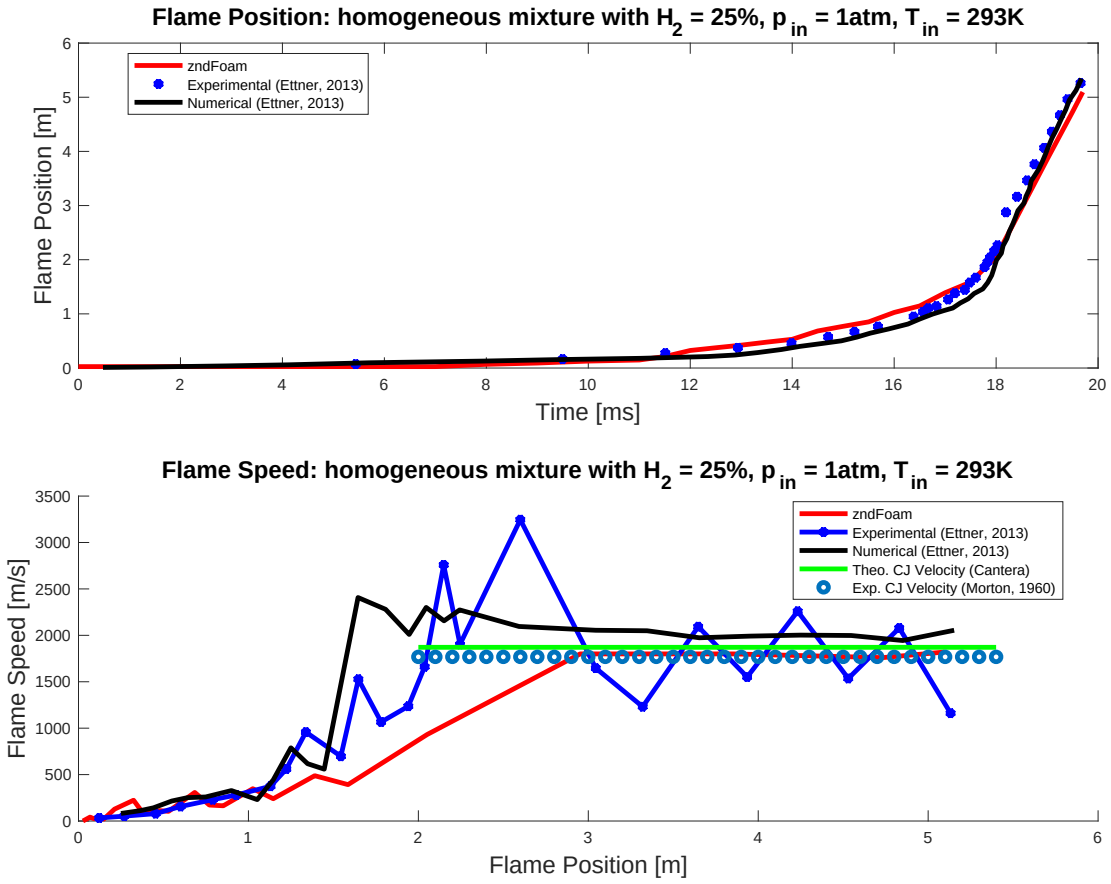

Figure 3.6: Flame position in function of time (top) and flame speed in function of tube length (bottom).

compares the predicted numerical pressure profile (red solid line) with the experimental one (blue solid line), at $x = 3.2m$. Overall, the predicted pressure profile follows the experimental trend and match reasonably well each other. The first peak, due to the detonation wave itself, is in good agreement with the measurements: the solver is then able to simulate well both position and value of the pressure peak. The second peak, due to the reflection wave caused by the wall condition imposed at the end of the channel, is latter than the measurements but again the value of the peak is well predicted. The error on predicting the position is almost twice respect to the first peak because the pressure wave, begin reflected from the wall, makes twice the path storing then a double error. Anyway, the percentage error of the peak position is around 2%, widely within the admissibility range.

Finally, microscopic effects were investigated also in this case for heat transfer motivations and

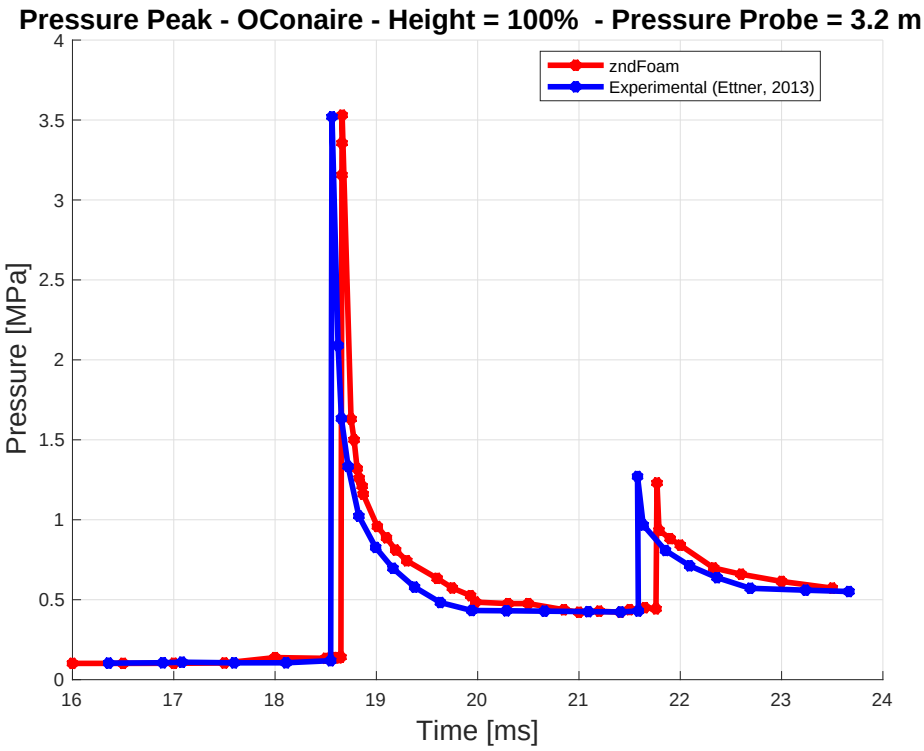

Figure 3.7: Comparison between predicted and measured pressure profile at $x = 3.2m$.

reliability of the solver. As usual, detonation cells size were investigated using his test case, as in the previous case. For the homogeneous mixture, a close up on the result coming from the detonation shock tube is shown in Figure 3.8.

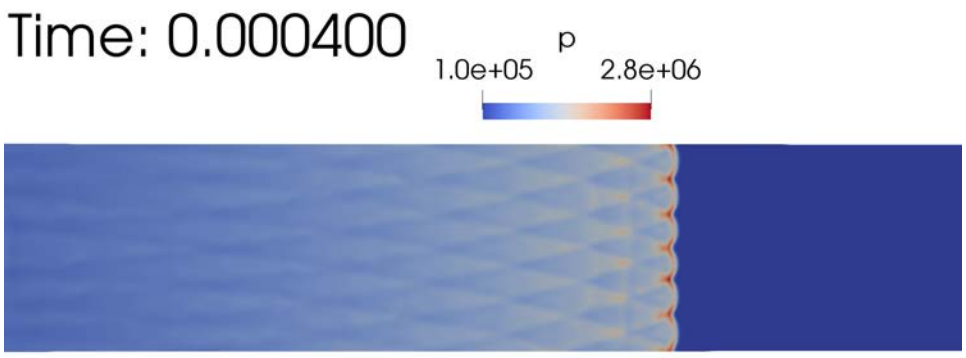

Figure 3.8: A close-up on the detonation cells.

The detonation cells are clearly marked and the usual symmetric structure is perfectly simulated. Moreover, on the front, triple points show the typical shock waves with high pressure peaks as predicted by theory and experimental simulations. Finally, the detonation cell width

is compared with experimental value: $17mm$ is the experimental value estimated on the same conditions available on the database GALCIT [70]. On other hand, the numerical value coming from this simulation is around $18mm$, a result that is basically excellent for this kind of simulation, leading to a percentage error of 6%) [71].

3.3.2 Inhomogeneous mixture

Same analyses were performed assuming inhomogeneous mixture. Furthermore, having shown that detailed scheme works much better than reduced one and having sufficient computational power available only detailed scheme was considered for this simulation. Again, reasonably good agreement has been achieved between numerical and experimental results, as shown in Figure 3.9. The predicted flame positions, in this case, are in even better agreement with the measurements than for the homogeneous H_2-air mixture, proving a suitable behaviour of the solver under concentration gradients. Looking the bottom plot of Figure 3.9, the flame speed is smoother than the previous cases, meaning that the pressure does not interact with the flame, having reflected off from the obstacles. In this case, the DDT occurs before than the previous case, i.e. around $t = 11ms$. Moreover, the shape of the flame is completely different as shown in Figure F.3, because the combustion rate is not anymore uniform due to mixture gradient.

The main difference of using mixtures with concentration gradients is that hydrogen cannot be completely consumed especially in the region of rich fuel. This part of unburnt hydrogen may be potentially re-ignited when one more fresh air is available. Before the first series of notches, the simulation may be assumed as a normal deflagration, but as soon as the flame exceed the first series of obstacles, due to turbulent interaction, the flame front speed rises quickly. From Figure F.3 a deflagration to detonation transition is clearly visible: pressure starts to rise drastically after reflection against the wall and initiates the detonation combustion. Also in this case, the numerical detonation velocity was compared with both experimental and theoretical value. Unfortunately, in this case the numerical values, around 1600m/s, is strictly lower than

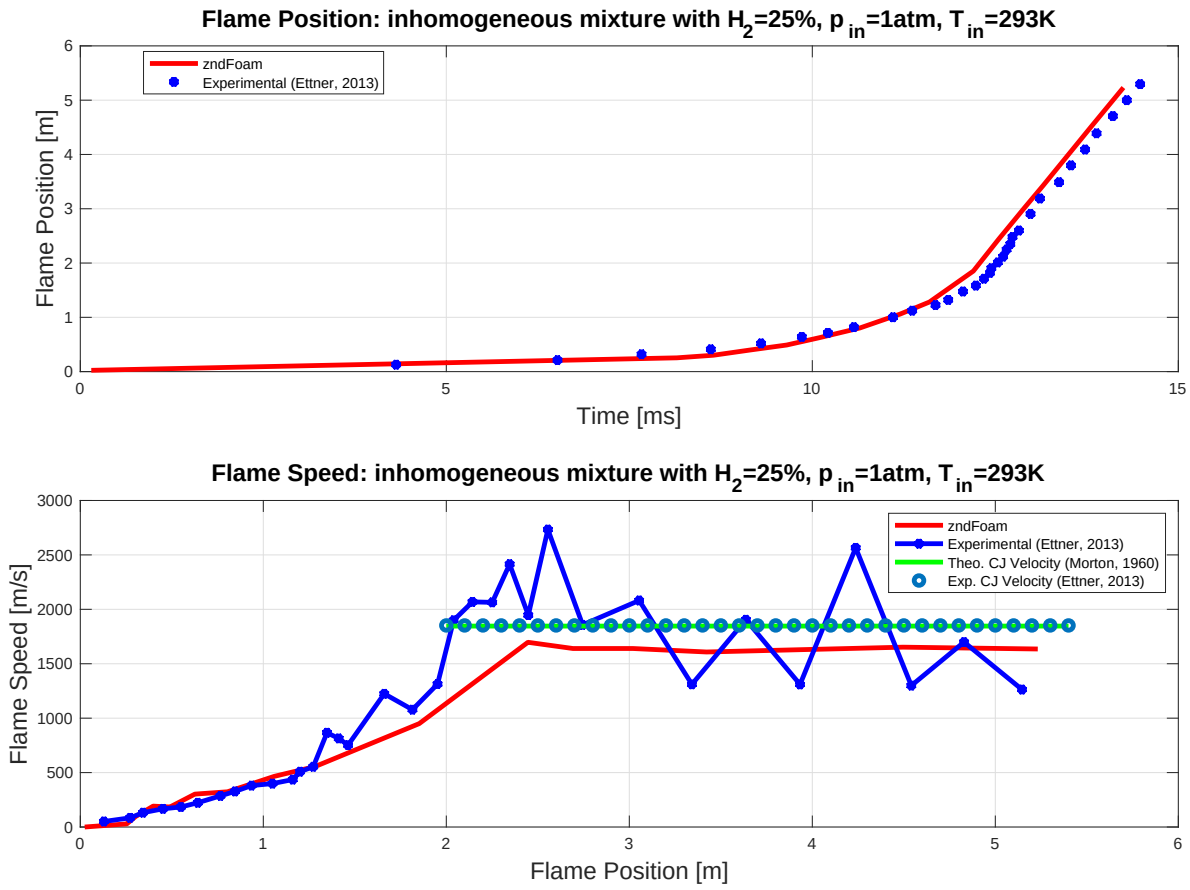

Figure 3.9: Flame position in function of time (top) and flame speed in function of tube length (bottom).

both values, due to the fact that an inhomogeneous non-stoichiometric mixture was used. In fact, the front is not perpendicular to the flow motion and the detonation velocity cannot be assumed as uniform, i.e. the previous detonation velocities values cannot be used anymore. Moreover, the numerical pressure peaks have different behaviours. In Figure F.3, emphasis on the different trends achieved on the top and bottom walls are presented. Clearly, the discrepancy of the peak pressure values and the peak pressure positions is due to the flame profile, which is not anymore perpendicular to the tube.

Again for this case an investigation on detonation cells was performed. Using the same assumption previously described, the results are shown in Figure 3.10. Clearly, in this case, detonation cells as not marked as homogeneous results: this may be ascribed to the detonation front not perpendicular to the flow. In fact, the instability is not made by compressible effect, which

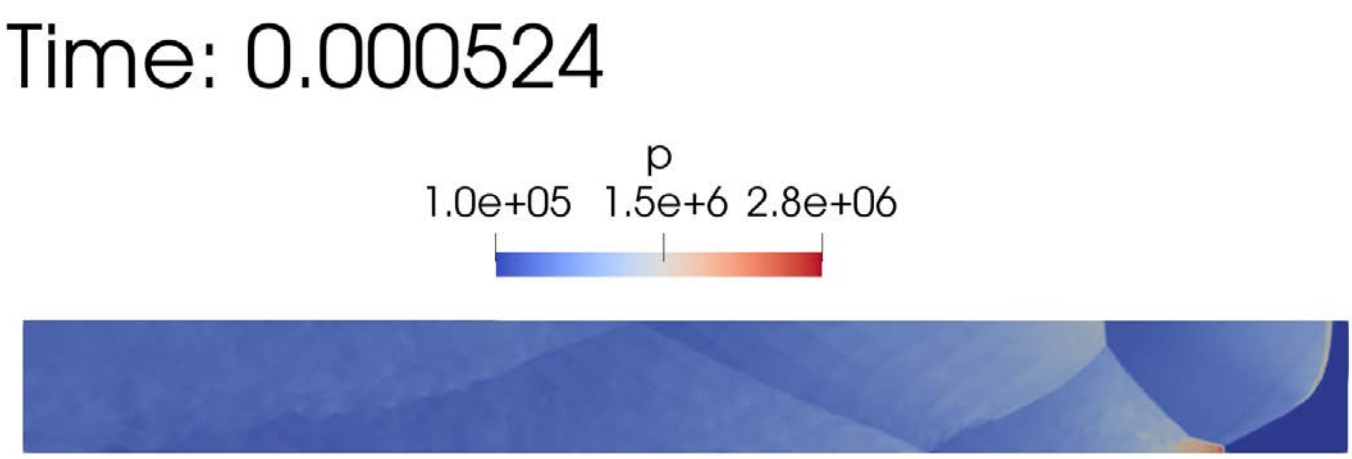

Figure 3.10: Detonation cells analysis for inhomogeneous case.

actually generates these kinds of structures, but from the mixture gradient. Thus, unlike the homogeneous case, detonation cells can not self-sustain due to the different combustion ratio at the flame front. It seems that behind the more marked compression waves, detonation cells occur similar to the previous case: these, unfortunately, cannot be taken into consideration because in the literature there are no experimental results showing effects of this type.

3.3.3 Computational time analysis

Finally, in order to estimate the computational cost among all the schemes used, computational time analysis was performed. The following analyses have been investigated:

- homogeneous mixture using ddtFoam;
- homogeneous mixture with reduced mechanism using zndFoam;
- homogeneous mixture with detailed mechanism using zndFoam.

All three simulations were analyzed on the same workstation, running 30 processors in parallel and the same mesh size. The results are shown in Figure 3.11. As expected, ddtFoam is the least expensive, followed immediately by the reduced and detailed.

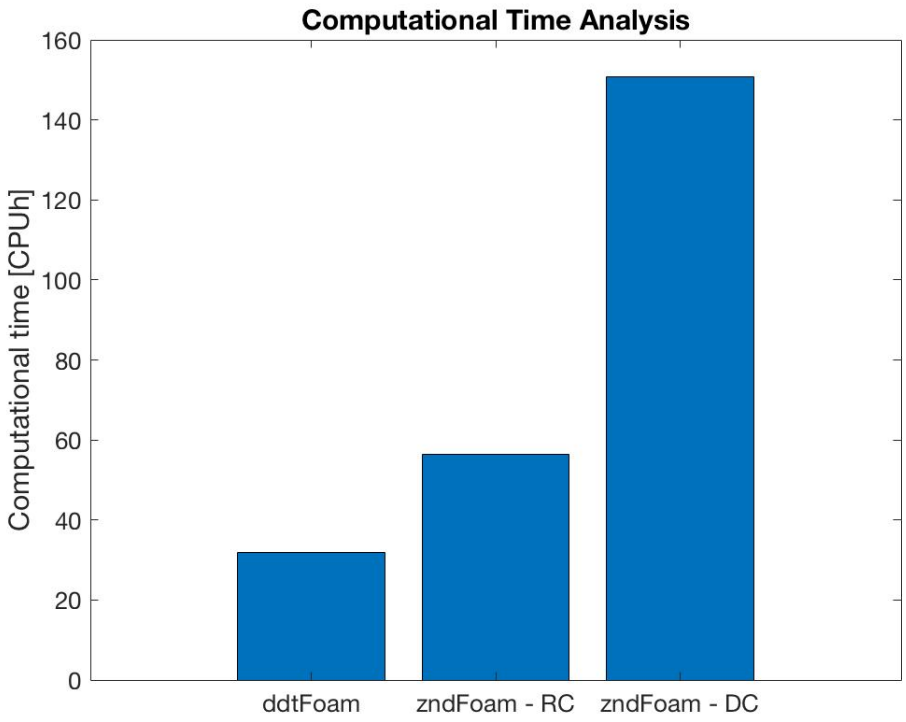

Figure 3.11: Computational time analysis.

3.4 zndFoam - C_2H_2-Oxygen

A numerical simulation for only homogeneous acetylene-oxygen mixture was performed and compared with experimental results obtained by Smirnov [65], using his test case. Due to the scarcity of experimental data, only flame speed results are taken into account. As reported in Figure 3.14, the detonation takes place in the zone of the obstacles, and then the detonation wave propagates along the tube. Deflagration period is rather short: the velocity increases by the end of the spiral region, then decreases, and then rise again as shown in Figure 3.12. The slight velocity decreasing occurs when the flame bypasses the notched section: this is due to the instantaneous reduction of turbulent mixture mixing. A fair discrepancy between theoretical and experimental detonation was found, which may be related to the low accuracy of experimental devices. The comparison was then compared to only theoretical result giving back a percentage error lower than 1%.

Again, for this kind of mixture detonation cell structure was investigated. This is clearly visible

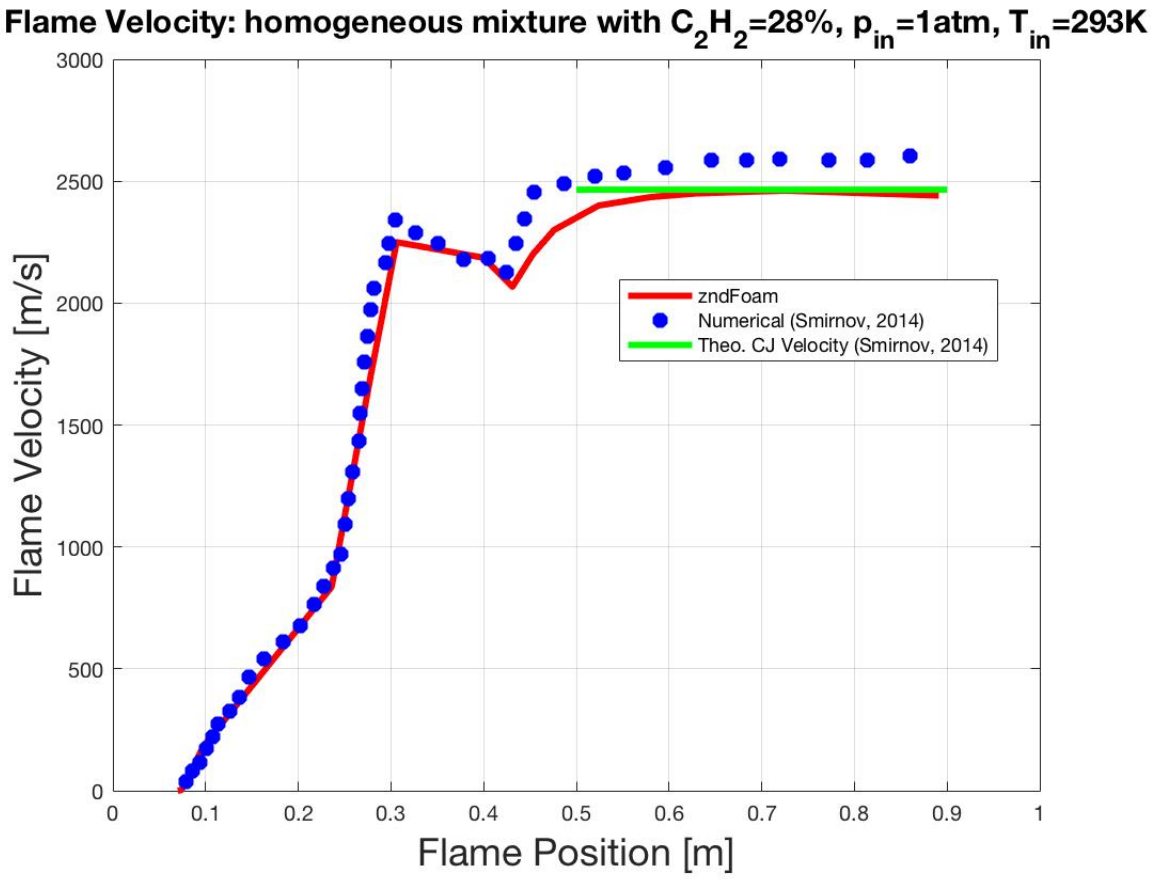

Figure 3.12: Flame velocity using acetylene-oxygen mixture.

immediately after the shock wave, showing the typical triple points path. The experiments led by [70] had shown an average width of 16.5mm. Then, the average numerical detonation cells width is in good agreement with the experimental value since the numerical value is around 18mm, leading to a percentage error of 8%.

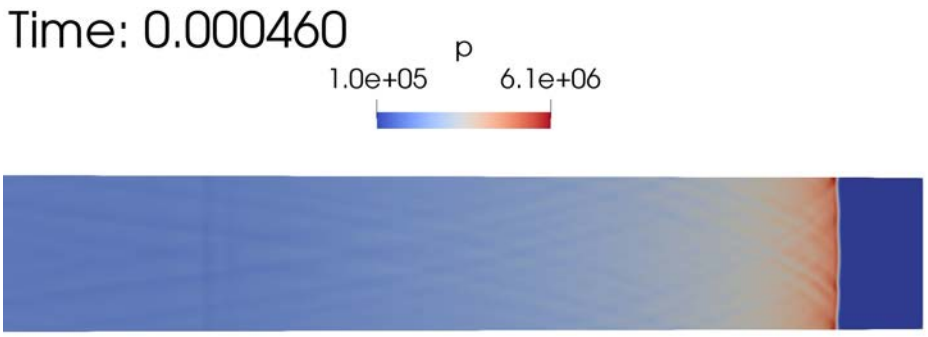

Figure 3.13: Detonation cells analysis for acetylene-oxygen mixture.

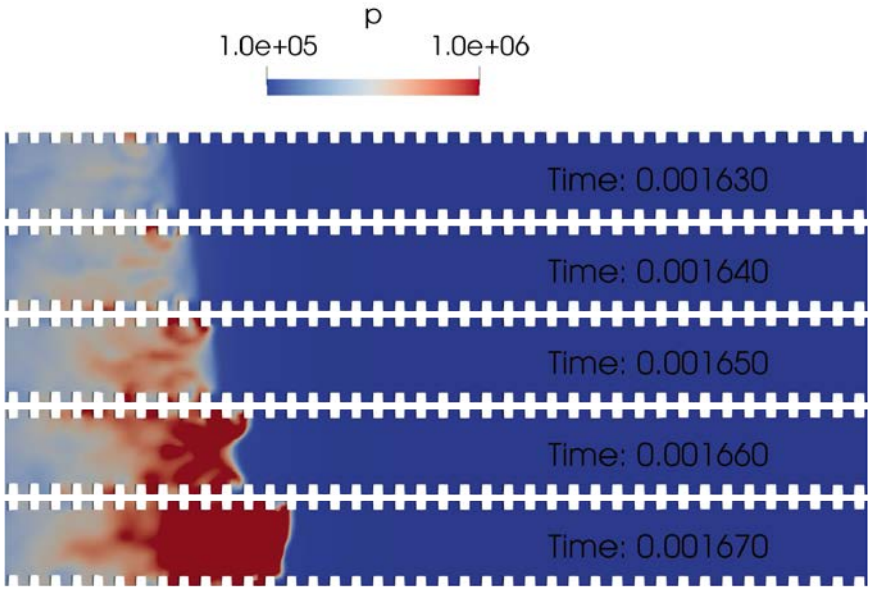

Figure 3.14: Predicted contours of pressure during DDT.

3.5 Available thrusts

A rough estimation of the thrusts of the previous test cases is provided in this section. Instead of considering the real PDE working principle, which can be split into three different parts (detonation, blow down of burnt gases and purging of the expanded burnt products), only the first phenomena has been taken into account. The thrust can be directly estimated by imposing the momentum conservation to a control volume, which covers completely the PDE [72]:

$$\sum_i F_i = \frac{d}{dt}\int_V \rho u \, dV + \int_S \rho u(\vec{u}\cdot\vec{n})\, dS \tag{3.2}$$

where only the x-direction is considered. Using the steady-state assumption and considering the second integral only at the nozzle surface, the Equation 3.2 can be approximated by:

$$F = \dot{m}_p u_e + (p_e - p_0)A_e \tag{3.3}$$

where $\dot{m}_p = rho_e u_e A_e$ is the mass flow rate, u_e, p_e and A_e are respectively the velocity, the pressure and the area at the exit. The Figure 3.15 shows the thrusts in function of time for the different mixtures involved.

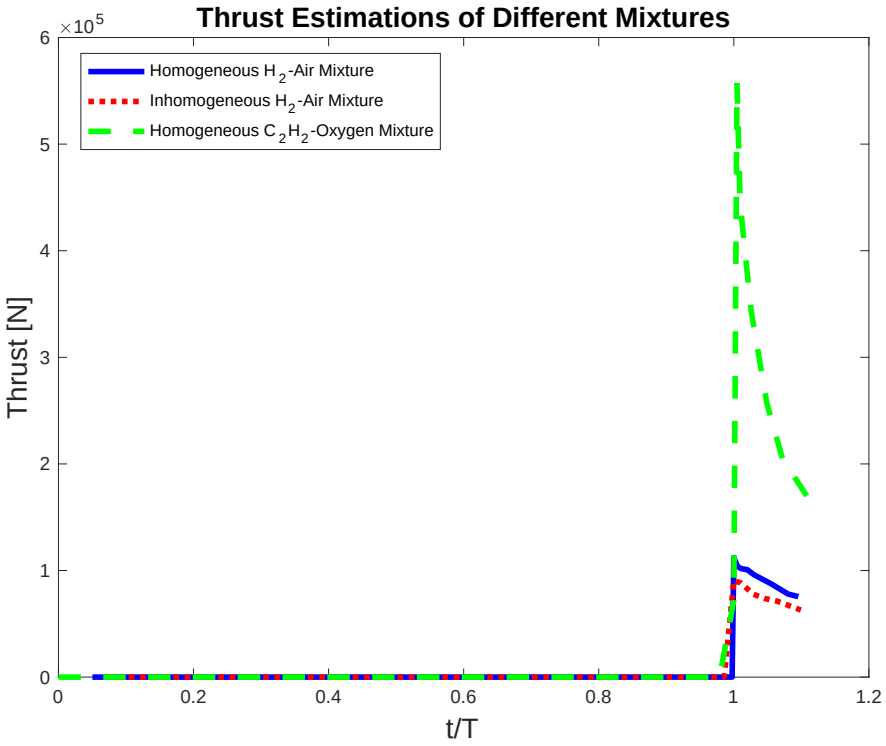

Figure 3.15: Thrust estimations for different mixtures.

Of course, the previous thrusts are overestimated because the refilling and purging processes are not considered.

Chapter 4

Conclusions

An open-source solver was developed using OpenFoam CFD platform to accurately investigate detonation effects using both reduced and detailed chemical models within detonation engines. The capability of splitting the simulations into two different solvers, using different schemes of solution, is certainly a specific feature than the existing reacting flow solvers in OpenFoam solvers. This peculiarity has shown reliable results compared to the experimental data, lower computational cost for the solution of the detailed chemistry than present solvers available from the literature and, in general, a more detailed and accurate description of the phenomenon.
The robustness of the solver against compressible flows with strong gradients was tested in a shock tube. The results show fairly good agreement with the theoretical solutions while the existing density-based reacting flow solver of OpenFoam fails to resolve the discontinuities. In order to test the capabilities of the solver, H_2-Air and C_2H_2-Oxygen have been tested in DDT tube. H2-Air mixture, both homogeneous and inhomogeneous, was burned in a 5.4 m long DDT channel with 6 cm height. The results showed good agreement with the experimental evidences and theoretical attributes of hydrogen detonation. The location of transition from deflagration to detonation was well predicted while the discrepancy between experimental and numerical results with detailed chemistry on detonation flame velocity kept below 3%. Pressure peak value at fixed location was acquired and compared with experimental result showing a percentage error below 8% in estimating both position and amplitude. The detonation cell

structures were resolved and compared by the experimental results in the literature. The solver showed a good match with the experimental cell size, with an error around 1.5%.
In the same way, C_2H_2-Oxygen mixture has been tested in a DDT tube of 1.24 m long and 2.4 cm height. The simulated DDT transition has shown a more precise description, estimating the detonation velocity with an error of 1% respect the theoretical one. Furthermore, analysis of detonation wave structure has been performed showing the numerical results: again, the average size of detonation cells is in good agreement with the experimental findings since the percentage error is kept below 8%.
In conclusion, the solver has been intensely tested in different conditions to verify that the solver provides reliable results in all relevant cases.

4.1 Recommendations for further works

An exact estimation of the thrust for the engine should be taken into account for future analyses. The entire cycle must be considered, simulating then the refilling and purging processes.
On other hand, PDEs have still some practical issue. It requires a robust and efficient detonation initiator as well as an efficient refill mechanism. Indeed, typical PDE runs in a range of 20 to 100 Hz, leading to the inability of reaching high thrust levels. Moreover, the unsteady nature of the DDT is another practical difficulty in using a PDE as a propulsion device. An alternative propulsion concept is the RDE, where the detonation is initiated once and remains while the engine is running, eliminating the need to initiate a detonation up to 100 times a second. In order to take into account all of those effects, the research should be extended also for these engines.

Bibliography

[1] M. L. Coleman. "Overview of Pulse Detonation Propulsion Technology". PhD thesis. Chemical Propulsion Information Agency, 2001.

[2] Wesley R Knick. "Characterization of Pulse Detonation Engine Performance with Varying Free Stream Stagnation Pressure Levels". PhD thesis. Air Force Institute Of Technology, 2006.

[3] Tad J Robbins. "Fuel injection strategy for a next generation Pulse Detonation Engine". PhD thesis. Naval Postgraduate School, Monterey CA, 2006.

[4] E.M. Braun R. Vutthivithayarak and F.K. Lu. "On thermodynamic cycles for detonation engines". In: *Combustion Journal* (20012).

[5] Francesco Nasutti. *Dispense del corso di Propulsione Aerospaziale*. Last accessed 19 March 2018. 2012.

[6] Wikipedia. *Turbogetto*. [Online; in data 9-luglio-2018]. 2018.

[7] Bill Gunston and P Stephens. *The development of jet and turbine aero engines*. Patrick Stephens, 1997.

[8] Nancy Hall. *Turbofan Engine*. Last accessed 19 March 2018. 2015.

[9] Fahey DW Lee DS and Foster PM. "Aviation and global climate change in the 21st century". In: *Atmos Environ* (2009).

[10] Christopher Tate. "Investigation of Pulse Detonation Engines: the Effect of Variable Blockage Ratio on the Deflagration to Detonation Transition". PhD thesis. 2015.

[11] K.K. Kuo. *Principles of combustion*. Wiley, 1986.

[12] Dora E. Musielak. *Fundamental of Pulse Detonation Engine and Related Propulsion Technology*. 2015.

[13] David G. Goodwin, Harry K. Moffat, and Raymond Speth. "Cantera: An Object-oriented Software Toolkit for Chemical Kinetics, Thermodynamics, and Transport Processes. Version 2.2.0". In: (2015).

[14] William H Heiser and David T Pratt. "Thermodynamic cycle analysis of pulse detonation engines". In: *Journal of Propulsion and Power* 18.1 (2002), pp. 68–76.

[15] T. Bussings and G. Pappas. "Pulse Detonation Engine Theory and Concepts". In: *Progess in Astronautics and Aeronautics* (1996).

[16] T Bratkovich et al. "An introduction to pulse detonation rocket engines (PDREs)". In: *33rd Joint Propulsion Conference and Exhibit*. 1997, p. 2742.

[17] William H Heiser and David T Pratt. "Thermodynamic cycle analysis of pulse detonation engines". In: *Journal of Propulsion and Power* 18.1 (2002), pp. 68–76.

[18] Ronnachai Vutthivithayarak. "Analysis of Pulse Detonation Turbojet Engines". In: (2012).

[19] James Braun. "Three dimensional analysis of a pressure gain combustor". PhD thesis. KU Leuven, 2013.

[20] SM Frolov, AV Dubrovskii, and VS Ivanov. "Three-dimensional numerical simulation of operation process in rotating detonation engine". In: *Progress in Propulsion Physics* 4 (2013), pp. 467–488.

[21] ES Oran et al. "A study of detonation structure: The formation ofunreacted gas pockets". In: *Symposium (International) on Combustion*. Vol. 19. 1. Elsevier. 1982, pp. 573–582.

[22] Yohann Eude. "Developpement d'un outil de simulation numerique des ecoulements reactifs sur maillage autoadaptatif et son application a un moteur a detonation continue". PhD thesis. Universite d'Orleans, 2011.

[23] Christian Schmitz and Miltiadis Papalexandris. "Numerical study of detonation ignition via converging shock waves". In: *APS Meeting Abstracts*. 2014.

[24] BV Voitsekhovskii, Vo V Mitrofanov, and ME Topchiyan. "Structure of the detonation front in gases (survey)". In: *Combustion, Explosion and Shock Waves* 5.3 (1969), pp. 267–273.

[25] OConaire Marcus et al. "A comprehensive modeling study of hydrogen oxidation". In: *International Journal of Chemical Kinetics* 36.11 (2004), pp. 603–622.

[26] John H. S. Lee. *The Detonation Phenomenon*. Cambridge University Press, 2008.

[27] Gareth Williams. "Combustion Theory". In: Addison-Wesley, 1985.

[28] F. Cardin and M. Favretti. *Modelli fisico matematici*. CLEUP, 2013.

[29] Pijush K Kundu, Ira M Cohen, and David R Dowling. *Fluid mechanics*. 5th ed. Academic press San Diego, 1990.

[30] George Keith Batchelor. *An introduction to fluid dynamics*. Cambridge university press, 2000.

[31] Charles F. Curtiss Joseph O. Hirschfelder and R. Byron Bird. "Molecular Theory of Gases and Liquids". In: *Science* 120.3131 (1954), pp. 1097–1097.

[32] T. Poinsot and D. Veynante. *Theoretical and Numerical Combustion*. Edwards, 2001.

[33] Stephen B. Pope. *Turbulent Flows*. Cambridge University Press, 2000.

[34] H Zhang, C Bachman, and H Fasel. "Reynolds-Averaged Navier-Stokes calculations of unsteady turbulent flow". In: *38th Aerospace Sciences Meeting and Exhibit*. 2000, p. 143.

[35] Florian Ettner. "Effiziente numerische Simulationdes Deflagrations Detonations Uebergangs". PhD thesis. TU Munchen, 2014.

[36] Wikipedia contributors. *OpenFOAM — Wikipedia, The Free Encyclopedia*. [Online; accessed 16-April-2018]. 2018.

[37] OpenFOAM contributors. *User Guide*. [Online; accessed 16-April-2018]. 2018. URL: https://openfoam.org/release/2-3-0/parallel/.

[38] L.F. Gutierrez Marcantoni, J. Tamagno, and S. Elaskar. "rhoCentralRfFoam: An OpenFOAM solver for high speed chemically active flows. Simulation of planar detonations." In: *Computer Physics Communications* 219 (2017), pp. 209–222.

[39] K. G. Vollmer, F. Ettner, and T. Sattelmayer. "Deflagration-to-Detonation Transition in Hydrogen/Air Mixtures with a Concentration Gradient". In: *Combustion Science and Technology* 184.10-11 (2012), pp. 1903–1915.

[40] Ettner Florian. *ddtFoam*. Available on line. 2013.

[41] R.I Issa. "Solution of the implicitly discretised fluid flow equations by operator-splitting". In: *Journal of Computational Physics* 62.1 (1986), pp. 40–65.

[42] Hrvoje Jasak. *Numerical Solution Algorithms for Compressible Flows*. Lecture Notes. 2007.

[43] E. Krause. "Computational Methods for Fluid Dynamics". In: *Journal of Applied Mathematics and Mechanics* 77.2 (), pp. 160–160.

[44] H.G. Weller et al. "Application of a flame-wrinkling les combustion model to a turbulent mixing layer". In: *Symposium (International) on Combustion* 27.1 (1998). Twenty-Seventh Sysposium (International) on Combustion Volume One, pp. 899–907.

[45] Konnov and Alexander. "Remaining uncertainties in the kinetic mechanism of hydrogen combustion". In: *Combustion and Flame* 152 (Mar. 2008), pp. 507–528.

[46] Joel H. FERZIGER and Milovan Peric. *Computational Methods for Fluid Dynamics*. Jan. 2002.

[47] A. Quarteroni, R. Sacco, and F. Saleri. *Matematica Numerica*. Springer, 2000.

[48] E.F. Toro. *Riemann Solvers and Numerical Methods for Fluid Dynamics: A Practical Introduction*. Springer Berlin Heidelberg, 2009.

[49] E. F. Toro, M. Spruce, and W. Speares. "Restoration of the contact surface in the HLL-Riemann solver". In: *Shock Waves* 4.1 (July 1994), pp. 25–34.

[50] Bonnie J McBride, Sanford Gordon, and Martin A Reno. "Coefficients for calculating thermodynamic and transport properties of individual species". In: (1993).

[51] A. Quarteroni. *Modellistica Numerica per Problemi Differenziali*. Springer Milan, 2005.

[52] Doyle D. Knight. "Reconstruction". In: *Elements of Numerical Methods for Compressible Flows*. Cambridge Aerospace Series. Cambridge University Press, 2006.

[53] Culbert B Laney. *Computational gasdynamics*. Cambridge university press, 1998.

[54] OpenFoam. *OpenFoam Guide*. 2018.

[55] SF Davis. "Simplified second-order Godunov-type methods". In: *SIAM Journal on Scientific and Statistical Computing* 9.3 (1988), pp. 445–473.

[56] Bernd Einfeldt. "On Godunov-type methods for gas dynamics". In: *SIAM Journal on Numerical Analysis* 25.2 (1988), pp. 294–318.

[57] Valeri I Golovitchev et al. *3-D diesel spray simulations using a new detailed chemistry turbulent combustion model*. Tech. rep. SAE Technical Paper, 2000.

[58] Jin Kusaka et al. *Numerical simulation accounting for the finite-rate elementary chemical reactions for computing diesel combustion process*. Tech. rep. SAE Technical Paper, 2005.

[59] PA Nordin. *Complex chemistry modeling of diesel spray combustion*. Chalmers University of Technology, 2001.

[60] Christopher P Stone and Fabrizio Bisetti. "Comparison of ODE Solver for Chemical Kinetics and Reactive CFD Applications". In: *52nd Aerospace Sciences Meeting*. 2014, p. 0822.

[61] Florian R Menter. "Two-equation eddy-viscosity turbulence models for engineering applications". In: *AIAA journal* 32.8 (1994), pp. 1598–1605.

[62] Florian R. Menter. "Review of the shear-stress transport turbulence model experience from an industrial perspective". In: *International Journal of Computational Fluid Dynamics* 23.4 (2009), pp. 305–316.

[63] ChangJian Wang et al. "Single-step chemistry model and transport coefficient model for hydrogen combustion". In: *Science China Technological Sciences* 55.8 (Aug. 2012), pp. 2163–2168.

[64] Min Son et al. "Effect of Spiral Turbulent Ring on Detonation Performances of Acetylene-Oxygen Mixture". In: (2013).

[65] NN Smirnov et al. "Accumulation of errors in numerical simulations of chemically reacting gas dynamics". In: *Acta Astronautica* (2015).

[66] Elaine S. Oran and Alexei M. Khokhlov. "Deflagrations, hot spots, and the transition to detonation". In: *Philosophical Transactions of the Royal Society of London A: Mathematical, Physical and Engineering Sciences* 357.1764 (1999), pp. 3539–3551.

[67] H. Brabants. "A 1d approach to chemical kinetics in detonation engines". PhD thesis. Katholieke Universiteit Leuven, 2013.

[68] J.D. Anderson. *Modern Compressible Flow: With Historical Perspective*. McGraw-Hill series in aeronautical and aerospace engineering. McGraw-Hill, 1990.

[69] Morton P Moyle, Richard B Morrison, and Stuart W Churchill. "Detonation characteristics of hydrogen-oxygen mixtures". In: *AIChE Journal* 6.1 (1960), pp. 92–96.

[70] Michael Kaneshige and Joseph E Shepherd. "Detonation database". In: (1997).

[71] CM Guirao et al. *Hydrogen-air detonations*. Tech. rep. Sandia National Labs., Albuquerque, NM (USA); McGill Univ., Montreal, Quebec (Canada), 1982.

[72] Eric Wintenberger and JE Shepherd. "Model for the performance of airbreathing pulse-detonation engines". In: *Journal of Propulsion and Power* 22.3 (2006), pp. 593–603.

[73] B Varatharajan and FA Williams. "Chemical-kinetic descriptions of high-temperature ignition and detonation of acetylene-oxygen-diluent systems". In: *Combustion and Flame* 124.4 (2001), pp. 624–645.

[74] Reaction Design. "CHEMKIN". In: (2000).

Appendix A

Detonation velocities

Below some values of detonation velocities are provided, both theoretical and experimental, for the mixtures taken into account in this work. Starting from H_2-Air mixture, the theoretical CJ velocity was calculated by using Cantera package [13] whereas the experimental value was provided by Morton [69]. Table A.1 shows both values for the hydrogen-air mixture using 25% of H_2 mole fraction.

Theoretical CJ velocity	$1871 m/s$
Experimental velocity	$1768 m/s$

Table A.1: CJ velocities for hydrogen-air mixtures

As regard the C_2H_2-Oxygen mixture, the experimental value was provided by Smirnov [65] using an unit equivalence ratio. Actually, this value is far from the theoretical one and may have been affected by experimental issues. Since this strange behaviour, only the theoretical velocity is taken into account. This is calculated by using Cantera package, as usual. Table A.2 shows both values for the acetylene-oxygen mixture using $\phi = 1$.

Theoretical CJ velocity	$2467 m/s$
Experimental velocity	$2105 m/s$

Table A.2: CJ velocities for acetylene-oxygen mixtures

Appendix B

Numerical issue using total mass equation

As said in section 2.1.4, using the total mass conservation may be dangerous from numerical point of view. In fact, summing all species equation from 1 to N - 1 and subtracting the resulting equation from the global mass conservation (Equation 2.1) yields:

$$\frac{\rho Y_N}{\partial t} + \frac{\partial(\rho u_i Y_N)}{\partial x_i} = \dot{\omega_N} + \frac{\partial}{\partial x_i}\left(\rho D_N \frac{\partial Y_N}{\partial x_i}\right) + \frac{\partial}{\partial x_i}\left(\rho \sum_{k=1}^{N-1}(D_N - D_k)\frac{\partial Y_N}{\partial x_i}\right) \tag{B.1}$$

Equation B.1 really controls Y_N. The last term of the RHS of this equation is no-physical and should not be there. The sign of the term is also unknown and depends on species profiles and diffusion coefficients: in certain cases, counter-gradient transport for Y_N may be induced.
This error is negligible when the last species Y_N is a high concentration diluent such as N_2 in air flames. For this reason, for all simulations, N_2 is considered as inert species, where inert means that is not chemically reactive.

Appendix C

Reaction mechanisms

The Arrhenius coefficients, for each mechanism used in this work, are listed below. The coefficients, based on the formal definition of the Arrhenius law, are available in literature from different authors.

C.1 Hydrogen-air mechanisms

As already said, for the simulations performed using hydrogen-air mixture have been used two different reaction schemes, in order to evaluate the overall effects of their use.

C.1.1 Reduced mechanism - OneStep

For *One-Step* mechanism, only a global reaction is taken into account where the coefficients are given by [63]:

Reaction	A	β	E
$H_2 + O_2 = H_2O$	$1.13 \cdot 10^{15}$	0	112957.41

Table C.1: Arrhenius coefficients for One-Step mechanism - units: [s, mol, cm^3, cal and K]

C.1.2 Detailed mechanism - O'Conaire

For O'Connaire scheme, the 19 elementary reactions are subdivided in four categories. The Arrhenius coefficients are given by [25]:

Sequence	*Reaction*	A	β	E
	$H2/O_2$ chain reactions			
1	$H + O_2 = O + OH$	$1.91 \cdot 10^{14}$	0.00	16.44
2	$O + H_2 = H + OH$	$5.08 \cdot 10^{4}$	2.67	6.292
3	$OH + H_2 = H + OH$	$2.16 \cdot 10^{8}$	1.51	3.43
4	$O + H_2O = H + H + M$	$2.97 \cdot 10^{6}$	2.02	13.4
	H_2/O_2 dissociation/recombination reactions			
5	$H_2 + M = H + H + M$	$4.57 \cdot 10^{19}$	-1.40	105.1
6	$O + O + M = O_2 + M$	$6.17 \cdot 10^{15}$	-0.50	0.00
7	$O + H + M = OH + M$	$4.72 \cdot 10^{18}$	-1.0	0.00
8	$H + OH + M = H_2O + M$	$4.50 \cdot 10^{22}$	-2.0	0.00
	Formation and consumption of HO_2			
9	$H + O_2 + M = HO_2 + M$	$3.48 \cdot 10^{16}$	-0.41	-1.12
	$H + O_2 = HO_2$	$1.48 \cdot 10^{12}$	0.60	0.00
10	$HO_2 + H = H_2 + O_2$	$1.66 \cdot 10^{13}$	0.00	0.82
11	$HO_2 + H = OH + OH$	$7.08 \cdot 10^{13}$	0.00	0.30
12	$HO_2 + O = OH + O_2$	$3.25 \cdot 10^{13}$	0.00	0.00
13	$HO_2 + OH = H_2O + O_2$	$2.89 \cdot 10^{13}$	0.00	-0.50
	Formation and consumption of H_2O_2			
14	$HO_2 + HO_2 = H_2O_2 + O_2$	$4.2 \cdot 10^{14}$	0.00	11.98
	$HO_2 + HO_2 = H_2O_2 + O_2$	$1.3 \cdot 10^{11}$	0.00	-1.629
15	$H_2O_2 + M = OH + OH + M$	$1.27 \cdot 10^{17}$	0.00	45.5
	$H_2O_2 = OH + OH$	$2.95 \cdot 10^{14}$	0.00	48.4
16	$H_2O_2 + H = H_2O + OH$	$2.41 \cdot 10^{13}$	0.00	3.97
17	$H_2O_2 + H = H_2 + HO_2$	$6.03 \cdot 10^{13}$	0.00	7.95
18	$H_2O_2 + O = OH + HO_2$	$9.55 \cdot 10^{6}$	2.00	3.97
19	$H_2O_2 + OH = H_2O + HO_2$	$1.0 \cdot 10^{12}$	0.00	0.00
	$H_2O_2 + OH = H_2O + HO_2$	$5.8 \cdot 10^{14}$	0.00	9.56

Table C.2: Arrhenius coefficients for O'Conaire's scheme - units: [s, mol, cm^3, Kcal and K]

C.2 Acetylene-oxygen mechanism

For the simulation performed by using acetylene-oxygen have only been used the detailed scheme, composed by 25 reactions. The Arrhenius coefficients are given by [73]:

Sequence	*Reaction*	A	β	E
	$H2/O_2$ chain reactions			
1	$H + O_2 = O + OH$	$3.52 \cdot 10^{16}$	-0.70	71.40
2	$OH + O = H + O_2$	$1.15 \cdot 10^{14}$	-0.32	-0.70
3	$OH + H_2 = H_2O + H$	$1.17 \cdot 10^{9}$	1.30	15.20
4	$O + H_2O = 2OH$	$7.60 \cdot 10^{0}$	3.84	53.50
5	$2OH = O + H_2O$	$2.45 \cdot 10^{-1}$	3.97	-19.00
	Hydrogenperoxyl Formation and Consumption			
6	$H + O_2 + M = HO_2 + M$	$6.76 \cdot 10^{19}$	-1.40	0.00
7	$HO_2 + H = 2OH$	$1.70 \cdot 10^{14}$	0.00	3.70
8	$HO_2 + H = H_2 + O_2$	$4.28 \cdot 10^{13}$	0.00	5.90
9	$HO_2 + OH = H_2O + O_2$	$2.89 \cdot 10^{13}$	0.00	-2.10
	Direct Recombination			
10	$H + OH + M = H_2O + M$	$2.20 \cdot 10^{22}$	-2.00	0.00
11	$H_2O + M = H + OH + M$	$2.18 \cdot 10^{23}$	-1.93	499.00
	Carbon Monoxide Reactions			
12	$CO + OH = CO_2 + H$	$4.40 \cdot 10^{6}$	1.50	-3.10
13	$CO_2 + H = CO + OH$	$4.97 \cdot 10^{8}$	1.50	89.70
	Initiation and Fuel Consumption			
14	$C_2H_2 + O_2 = CH_2O + CO$	$4.60 \cdot 10^{15}$	-0.54	188.00
15	$C_2H_2 + O = HCCO + H$	$4.00 \cdot 10^{14}$	0.00	44.60
16	$C_2H_2 + OH = CH_2CO + H$	$1.90 \cdot 10^{7}$	1.70	4.20
	Ketene and Ketyl Consumption			
17	$CH_2CO + O = HCCO + OH$	$1.00 \cdot 10^{13}$	0.00	8.40
18	$CH_2CO + H = CH_3 + CO$	$1.11 \cdot 10^{7}$	2.00	8.40
19	$HCCO + O_2 = 2CO + OH$	$2.88 \cdot 10^{7}$	1.70	4.20
	Formaldehyde, Formyl and Methyl Consumption			
20	$CH_2O + M = CHO + H + M$	$6.26 \cdot 10^{16}$	0.00	326.00
21	$CH_2O + H = CHO + H_2$	$1.26 \cdot 10^{8}$	1.62	9.10
22	$CH_2O + OH = CHO + H_2O$	$3.90 \cdot 10^{10}$	0.89	1.70
23	$CHO + M = CO + H + M$	$1.86 \cdot 10^{17}$	-1.00	71.10
24	$CHO + H = CO + H_2$	$1.00 \cdot 10^{14}$	0.00	0.00
25	$CH_3 + O = CH_2O + H$	$8.43 \cdot 10^{13}$	0.00	0.00

Table C.3: Arrhenius coefficients for Varatharajan scheme - units: [s, mol, cm^3, KJ and K]

C.3 Thermophysical table

An example of thermophysical table, that must be provided for each simulation, is shown below. For each species, the coefficients for the polynomials used to calculate the thermodynamics variable are included, as well as the operability range [50]. In fact, at high temperature the coefficients are no longer valid because catalysis effects also should be taken into consideration. A tutorial that explains how to use this table can be found in [74].

```
THERMO ALL
     200.00  1000.000  8000.00
O2                121386O   2               G 0200.00   8000.00   1000.00      1
 0.03697578E+02 0.06135197E-02-0.01258842E-05 0.01775281E-09-0.01136435E-13    2
-0.01233930E+05 0.03189166E+02 0.03212936E+02 0.01127486E-01-0.05756150E-05    3
 0.01313877E-07-0.08768554E-11-0.01005249E+05 0.06034738E+02                   4
O                 120186O   1               G 0200.00   8000.00   1000.00      1
 0.02542060E+02-0.02755062E-03-0.03102803E-07 0.04551067E-10-0.04368052E-14    2
 0.02923080E+06 0.04920308E+02 0.02946429E+02-0.01638166E-01 0.02421032E-04    3
-0.01602843E-07 0.03890696E-11 0.02914764E+06 0.02963995E+02                   4
OH                1212860   1H   1          G 0200.00   8000.00   1000.00      1
 0.02882730E+02 0.01013974E-01-0.02276877E-05 0.02174684E-09-0.05126305E-14    2
 0.03886888E+05 0.05595712E+02 0.03637266E+02 0.01850910E-02-0.01676165E-04    3
 0.02387203E-07-0.08431442E-11 0.03606782E+05 0.01358860E+02                   4
H2O2              120186H   2O   2          G 0200.00   8000.00   1000.00      1
 0.04573167E+02 0.04336136E-01-0.01474689E-04 0.02348904E-08-0.01431654E-12    2
-0.01800696E+06 0.05011370E+01 0.03388754E+02 0.06569226E-01-0.01485013E-05    3
-0.04625806E-07 0.02471515E-10-0.01766315E+06 0.06785363E+02                   4
HO2                20387H   1O   2          G 0200.00   8000.00   1000.00      1
 0.04072191E+02 0.02131296E-01-0.05308145E-05 0.06112269E-09-0.02841165E-13    2
-0.01579727E+04 0.03476029E+02 0.02979963E+02 0.04996697E-01-0.03790997E-04    3
 0.02354192E-07-0.08089024E-11 0.01762274E+04 0.09222724E+02                   4
H2O                20387H   2O   1          G 0200.00   8000.00   1000.00      1
 0.02672146E+02 0.03056293E-01-0.08730260E-05 0.01200996E-08-0.06391618E-13    2
-0.02989921E+06 0.06862817E+02 0.03386842E+02 0.03474982E-01-0.06354696E-04    3
 0.06968581E-07-0.02506588E-10-0.03020811E+06 0.02590233E+02                   4
H2                121286H   2               G 0200.00   8000.00   1000.00      1
 0.02991423E+02 0.07000644E-02-0.05633829E-06-0.09231578E-10 0.01582752E-13    2
-0.08350340E+04-0.01355110E+02 0.03298124E+02 0.08249442E-02-0.08143015E-05    3
-0.09475434E-09 0.04134872E-11-0.01012521E+05-0.03294094E+02                   4
H                 120186H   1               G 0200.00   8000.00   1000.00      1
 0.02500000E+02 0.00000000E+00 0.00000000E+00 0.00000000E+00 0.00000000E+00    2
 0.02547163E+06-0.04601176E+01 0.02500000E+02 0.00000000E+00 0.00000000E+00    3
 0.00000000E+00 0.00000000E+00 0.02547163E+06-0.04601176E+01                   4
END
```

Appendix D

Polynomials for the gradient hydrogen concentration

Hydrogen simulations were performed with and without gradient in H_2-Air mixtures. The hydrogen mole fraction for average hydrogen contents at 10%, 20%, 30%, 40% was obtained from 3D injection calculations [35]. The resulting 1D fraction, after 3s, can be expressed as polynomials of fifth degree:

$$x_{H2} = a_5 y^5 + a_4 y^4 + a_3 y^3 + a_2 y^2 + a_1 y + a_0 \tag{D.1}$$

The coefficients are given on Table D.1, where the y-value must be within the range $y \in [-0.06, 0]$.

	10%	20%	30%	40%
a_5	$-3.5096 \cdot 10^4$	$1.8472 \cdot 10^5$	$3.7046 \cdot 10^5$	$5.6996 \cdot 10^5$
a_4	$-3.2606 \cdot 10^4$	$-1.4072 \cdot 10^4$	$1.8926 \cdot 10^4$	$6.664 \cdot 10^4$
a_3	$-5.2576 \cdot 10^3$	$-6.7836 \cdot 10^3$	$-5.7421 \cdot 10^3$	$-2.6212 \cdot 10^3$
a_2	$-2.6215 \cdot 10^2$	$-4.1797 \cdot 10^2$	$-4.6044 \cdot 10^2$	$-4.1188 \cdot 10^2$
a_1	$-3.8466 \cdot 10^{-1}$	$-6.0981 \cdot 10^{-1}$	$-4.9862 \cdot 10^{-1}$	$-1.7976 \cdot 10^{-1}$
a_0	$1.9909 \cdot 10^{-1}$	$3.7736 \cdot 10^{-1}$	$5.2644 \cdot 10^{-1}$	$6.4839 \cdot 10^{-1}$

Table D.1: Coefficients for determining hydrogen fraction in calculations with concentration gradient.

Appendix E

Close Up on the Chemical Model

Considering a system a R reactions with S species, the kinetic system of the ordinary differential equations is given by:

$$\frac{dY_j}{dt} = \sum_i^R \nu_{ij}\omega_j \quad j = 1, 2, \ldots, S. \tag{E.1}$$

where ν_{ij} are the stoichiometric values. For instance, a more detailed hydrogen combustion mechanism is defined by:

$$\begin{aligned} R1 \quad H_2 + O_2 &\rightarrow H + HO_2 \qquad \omega_1 \\ R2 \quad O_2 + H &\rightarrow OH + O \qquad \omega_2 \\ R3 \quad H_2 + OH &\rightarrow H + H_2O \qquad \omega_3 \\ R4 \quad H_2 + O &\rightarrow H + OH \qquad \omega_4 \end{aligned} \tag{E.2}$$

The calculation of the production rates is based on Equation E.1. For example, the hydrogen atom H is produced in reaction step 1, 3 and 4 (ν=+1) and it is consumed in reaction step 2 (ν=-1). The line of the kinetic system of ODEs, corresponding to the production of H is the following:

$$\frac{d[H]}{dt} = +1\omega_1 - 1\omega_2 + 1\omega_3 + +1\omega_4 \tag{E.3}$$

In the similar way, the production of water can be described by the following equations:

$$\frac{d[H_2O]}{dt} = +1\omega_3 \tag{E.4}$$

Taking into account all the species involved in the mixture, the system becomes, in matrix form:

$$\frac{d\boldsymbol{Y}}{dt} = \boldsymbol{\nu\omega} \tag{E.5}$$

which is clearly a system of ordinary differential equations.

Appendix F

Complementary results for the simulations performed

F.0.1 ddtFoam

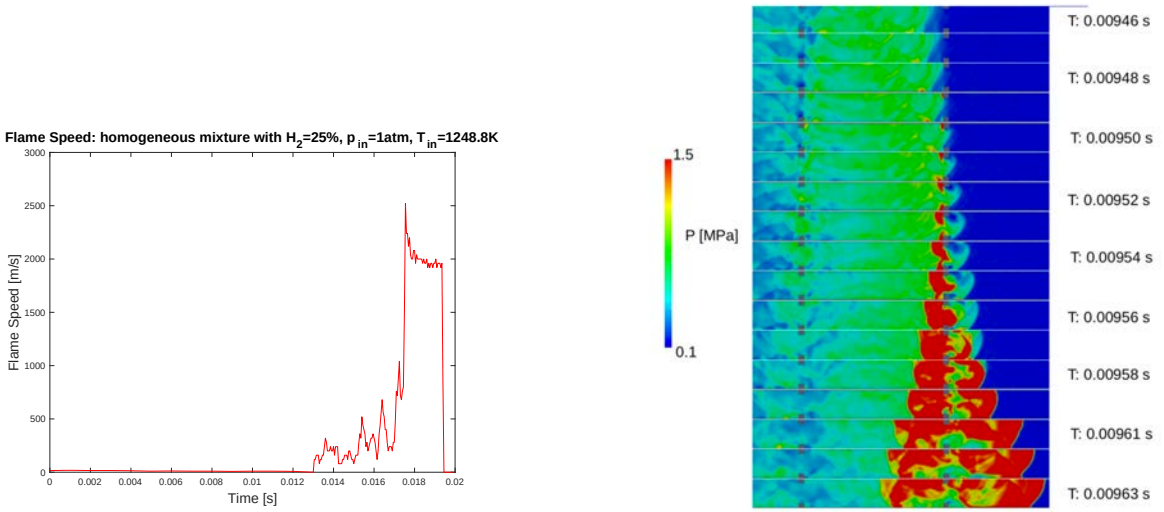

Figure F.1: Flame speed in function of time (left) and predicted contours of pressure during DDT [19] (right).

F.0.2 zndFoam (H_2-Air Homogeneous Mixture)

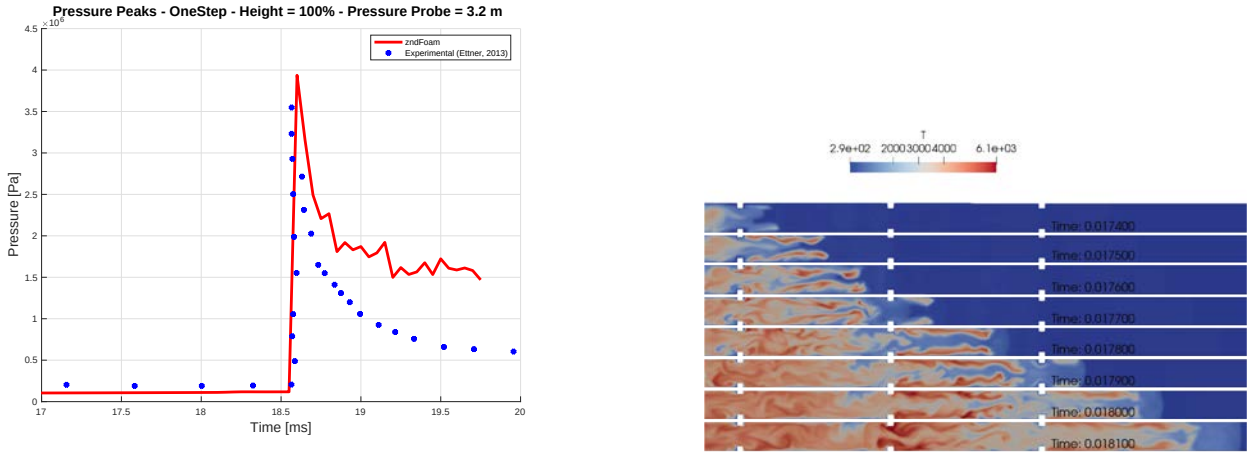

Figure F.2: Pressure peak in function of time (left) and predicted contours of temperature during DDT (right) using OneStep mechanism.

F.0.3 zndFoam (H_2-Air Inhomogeneous Mixture)

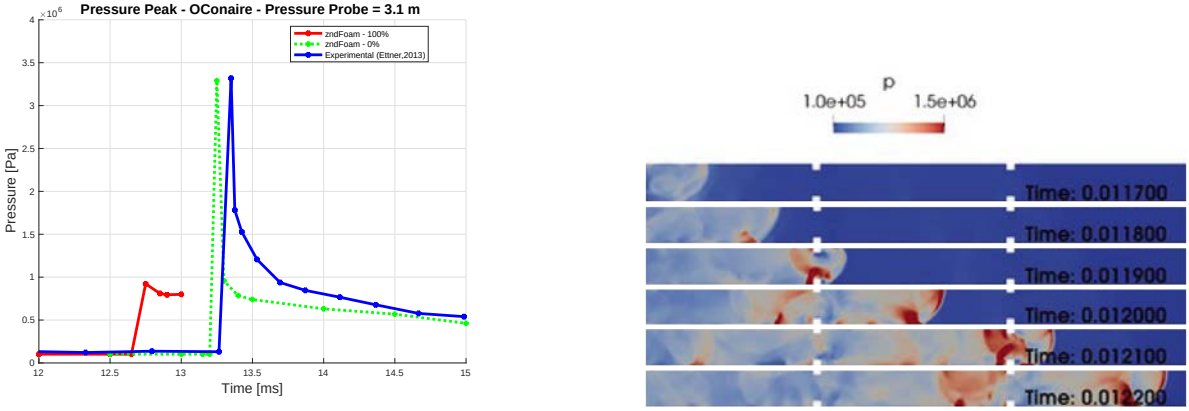

Figure F.3: Pressure peak in function of time (left) and predicted contours of pressure during DDT (right) using OneStep mechanism.